

BIPOLAR SUPERNOVA EXPLOSIONS: NUCLEOSYNTHESIS & IMPLICATION ON ABUNDANCES IN EXTREMELY METAL-POOR STARS

KEIICHI MAEDA¹, & KEN'ICHI NOMOTO^{1,2}

To appear in the Astrophysical Journal

ABSTRACT

Hydrodynamics and explosive nucleosynthesis in bipolar supernova explosions are examined to account for some peculiar properties of hypernovae as well as peculiar abundance patterns of metal-poor stars. The explosion is assumed to be driven by bipolar jets which are powered by accretion onto a central remnant. The energy injection rate by the jets is assumed to be proportional to the accretion rate, i.e., $\dot{E}_{\text{jet}} = \alpha \dot{M} c^2$. We explore the features of the explosions with varying progenitors' masses and jet properties. The outcomes are different from conventional spherical models. (1) In the bipolar models, Fe-rich materials are ejected at high velocities along the jet axis, while O-rich materials occupy the central region whose density becomes very high as a consequence of continuous accretion from the side. This configuration can explain some peculiar features in the light curves and the nebular spectra of hypernovae. (2) Production of ^{56}Ni tends to be smaller than in spherical thermal bomb models. To account for a large amount of ^{56}Ni observed in hypernovae, the jets should be initiated when the compact remnant mass is still smaller than $2 - 3M_{\odot}$, or the jets should be very massive and slow. (3) Ejected isotopes are distributed as follows in order of decreasing velocities: ^{64}Zn , ^{59}Co , ^{56}Fe , ^{44}Ti , and ^4He at the highest velocities, ^{55}Mn , ^{52}Cr , ^{32}S , and ^{28}Si at the intermediate velocities, and ^{24}Mg , ^{16}O at the lowest velocities. (4) The abundance ratios (Zn, Co)/Fe are enhanced while the ratios (Mn, Cr)/Fe are suppressed. This can account for the abundance pattern of extremely metal-poor stars. These agreements between the models and observations suggest that hypernovae are driven by bipolar jets and have significantly contributed to the early Galactic chemical evolution.

Subject headings: hydrodynamics – nuclear reactions, nucleosynthesis, abundances – stars: abundances – stars: Population II – supernovae: general – Galaxy: abundances

1. INTRODUCTION

The basic explosion mechanisms of core-collapse (Type II, Ib, Ic) supernovae (SNe II, Ib, Ic) have not been clarified (e.g., Janka et al. 2003), and the essential importance of asphericity has been suggested from observations, including a direct HST image of SN1987A (Wang et al. 2002), and large optical linear polarization in SNe Ib/Ic (Wang et al. 2001).

The discovery of a new class of supernovae, 'hypernovae', which have been suggested to have distinctly large kinetic energies (hereafter E) as compared with previously known supernovae (Galama et al. 1998; Iwamoto et al. 1998), brought us a new light on this issue. As will be discussed below, some peculiar properties of hypernovae have indicated a large deviation from spherical symmetry. Here we present bipolar explosion models for hypernovae to account for those properties. We further apply our nucleosynthesis results to account for some peculiar abundance patterns of metal-poor stars, which have not been predicted by spherical explosion models.

1.1. Properties of Hypernovae

In 1998, the unusually bright SN Ic 1998bw with very broad spectral features was discovered in the small error box of the γ -ray burst GRB980425 (Galama et al. 1998). The large expansion velocity combined with relatively slow evolution in the optical spectra and the light curve (when

compared with those of SN 1994I for example) led to the conclusion that the supernova was fairly energetic with $E_{51} \sim 30$ (where $E_{51} = E/10^{51}\text{ergs}$) and had very massive C+O ejecta $M_{\text{ej}} \sim 10M_{\odot}$ (Iwamoto et al. 1998; Woosley, Eastman, & Schmidt, 1999). It was most likely an end product of a star with the zero-age main-sequence mass $M_{\text{ZAMS}} \sim 40M_{\odot}$. Iwamoto et al. (1998) used the term 'hypernova' to describe such a hyper-energetic supernova with $E_{51} \gtrsim 10$. We follow this terminology hereafter in this paper.

Beginning with SN1998bw, there is a growing list of hypernovae. It now includes SNe Ic 1997ef (Iwamoto et al. 2000; Mazzali, Iwamoto, & Nomoto 2000), 1999as (Knop et al. 1999; Hatano et al. 2001), 2002ap (Mazzali et al. 2002; Kinugasa et al. 2002), Type IIn supernovae (SNe IIn) 1997cy (Germany et al. 2000; Turatto et al. 2000) and 1999E (Rigon et al. 2003). Still more SNe have been proposed as hypernova candidates (e.g., Nomoto et al. 2001). For reviews of hypernovae, see Nomoto et al. (2001, 2003).

With the growing number of samples, interesting features have been uncovered (e.g., Nomoto et al. 2003). Figure 1 summarizes E and $M(^{56}\text{Ni})$ (the ejected mass of ^{56}Ni) against M_{ZAMS} for several core-collapse supernovae/hypernovae derived by the previous studies.

- (1) For progenitors with $M_{\text{ZAMS}} \lesssim 20M_{\odot}$, E and $M(^{56}\text{Ni})$ are fairly homogeneous with the representative values of $E_{51} \sim 1$ and $M(^{56}\text{Ni}) \sim 0.07M_{\odot}$.

¹Department of Astronomy, School of Science, University of Tokyo, Hongo 7-3-1, Bunkyo-ku, Tokyo 113-0033, Japan: maeda@astron.s.u-tokyo.ac.jp

²Research Center for the Early Universe, School of Science, University of Tokyo, Hongo 7-3-1, Bunkyo-ku, Tokyo 113-0033, Japan

- (2) There seems to be a transition in those properties around $M_{\text{ZAMS}} = 20 - 25M_{\odot}$. In the regime where $M_{\text{ZAMS}} > 20 - 25M_{\odot}$, there exist bright energetic hypernovae at one extreme and faint low-energy Type II supernovae SN II 1997D (Turatto et al. 1998) and SN II 1999br (Hamuy 2003; Zampieri et al. 2003) on the other. There may be a variety of SNe which express intermediate cases between those two branches (Hamuy 2003).
- (3) In the 'hypernova branch', E and $M(^{56}\text{Ni})$ are larger for larger M_{ZAMS} .

The apparent transition leads to the hypothesis that the explosion mechanism of stars with zero-age main-sequence masses $M_{\text{ZAMS}} > 20 - 25M_{\odot}$ might be different from that of less massive stars ($M_{\text{ZAMS}} \lesssim 20M_{\odot}$), especially for hypernovae given their large energies. (For faint SNe, the small E may simply be attributed to a large gravitational binding energy. Unless the explosion mechanism provides a much larger energy than a typical SNe, a more massive star will experience more significant fallback. See Woosley & Weaver (1995).)

1.2. Indications of Asphericity in Hypernovae

Subsequent studies have indeed uncovered the discrepancies between observations of hypernovae and a conventional spherical model (a spherical thermal bomb model: Aufderheide, Baron, & Thielemann, 1991). The model had well described observations of normal core collapse supernovae, e.g., SN1994I (e.g., Iwamoto et al. 1994). The discrepancies raised by these studies are summarized as follows:

- (1) Late time spectra of SN1998bw showed that the FeII] blended lines were broader than the OI] 6300 lines, indicating Fe was ejected with larger velocities than O along the line of sight (Mazzali et al. 2001). Maeda et al. (2002) suggested that the explosion was highly aspherical and bipolar by demonstrating that such an explosion naturally explains this property.
- (2) Modeling the light curves of SNe 1998bw (Nakamura et al. 2001a), 1997ef (Iwamoto et al. 2000; Mazzali et al. 2000), and 2002ap (Yoshii et al. 2003) showed the deviation of the observed curves from the synthetic curves based on the spherical explosion models after ~ 50 days. All the model curves are much fainter than the observed curves at these epochs. Maeda et al. (2003) have shown that this failure is resulted from too low densities at low velocities in the spherical hydrodynamic models. By introducing a dense inner component, which is not expected in spherical hydrodynamic models, they have reproduced the light curves of SNe 1998bw, 1997ef, and 2002ap at the whole epochs observed.
- (3) The spectroscopic modeling of SN1997ef also suggested the existence of a dense core. It also requires that the density distribution at an outer envelope is flatter than obtained by spherical thermal bomb models (Mazzali et al. 2000).

- (4) On spectropolarimetries, SNe 1998bw and 2002ap had linear polarization of $\sim 1\%$ (Iwamoto et al. 1998) and $\sim 2\%$ (Kawabata et al. 2002; Leonard et al. 2002; Wang et al. 2003), respectively. Because local polarization should be totally cancelled out in strictly spherically symmetrical geometry, existence of net polarization is interpreted as evidence of asphericity in ejecta. Kawabata et al. (2002) suggested that the combination of the mildly distorted ejecta and the jet material at $v \gtrsim 0.115c$ could explain their spectropolarimetric data of SN 2002ap.

These features of hypernovae, combined with their large E , have suggested that hypernovae are bipolar explosions.

1.3. Bipolar Explosion Models

A bipolar explosion could arise in a core-collapse supernova through several mechanisms, if rotation in a pre-explosion core is sufficiently large. In the neutrino driven delayed explosion scenario, the rotation would make a newly born neutron star a pancake configuration. This prefers strong neutrino heating along the rotational axis (Yamada & Sato, 1994). In the extreme case, the core would become a black hole surrounded by a hyper accreting torus. It has been suggested that such a system can generate an outflow with the energy comparable to those in hypernovae through neutrino annihilation and/or viscous dissipation (Woosley 1993; MacFadyen & Woosley 1999). Another possible mechanism is a MHD driven explosion, where the magnetic field amplified by rotation up to $\sim 10^{15} - 10^{16}\text{G}$ would make a strong outflow along the axis of magnetic field lines. The central object can be either a neutron star (LeBlanc & Wilson 1970; Wheeler et al. 2000) or a black hole (Brown et al. 2000). The latter provides further two options for the energy source: the binding energy of the accretion disk and the rotational energy of the black hole through Blandford & Znajek mechanism (Blandford & Znajek 1977).

Such an explosion should show different characteristics in hydrodynamics and nucleosynthesis. The nature of the central energy-generating system is quite complicated and involves physics which is not well understood yet. The outcome, however, is relatively simple. It is the interaction between the jets and the stellar envelope. Therefore, once the property of the jets is specified, subsequent hydrodynamical evolution and nucleosynthesis can be examined in detail. In fact, the inverse approach is possible. First assume the jet property, then examine the outcome of the explosion. The results can be compared with observation. The comparison finally puts constraints on the properties of the jets, and thus the energy generation mechanism.

This strategy has been taken by several authors in studying the outcome and observational consequences of jet-driven supernova explosions. Khokhlov et al. (1999) examined hydrodynamical interaction between the jets and the surrounding stellar mantle for one representative case with $M_{\text{ZAMS}} = 15M_{\odot}$ and a fixed jet property. MacFadyen, Woosley, & Heger (2001) investigated the effects of jets from a central compact remnant in the context of a failed supernova explosion of a $25M_{\odot}$ progenitor star. They studied the interaction by varying the jet parameters. However, neither of the above hydrodynamical studies computed nucleosynthesis.

On the other hand, Nagataki (2000) and Maeda et al. (2002) examined nucleosynthesis in aspherical supernova/hypernova explosions, using aspherical energy inputs at the center of stars with $M_{\text{ZAMS}} = 20$ and $40M_{\odot}$, respectively. In their studies, however, the energy injection by the jets was simplified as compared to that of Khokhlov et al. (1999) and MacFadyen et al. (2001), as their models represented aspherical prompt explosions which apply only to the case where the time scale of the energy generation is much shorter than the hydrodynamical time scale.

There are two possible sites for nucleosynthesis associated with jet-driven supernova explosions: the stellar materials heated by the jets and the materials in the jets themselves. As stellar materials falls onto a central remnant, they cool via photodisintegration and neutrino emissions to form an accretion disk. A fraction of the accreted materials is likely ejected from the accretion disk, rather than is accreted onto the central remnant (Narayan, Piran, and Kumar 2001). This accretion disk wind likely escapes from the central region along the rotational axis and shows collimation, i.e., a jetted wind.

How much fraction of the accreting gas is ejected depends on the accretion rate and the typical radius where the accretion disk forms (Narayan et al. 2001). They are physically related to the angular momentum distribution and the viscosity in the progenitor star (MacFadyen 2003). Unfortunately, both are rather uncertain. In the present study, we assume that only a small fraction of the accreting gas is ejected as the jets from the central region (10 or 50%: denoted as μ in section 2), so that nucleosynthesis in the heated stellar materials is more prominent than in the jet (wind) materials themselves.

The purpose of this paper is first to investigate in more detail the outcome (hydrodynamics and nucleosynthesis) of supernova explosions driven by bipolar jets for such massive stars as $M_{\text{ZAMS}} \gtrsim 25M_{\odot}$. We model the jet properties in terms of the accretion rate, which itself is affected by the jet properties through the hydrodynamical interaction. This approach makes it possible to calculate the self-regulated interaction, and investigate how the jet properties affect the outcome by modeling the interaction with varying parameters. With the detailed nucleosynthesis yields, we discuss their possible influence on the early Galactic chemical evolution.

We note the two main assumptions in the present study: the parameterized constant jet properties and the small mass of the jet materials. In reality, the jets could be highly variable. The variability will affect the detailed structure in the jet materials (e.g., Aloy et al. 2000), though we believe that the constant jet properties express the typical behavior and are adequate for the purpose of this paper. The assumption that only a small fraction of the accreting gas is ejected as the jets (i.e., the small mass of the jets) puts more important limitation. Changing the mass of the jets will change the evolution of the mass of the central remnant, may change the hydrodynamic interaction between the jets and the stellar materials. Moreover, in the case of very massive jets, if they are realized, nucleosynthesis products in the jets will become prominent than those in the heated stellar materials (Pruet, Woosley, & Hoffman 2003; MacFadyen 2003). This is an interesting possibility, while we postpone to study such a very massive

jets to future works.

In Section 2, we describe our models of bipolar supernova explosions in detail. Results are shown in Section 3, which is divided into three subsections. Section 3.1 gives the results of hydrodynamics, discussing how the outcome (e.g., the degree of asphericity and the final mass of the central compact remnant) depends on the jet properties. Section 3.2 focuses on the production of ^{56}Ni . Section 3.3 shows the results of detailed nucleosynthesis, where we put emphasis on the difference between our models and previous yields. In Section 4, we examine their contribution to the early Galactic chemical evolution by comparing our yields with abundances in extremely metal poor stars. Section 5 closes this paper with conclusions and discussion.

2. METHODS & MODELS

The main ingredient of our models is a pair of jets penetrating into a stellar mantle. At the beginning of each calculation, the central part ($M_r \leq M_{\text{REM0}}$) of a progenitor star is displaced by a point mass with transmitted boundary condition at the interface. Without detailed knowledge of how the central object generates energy, we take M_{REM0} as a parameter which expresses the mass of the central remnant when it begins to produce the jets (strictly speaking, when the jets emerge out of the central region).

The jets are injected at the inner boundary along the z -axis with the opening half-angle θ_{jet} . For the property of the jets, we adopt the formalism similar to MacFadyen et al (2001). We must specify two thermodynamical variables and one hydrodynamical variable to determine the property of the jets at their emergence. For these, we take the density, the momentum, and the ratio f of the internal energy to the total energy in the jets. We set $f = 0.01$, so that the internal energy in the jets is negligible. Thus the jets are 'momentum-driven'. To connect the jet properties consistently to the flow around the central region, we assume that the energy and mass fluxes of the jets are proportional to the mass accretion rate. In this formalism, the jet properties are expressed as follows:

$$\begin{aligned} \dot{M}_{\text{jet}} &= \mu \dot{M}_{\text{accretion}} = \rho_{\text{jet}} v_{\text{jet}} A_{\text{jet}} , \\ \dot{E}_{\text{jet}} &= \alpha \dot{M}_{\text{accretion}} \left(e_{\text{thermal}} + \frac{1}{2} \rho_{\text{jet}} v_{\text{jet}}^2 \right) v_{\text{jet}} A_{\text{jet}} (1) \\ f &= \frac{\dot{E}_{\text{thermal}}}{\dot{E}_{\text{jet}}} = 0.01 . \end{aligned}$$

Here A_{jet} is the area where the jets emerge, i.e., $A_{\text{jet}} = 4\pi R_0^2 (1 - \cos(\theta_{\text{jet}}))$ with R_0 the radius of the inner boundary (typically $\sim 10^8 \text{cm}$). Equation (1) leads to the following explicit expression for the jet properties:

$$\begin{aligned} \rho_{\text{jet}} &= \frac{\mu \dot{M}_{\text{accretion}}}{v_{\text{jet}} A_{\text{jet}}} , \\ e_{\text{jet}} &= e_{\text{thermal}} + \frac{1}{2} \rho_{\text{jet}} v_{\text{jet}}^2 = \frac{\alpha \dot{M}_{\text{accretion}} c^2}{v_{\text{jet}} A_{\text{jet}}} , \quad (2) \\ v_{\text{jet}} &= \left(\frac{2\alpha(1-f)}{\mu} \right)^{\frac{1}{2}} c \sim \left(\frac{2\alpha}{\mu} \right)^{\frac{1}{2}} c . \end{aligned}$$

Generally, μ and α are the functions of $\dot{M}_{\text{accretion}}$. For

simplicity, we take them as constants if $\dot{M}_{\text{accretion}} \geq \dot{M}_{\text{critical}}$. When the accretion rate falls down below $\dot{M}_{\text{critical}}$, the injection of jets is turned off. $\dot{M}_{\text{critical}}$ expresses the critical accretion rate at which the central accretion flow changes its characteristics dramatically. Such transition would occur in a hyper-accreting disk by the strong dependence of neutrino cooling on the mass accretion rate (Popham, Woosley, & Fryer, 1999). We set $\dot{M}_{\text{critical}} = 0.2M_{\odot}\text{s}^{-1}$. For the relation between α and μ , we set $\mu = 10\alpha$, so that $v_{\text{jet}} \sim 1.3 \times 10^{10}\text{cm s}^{-1}$ for all the models.

Our models are summarized in the first five columns of Table 1. For the progenitor models, we take the $16M_{\odot}$ and $8M_{\odot}$ He cores of stars with $M_{\text{ZAMS}} = 40M_{\odot}$ and $25M_{\odot}$, respectively, from the solar metallicity models of Nomoto & Hashimoto (1988). The H-rich envelope in the progenitor star is removed and the remaining He star is mapped onto the numerical grids with the outer radii $R_* = 3.7$ and $6.7 \times 10^{10}\text{cm}$ for $40M_{\odot}$ and $25M_{\odot}$, respectively.

With the parameterization described above, we follow hydrodynamics of the explosion. At each time step, we compute $\dot{M}_{\text{accretion}}$ at the inner boundary, and then update the jet properties and the mass of the central remnant (M_{REM}) at the next step. To determine the final central remnant mass and the composition in the ejected materials, it is necessary to follow the hydrodynamics until $\dot{M}_{\text{accretion}}$ becomes very small and the ejecta reaches homologous expansion. This is done by expanding the numerical grids and adding the exponential atmosphere above the surface of the He star when the leading edge of the jets reaches the outer boundary. The hydrodynamical evolution is followed up to $40 \sim 100$ seconds in most runs, so that the expansion becomes nearly homologous.

Roe's scheme based on Riemann solver is applied to a two-dimensional Eulerian hydrodynamical code (Hachisu et al. 1992, 1994). Typically 100×30 zones are used in spherical polar coordinate discretized logarithmically in the radial direction. This relatively coarse zoning is due to the small time steps imposed at the inner boundary as a consequence of large v_{jet} . A typical time step is $\Delta t = R_0 \Delta \theta / v_{\text{jet}} \sim (0.5\pi/30 \times 10^8\text{cm}) / (1.3 \times 10^{10}\text{cm s}^{-1}) \sim 4 \times 10^{-4}$ seconds. We have set the CFL number to be 0.1 so that the calculations are stable, which makes $\Delta t \sim 4 \times 10^{-5}$ seconds. As mentioned above, we have to follow the evolution up to ~ 100 seconds, so that more than 10^6 time steps are needed to run one model. Also, we need to run many models (about 10 models: see Table 1) to investigate the outcome with various jet properties. In addition, the number of points to calculate nucleosynthesis should be proportional to the number of the meshes used in the hydrodynamic calculation, which puts another need for computational time for a higher resolution run.

Despite the practical difficulties mentioned above, the coarse zoning is physically little justifiable. We have performed a convergence test by running model 40A with lower and higher resolutions in Appendix A. We have found that the results do not change significantly, if the number of the meshes is greater than 100×30 (see Appendix A for the details).

We employ equation of state including radiation and e^+e^- pairs in an approximated analytical form (Freiburghaus et al. 1999). The integrated form of Pois-

son equation (Hachisu 1986) handles with both self gravity of a stellar mantle and gravity of a central point mass (in Newtonian limit). In the hydrodynamical calculations, the energies generated by nuclear reactions are omitted. This is justified by the following reason: We have used He star models, so that the original composition of the materials which has burned into ^{56}Ni is heavier than ^4He . The energy generated by the reactions is therefore at most $3 \times 10^{51}\text{ergs} / (M(^{56}\text{Ni})/M_{\odot})$, and even smaller in a typical case because most of the materials burned into ^{56}Ni are heavier than ^{16}O . Because $M(^{56}\text{Ni})$ is of the order of $0.1M_{\odot}$, This energy is about 10–20 % for the models with $E_{51} \sim 1$ and much smaller for the models with $E_{51} \gtrsim 10$.

With the hydrodynamical calculation, we trace thermodynamical histories of individual Lagrangian elements. 3000 particles are used for stellar mantle. At the base of the jet, new particles flow into the numerical domain, and are also traced. These histories are used to calculate nucleosynthesis as post-processing. The reaction network includes 222 isotopes up to ^{71}Ge (Hix, & Thielemann 1996, 1999).

The initial compositions of the particles in the post-processing are taken as follows:

- (1) For those which initially reside above the Si layer in the progenitor star, we use the original composition of Nomoto & Hashimoto (1998).
- (2) For those in the iron core, the initial composition, especially Y_e (i.e., electron molecule number), is uncertain. Guided by the recent investigation on how Y_e affects the resultant yields (Umeda & Nomoto 2002), we take $Y_e = 0.5$ in this region.
- (3) The initial composition of the jet material should wait for detailed study on the flow around the central remnant. Recently Pruet et al. (2003) reported based on the one-dimensional accretion disk model that Y_e in the bulk of the disk wind is close to 0.5. In this study we take $Y_e = 0.5$.

Because of the large uncertainty in the initial composition of the jet material, we restrict ourselves in this paper to parameter space where the mass of the isotopes newly synthesized in the shocked stellar mantles overwhelms the mass contained in the jets. We postpone the whole survey, such as very massive jets, to future works. This should require to follow the accretion process to determined the initial composition and will involve the physics neglected in the present study, e.g., angular momentum transport, nuclear energy generation, and cooling by photodisintegration and neutrino emissions, as well as highly resolved numerical simulation around the central remnant.

3. RESULTS

We perform hydrodynamic calculations for the models in Table 1. The models are named with the numbers describing progenitors' zero-age main-sequence masses (M_{ZAMS}). For $M_{\text{ZAMS}} = 40M_{\odot}$, we examine the parameter dependences in detail.

- (1) Models 40A and 25A are regarded as standard runs in this paper.
- (2) Models 40B and 25B express models with loosely collimated jets.

- (3) Model 40C corresponds to very efficient jets with 5% efficiency in converting the accreted energy into the jets' energy.
- (4) Model 40D is calculated in order to examine dependence on the initial central remnant's mass (M_{REM0}), where the jets are initiated with $M_{\text{REM0}} = 3M_{\odot}$, twice the mass in the standard run.
- (5) Models 40SH, 40SL, and 25S express spherical prompt explosion models, which are calculated to compare the bipolar models with the conventional spherical models using the same numerical code. In their names, S means Spherical and H and L mean High and Low energies.

3.1. Hydrodynamics

The hydrodynamical evolution of the interaction between the bipolar jets and the stellar mantle of model 40A is shown in Figure 2, and on an expanded scale in Figure 3. As the jets run through the stellar mantle, they make configuration which is typical of interaction between jets and surrounding matter (e.g., Khokhlov et al. 1999). At the leading edge of the jets is a working surface which divides the jet matter and the ambient stellar matter. At the working surface, energy is deposited to the stellar material which is pushed sideways to form bow shocks. The shocked material forms the high-pressure cocoon surrounding the jets. It expands laterally to push the stellar material further at the bow shock. The cocoon also pushes the jet material toward the z -axis to help the jet even more collimated (MacFadyen et al. 2001), with itself flowing continuously into behind the jets. After the jets lose the power supply at their bases, the internal structure in the jets and the shocked material tends to be smoothed out, making finally the bipolar explosion.

Figure 3 exhibits the complicated structure of the interaction between the jets and the surrounding matter in the central region. The outflow generated by the jets and the inflow caused by gravity compete with each other during the jet propagation. Strong outflow occurs along the z -axis, while matter continues to accrete onto the central region from the side. The working surface works as the 'jet channel', through which the energy is transported efficiently into the outer layers. In the central region, the energy is deposited less effectively. Thus after the jets are turned off, the central part of the star still continues to accrete.

This leads to important results on the final density structure. In Figure 4, we plot the final density distribution of model 40A along the z -axis and r -axis, as well as that of models 40SH and 40SL. The same plot for the $25M_{\odot}$ star is also given. We note two points which are completely different from spherical (thermal bomb) models.

- (1) In the outer envelope, we find higher velocities in the z -axis than in the r -axis as expected. What is unexpected is that the density distribution is flatter than in spherical prompt models. The matter along the z -axis is dominated by the jet material. Thus the density structure is determined by the jet properties rather than the pre-explosion structure. The latter

affects the final density structure only through the hydrodynamical interaction. Its effect, however, is of less significance than the jet property itself.

The density distribution at high velocities ($v \gtrsim 10^9$ cm s $^{-1}$) is responsible for spectral evolution in early, photospheric phases. Analyzing supernova photospheric spectra indicates the structure in this region. For SNe 1997ef and 2002ap, Mazzali et al. (2000, 2002) derived $\rho \propto v^{-4}$ at $v \gtrsim 3 \times 10^9$ cm s $^{-1}$. They stressed that this was not reproduced by spherical models, and might indicate asphericity in the hypernova explosions. The densities in this region is roughly expressed as $\rho \propto v^{-8}$ for the spherical model 40SH, which is consistent with the previous studies (e.g., Nakamura et al. 2001b). Model 40A results in the density structure in the same region fitted by $\rho \propto v^{-3.6}$. This indeed well agrees with the structure derived by the spectral modeling.

The caveat is that the detailed density structure at the highest velocities along the z -axis depends on how fine structures of the jets are resolved, i.e., on the numerical resolution (see appendix). In appendix, we show it is the case but the overall slope does not depend on the resolution sensitively. Especially, model 40A results in much flatter density distribution than spherical models 40SH and 40SL irrespective of the assumed numerical resolution.

- (2) In the central region, a high density core is formed. It should be noted that such a high density region is found not only along the r -axis, but also along the z -axis. It is really a 'central' core. This is because the jet deposits its energy mostly in the outer layers (i.e., through the working surface), while in the central region the energy deposition is inefficient. Thus the central region continues to fall back onto the center. This produces the central dense core, which agrees with the suggestion that a dense core is the feature of a hypernova explosion according to the spectral analyses of SNe 1998bw and 1997ef (Mazzali et al. 2000, 2001; Maeda et al. 2002).

As Nakamura et al. (2001a) showed that their low energetic models ($E_{51} = 1$ and 7) have ejecta dense enough to compare to the density required to explain the brightness of SN 1998bw at late epochs, and as model 40A has denser core than the spherical models 40SH ($E_{51} = 10$) and 40SL ($E_{51} = 1$), we expect that the dense core in model 40A is capable to reproduce the brightness of SN 1998bw at the late phases. The densities below $\sim 10^8$ cm s $^{-1}$ is enhanced in model 40A roughly by a factor of 100 and 10 compared to the spherical models 40SH and 40SL, respectively. This is close to the value seen in the central region in the light curve modeling for SNe 1998bw, 1997ef, and 2002ap by Maeda et al. (2003), in which we re-examined the light curves of these hypernovae and got good fits to them at the whole epochs both at the peak and late phases.

As noted above, the density structure is determined by the parameterized jet properties which are put by hand. Figure 5 shows the density structure resulted from differ-

ent jet properties. The jet models in general have different density structures from spherical prompt models, and moreover, have flatter density structures at the highest velocities than spherical models. Thus we suggest that the flatter density structure is a typical and distinguished feature of the jet-driven explosions as compared to spherical prompt models. Of course, the detailed structure, e.g., the slope ($\rho \propto v^{-3.6}$ for a particular model 40A), does depend on the assumed jet properties (Fig. 5) and on time variability of the central source which produces the jets. The difference will be useful to distinguish the models in future by comparing the observed and multi dimensional synthetic spectra (e.g., Thomas et al. 2002).

The competition between the outflow and the inflow determines the hydrodynamical and nucleosynthetic outcome in the present models. We note that the final remnant's mass (i.e., M_{REM}) is determined self-consistently by the hydrodynamical evolution, in contrast to the conventional spherical models in which it is treated as a parameter.

How the hydrodynamical results depend on the parameters is summarized in Table 1, where we list some important quantities in characterizing dynamics, i.e., E_{total} , M_{REM} , and $M(^{56}\text{Ni})$ (the last we discuss in the next subsection). Note that E_{total} is the total energy (almost equal to the kinetic energy) at the end of the calculation when the ejecta reaches nearly the homologous expansion, thus being basically the energy deposited by the jets reduced by the gravitational binding energy of the ejecta. In Figure 6, we show the evolution of the mass of the central compact remnant, M_{REM} . The results are summarized as follows.

- (1) For a given set of the jet parameters, the explosion of the $40M_{\odot}$ star is more energetic than the $25M_{\odot}$ star. This is because the gravity is stronger in a more massive star, making an accretion rate higher and thus the explosion more energetic. At the same time, a higher accretion rate leads to a more massive central remnant.
- (2) The jet with a wider opening angle θ_{jet} induces a less energetic explosion. The larger θ_{jet} is, more efficiently the energy is transported from the jets to the surrounding stellar envelopes. The bow shock running through the envelope tries to push material outward. $\dot{M}_{\text{accretion}}$, therefore, falls off rapidly in models 40B and 25B (larger θ_{jet}) than in models 40A and 25A (smaller θ_{jet}). Small $\dot{M}_{\text{accretion}}$ leads to a less energetic explosion.
- (3) The final remnant's mass depends on θ_{jet} . It is related to the progenitors' mass as follows:
 - (3-1) For the $40M_{\odot}$ star, model 40B (large θ_{jet}) forms a more massive remnant than 40A. Figure 6 shows that the decrease in the accretion rate after turning off the jets is slower in 40B than 40A. When the jets are turned off (~ 1 sec in 40B), model 40B still has a mantle of more than $14M_{\odot}$. The energy injected by the jets (E_{jet}) till that time is $\sim 6 \times 10^{51}$ ergs, while the binding energy of the whole star is $\sim 7 \times 10^{51}$ ergs. This binding energy is comparable to and indeed larger than E_{jet} . However, it does not mean

that the explosion must be failed. Because the energy is mainly deposited in the outer layers along the z axis, matter continues to accrete in the central region. It reduces the final mass of the ejecta and thus the energy required to set the outward motion against gravitation. It can (and does in 40B) induce the explosion. In model 40A, at the time the jets are turned off, E_{jet} greatly exceeds the binding energy.

- (3-2) For the $25M_{\odot}$ star, model 25B forms a smaller mass remnant than model 25A. At turning off the jets, even smaller E_{jet} ($\sim 3 \times 10^{51}$ ergs) in model 25B is enough to eject the remaining stellar mantle without further accretion, because of the much smaller binding energy ($\sim 2 \times 10^{51}$ ergs) of the $25M_{\odot}$ star than the $40M_{\odot}$ star.
- (4) For larger efficiency of the central engine, a more energetic explosion takes place. Also the central remnant is less massive, because E_{jet} is much larger than the binding energy and the lateral expansion keeps the accretion rate small.

3.2. Production of ^{56}Ni

Regarding nucleosynthesis, we first direct our attention to the production of ^{56}Ni . The ejected mass of ^{56}Ni , $M(^{56}\text{Ni})$, is listed in Table 1. The models presented here differ from spherical thermal bomb models mainly in two respects.

- (1) The time scale for the energy release from the central remnants can be comparable to the hydrodynamical time scale for the jet propagation.
- (2) The explosion proceeds mainly along the z-axis.

We first show how the time scale of the explosion affects the final ^{56}Ni mass produced at the shocked stellar material. $M(^{56}\text{Ni})$ can be estimated as follows, which generalizes the equation (2) of Nakamura et al. (2001b) for a prompt explosion model. In the following derivation, the energy input rate (\dot{E}_{jet}) is assumed to be constant for simplicity.

Let t_f be the time when the jets lose the power supply at their bases, i.e., $\dot{E}_{\text{jet}} \times t_f = E_{\text{jet}}$. The region having experienced the shock wave is dominated by radiation, and contains the energy which is injected till the time t . Assuming spherical symmetry, the following approximate relation holds.

$$\frac{4\pi}{3}R^3aT^4 = \begin{cases} \dot{E}_{\text{jet}}t & \text{for } t < t_f, \\ \dot{E}_{\text{jet}}t_f = E_{\text{jet}} & \text{for } t \geq t_f. \end{cases} \quad (3)$$

The position of the shock may be approximated as $R = Vt$. Using the approximations of $V \sim \sqrt{\dot{E}_{\text{jet}} \min(t, t_f) / M_{\text{sw}}}$ for the shock velocity and $M_{\text{sw}} = (4\pi/3)R^3\bar{\rho}$ for the mass of the swept up material, we get the following equations for the post-shock temperature when the shock arrives at R (here we take $\bar{\rho} = 10^6 \text{ g cm}^{-3}$).

$$T_9 \sim \begin{cases} 6\dot{E}_{51}^{1/6}R_8^{-1/3} & \text{for } t < t_f, \\ 20E_{52}^{1/4}R_8^{-3/4} & \text{for } t \geq t_f. \end{cases} \quad (4)$$

Here $X_n = X/10^n$ in cgs unit. T_9 is plotted as a function of the shock radius R in Figure 7. For given \dot{E}_{jet} and E_{jet} (or, equivalently, t_f), one gets two curves in the $M_r - T_9$ ($R - T_9$) plot, at $t < t_f$ and $t \geq t_f$, respectively. $R(t_f)$ is given as the intersection of the two curves and estimated as

$$R_8(t = t_f) \sim 30 \dot{E}_{51}^{1/5} (t_f/10\text{s})^{3/5} \quad (5)$$

by setting $t = t_f$ in equation (3) and in the expression for R . In the case t_f is very small, the relations above reduce to those in a prompt explosion model.

With Figure 7, $M(^{56}\text{Ni})$ can be estimated as the mass contained in the regions with $T_9 > 5$. In the prompt explosion with $E_{51} = 10$ and $M_{\text{ZAMS}} = 40M_\odot$, $T_9 > 5$ is satisfied up to the enclosed mass $M_r \sim 3M_\odot$, among which $\sim 1M_\odot$ is reprocessed into ^{56}Ni and the rest falls back onto the central remnant. This is consistent with the result of model 40SH within a factor of a few.

The noticeable difference from the prompt models arises when t_f is large. Let $\dot{E}_{51} = 1$ and $t_f = 10$ sec so that $E_{51} = 10$ being the same as in model 40SH. In this case, however, the region with $T_9 > 5$ is small (up to the enclosed mass $M_r \sim 1.8M_\odot$), so that the production of ^{56}Ni is smaller than 40SH, as also found by Nagataki et al. (2003). The reason is simple. At a given time t , the total energy injected till that time is smaller in this kind of models than in prompt explosion models. At later times, matter already begins to expand, so that continuous energy deposition yields lower temperature because of larger ejecta volume.

Let us look at the other case where t_f is sufficiently small, e.g., $t_f = 1$ sec. This is shorter than the typical hydrodynamical time scale, as it takes the jets $\gtrsim 4$ s to propagate through the entire stellar radius. For a given final explosion energy, e.g., $E_{51} = 10$ (thus $\dot{E}_{51} = 10$), the energy injection is finished before the post-shock temperature falls off below $T_9 = 5$. Therefore, the expected $M(^{56}\text{Ni})$ is similar to the corresponding prompt model.

Deviation from spherical symmetry makes the production of ^{56}Ni less efficient for given E . Given the opening half-angle $\theta_{\text{jet}} = 15^\circ$, the solid angle subtended by the jets is $\Omega = 2 \times 2\pi(1 - \cos\theta_{\text{jet}}) \sim 4\pi/30$. This in effect corresponds to the enhancement of the isotropic energy by a factor $(4\pi/\Omega)$ in this direction, i.e.,

$$\frac{\Omega}{4\pi} \frac{4\pi}{3} R^3 a T^4 \sim \dot{E}_{\text{jet}} t. \quad (6)$$

For $\dot{E}_{51} = 10 \text{ s}^{-1}$ with $t_f = 1$ s, matter up to $M_r \sim 5M_\odot$, i.e., up to larger R than the spherical case, is heated to $T_9 > 5$. For $M_{\text{cut}} = 1.5M_\odot$, the ejected $M(^{56}\text{Ni})$ is about $0.1M_\odot$ (after reduced by the factor of $\Omega/4\pi$). It roughly explains $M(^{56}\text{Ni})$ in model 40A. This is much smaller than $M(^{56}\text{Ni}) \gtrsim 1.0M_\odot$ in the spherical model with the same parameters. The effect of asphericity, therefore, is to reduce $M(^{56}\text{Ni})$ for given E_{jet} . The reason is as follows: though the region with $T_9 > 5$ is elongated to the outer, lower density regions in a specific direction in the aspherical models, the mass in such outer regions is small. The mass of the region with $T_9 > 5$ in the bipolar models, therefore, is reduced by a factor $\sim (\Omega/4\pi)$.

Also the initial mass of the compact remnant, M_{REM0} , greatly affects the ^{56}Ni production. Model 40D produces

very little amount of ^{56}Ni . The reason for this can be seen in Figure 7. With $E_{51} \sim 10$, the region with $T_9 > 5$ extends to $M_r \sim 5M_\odot$ along the z -axis as discussed for model 40A. Because M_{REM0} is as large as $3M_\odot$ in model 40D, $M(^{56}\text{Ni})$ is estimated to be smaller than $0.1M_\odot$. Thus, with $M_{\text{REM0}} > 3M_\odot$, even a hypernova-like explosion produces much smaller $M(^{56}\text{Ni})$ than typical supernovae. In other words, $M(^{56}\text{Ni})$ may not be connected with E_{jet} .

We note that $M(^{56}\text{Ni})$ in Figure 1 has been obtained through analyzing light curves and spectra. Figure 1 does not imply the absence of hypernovae/supernovae with little $M(^{56}\text{Ni})$ such as model 40D, as the corresponding SNe Ib/c must be too faint to be observed directly. Actually, the existence of such ^{56}Ni -deficient supernovae is inferred from extremely metal-poor stars, which we discuss later.

On the other hand, $M(^{56}\text{Ni})$ obtained from modeling light curves and spectra shows that there exist hypernovae with ejection of large $M(^{56}\text{Ni})$, highlighted by $M(^{56}\text{Ni}) \sim 0.5M_\odot$ in SN 1998bw.

To account for the latter case, i.e., hypernovae with $M(^{56}\text{Ni}) \gtrsim 0.1M_\odot$, one of the following conditions must be satisfied.

- (1) To produce ^{56}Ni in the shocked stellar material, M_{REM0} must be sufficiently small ($M_{\text{REM0}} \lesssim 2M_\odot$) and the energy injection rate sufficiently large ($\dot{E}_{\text{jet}} \gtrsim 10^{52} \text{ ergs s}^{-1}$). We note that the models presented here except for model 40D produce $\gtrsim 0.1M_\odot$ $M(^{56}\text{Ni})$.
- (2) The alternative way is to eject ^{56}Ni from the inner most region, e.g., in a disk wind from the accretion disk surrounding the central object (MacFadyen & Woosley, 1999; MacFadyen 2003; see also Introduction). This would correspond to taking larger μ than in our models (and maybe larger θ_{jet}). In this case, the resultant flow from the inner region is more massive and slow. This possibility should be examined in more detail. In the present models, the mass carried in the jets is small (with $E_{51} = 10$, $\alpha = 0.01$, and $\mu = 0.1$, $M_{\text{jet}} \sim 0.05M_\odot$), so that the newly synthesized elements are dominated by those in the shocked stellar material.

Also, as shown in Figure 8, the present models predict anti-correlation between $M(^{56}\text{Ni})$ and M_{REM} (thus correlation between $M(^{56}\text{Ni})$ and M_{ej}) for a given progenitor. For larger M_{REM} , the mass available to ^{56}Ni production is smaller. In addition, larger M_{REM} corresponds to longer time scale for the energy injection, i.e., longer t_f . Both effects suppress the production of ^{56}Ni .

Figure 9 shows the distribution of ^{56}Ni (which decays into ^{56}Fe) and ^{16}O at the homologous expansion phase for the models with $M_{\text{ZAMS}} = 40M_\odot$ (we omit model 40D, because it produces very little amount of ^{56}Ni). Along the jet axis, matter experiences a strong shock, thus being reprocessed through complete silicon burning. It produces a large amount of ^{56}Ni . On the other hand, matter continues to accrete from the side. When the mass accretion rate becomes low enough, matter gets outward momentum large enough to compete with inflow. The peak temperatures of those materials are, however, too low to cause

significant nuclear reactions. Thus their isotopic patterns reflect those of initial composition before the gravitational collapse. The result is characterized by the high velocity ^{56}Ni -rich matter along the jet, and low velocity ^{16}O -rich matter near the center. Maeda et al. (2002) and Mazzali et al. (2001) discussed that such configuration could naturally explain nebular spectra of SN 1998bw.

The comparison among the models in Figure 9 reveals how the overall asphericity is affected by the property of the jets. A larger opening angle (θ_{jet}) leads to a less aspherical explosion as expected (40A vs. 40B). Larger efficiency (α) leads to a more energetic and a less aspherical explosion (40A vs. 40D). The reason for the latter is as follows: a stronger shock (larger α) deposits a larger amount of energy in the surrounding material at the working surface and causes a stronger lateral expansion. These are also obvious in Figure 6, which shows that models 40B and 40C keep the accretion rate smaller than 40A, indicating the stronger lateral expansion. In addition, final kinetic energies listed in Table 1 support this explanation. The final energies of models 40B and 40C are smaller than $E_{51} = 10.9 \times (\alpha/0.01)$, which is expected if the accretion rate is the same as in model 40A. This result is consistent with MacFadyen et al. (2001), who examined the interaction between bipolar jets and envelopes of failed supernovae by the similar formalism we adopt in this paper. We note that in model 40A, the jet material really drills the hole along its way up to the stellar surface.

3.3. Nucleosynthesis

In this section, we discuss further details of the nucleosynthetic feature, i.e., the isotopic composition of the bipolar explosions. The isotopic abundance patterns of model 40A along the z -axis and the r -axis, as well as that averaged over all directions are shown in Figure 10. The abundance pattern of the spherical model 40SH is also shown.

In explosive nucleosynthesis in a supernova explosion, the isotopic ratios depend on the peak temperature attained at the passing of the shock wave as follows (e.g., Thielemann, Nomoto, & Hashimoto. 1996):

- (1) The regions with $T_9 > 5$ undergo complete silicon burning and α -rich freezeout to produce ^{56}Ni abundantly, as discussed in the previous section. Higher temperatures (or lower densities at given T_9) result in stronger α -rich freezeout, thus producing ^{44}Ti , ^{64}Ge , and ^{59}Cu more abundantly.
- (2) The regions with $4 < T_9 < 5$ undergo incomplete silicon burning. Beside the dominant fuel nuclei ^{28}Si and ^{32}S , the burning produces ^{40}Ca and some iron-peak isotopes including ^{55}Co .
- (3) At $3 < T_9 < 4$, explosive oxygen burning takes place. ^{28}Si , ^{32}S , ^{36}Ar , and ^{40}Ca are abundantly produced at the consumption of ^{16}O .
- (4) At $T_9 < 3$, explosive nucleosynthesis does not proceed so much. Though a fraction of fuel nuclei, mostly ^{12}C , are converted to heavier nuclei by carbon burning, this does not significantly change the isotopic composition. Thus, the isotopic composition of

this region is almost the same as in the pre-explosion star, i.e., ^{16}O , ^{12}C , and ^4He .

3.3.1. Spherical Models

In spherical models, higher temperature is attained in inner regions, because the temperature after the passing of the shock wave decreases as the shock wave moves outward ($T \propto R^{-3/4} E^{1/4}$ where R is the radius of the position of the shock wave; see equations (3) and (4)). Thus, spherical models predict in general the following pattern in order of increasing radii: strong α -rich freezeout (e.g., ^{44}Ti (Ca), ^{59}Cu (Co), ^{64}Ge (Zn)), complete silicon burning (e.g., ^{56}Ni (Fe)), incomplete silicon burning (e.g., ^{40}Ca , ^{55}Co (Mn)), oxygen burning (e.g., ^{28}Si , ^{32}S , ^{36}Ar), and no significant burning (e.g., ^4He , ^{12}C , ^{16}O). (The stable isotopes after β -decays are indicated in parenthesis.) This feature in spherical models is evident in Figure 10d.

We are interested in the isotopic yields in the whole ejecta, as these are responsible for the Galactic chemical evolution. In conventional spherical models, the yields depend on the 'mass cut', which divides the stellar material into those finally ejected and accreted onto a central remnant. We show how the resultant yields depend on M_{cut} (the mass contained below the mass cut) in spherical models, to clarify the difference between spherical models and the bipolar models in the later part.

Figure 11 shows the isotopic patterns of spherical model 40SH for different mass cuts. The isotopic distribution in the ejecta of model 40SH shown in Figure 10d explains the behavior. For large M_{cut} , $M(^{56}\text{Ni})$ is small and the isotopes produced in the deepest regions such as ^{64}Zn (produced as ^{64}Ge) and ^{59}Co (produced as ^{59}Cu) are not ejected (Figure 11a). For small M_{cut} , on the contrary, a large amount of ^{64}Zn and ^{59}Co are ejected (Figure 11b). The isotopes with mass numbers $A \lesssim 40$ are produced mainly in the layers well above the mass cut, so that their abundances do not depend on the mass cut. For these elements ($A \lesssim 40$), therefore, the abundances normalized by iron, i.e., $[\text{X}/\text{Fe}] = \log(\text{X}/\text{Fe}) - \log(\text{X}/\text{Fe})_{\odot}$, are smaller for larger M (^{56}Ni). The spherical models thus predict that the ejecta with smaller M_{cut} has larger $[(\text{Zn}, \text{Co})/\text{Fe}]$ and smaller $[(\text{O}, \text{Mg}, \text{Mn})/\text{Fe}]$ (the latter because of larger $M(^{56}\text{Ni})$), unless the mixing and fallback process takes place (Umeda & Nomoto 2002). Such a correlation is not the case for the bipolar models because of the following reason.

3.3.2. Bipolar Models

Figure 12 shows the peak temperatures of individual mass particles against the densities at the passing of the shock wave. At a given density, the peak temperatures spread over a wide range, in contrast to the single line in the $\rho - T$ plane in spherically symmetric models.

Along the z -axis, the stronger shock heats up the stellar material to higher temperatures. Along the r -axis, temperatures are lower because of the weaker shock and densities are higher because of mass accretion. Therefore, the materials along the z -axis occupy the high entropy region in the $\rho - T$ plane, while those in the r -axis form the lowest bound of entropy. As a result, the peak temperatures distribute in a wide range for a given density. The variation in temperatures in model 40A is much larger than the def-

erence between the spherical models 40SH ($E_{51} = 10$) and 40SL ($E_{51}=1$) (Fig. 12).

Compared with the spherical model with the same E (40SH), the entropy of material along the z -axis of model 40A is higher for the same density at $\rho \lesssim 10^7 \text{ g cm}^{-3}$. At $\rho \gtrsim 10^7 \text{ g cm}^{-3}$, the entropy along the z -axis of model 40A is as low as that in the spherical model 40SH. This is because the energy injection by the jets in model 40A is not completed when the shock reaches the corresponding radius, so that the rise in the temperature is suppressed as discussed in the previous section.

In hydrodynamics, materials along the r -axis with lower temperature accrete onto the center, while materials undergoing higher temperatures are ejected along the z -axis. Thus, the bipolar explosions eject preferentially higher temperature matter as shown in Figure 12.

This can also be seen in Figure 10. Along the z -axis, matter experiences strong α -rich freezeout to synthesize ^{64}Ge , ^{44}Ti , ^{56}Ni and is brought up to the surface. Along somewhat off-axis, matter experiences lower T_9 , thus undergoing incomplete silicon burning to produce ^{55}Co and oxygen burning to produce ^{28}Si . The latter are heated by the bow shock expanding sideways and flows into the side. As the energy deposited is smaller than along the z -axis, some of them experience circulation and flow into behind the α -rich freezeout isotopes.

The matter aside the jets moves toward the center, which forms the oxygen-rich high density core (section 3.1). This O-rich core is seen in both plots along the z -axis and along the r -axis. Thus, the result is the inversion of the velocities among various isotopes along the z -axis, as compared with spherical models: ^{64}Zn , ^{56}Ni , and ^{44}Ti at the highest velocity, ^{55}Co and ^{28}Si at the intermediate velocity, and ^{16}O at the lowest velocity. This is the case not only along the z -axis, but also for the average over all the direction (Fig. 10c). This feature is due to the action between the jets and gravity modeled in this study, and was not examined to this extent in the simpler models in the previous studies (Nagataki 2000; Maeda et al. 2002).

Figure 13 demonstrates that ^{64}Zn is ejected with higher velocities than ^{55}Mn . Here Zn represents the products of strong α -rich freezeout in complete Si burning, while Mn represents the products of incomplete Si burning. The velocity inversion between these elements is obvious. The bipolar model predicts that Zn is ejected with higher velocities than Mn, in contrast to spherical models.

The above features are seen in the isotopic yields of the bipolar models shown in Figure 14, Tables 2-4 (after β -decays), Tables 5-7 (before β -decays), and Table 8 (Radioactive isotopes). Comparison between 40A and 40SH (spherical) reveals the following characteristics in the bipolar models:

- (1) Production of heavy isotopes with $A \gtrsim 60$, especially ^{64}Zn and ^{59}Co , is enhanced relative to ^{56}Fe . This is attributed to the high entropy of matter ejected along the z -axis. Comparison between Figures 11 and 14 shows that the yields of these isotopes relative to ^{56}Fe (^{56}Ni) in 40A are similar to those of 40SH with large M (^{56}Ni) (i.e., small M_{cut}). Both models are dominated by the material which experiences strong α -rich freezeout. For the same reason, $^{55}\text{Mn}/^{56}\text{Fe}$ ratio is suppressed.

- (2) On the other hand, model 40A produces a relatively small amount of ^{56}Ni compared to 40SH with small M_{cut} . As a result, the ratios $[(^{16}\text{O}, ^{24}\text{Mg})/^{56}\text{Fe}]$ are much larger in 40A. These ratios in model 40A are close to those in 40SH with small ^{56}Ni (large M_{cut}).

3.3.3. α -rich freezeout and complete silicon burning products

Regarding the ejection of isotopes produced in strong α -rich freezeout, the masses of ^{44}Ti and ^{64}Ge (which decay into ^{44}Ca and ^{64}Zn , respectively) are shown against $M(^{56}\text{Ni})$ in Figure 15. Because the bipolar models preferentially eject the materials experiencing higher temperatures (higher entropies) in complete silicon burning, the ratios $^{44}\text{Ti}/^{56}\text{Ni}$ and $^{64}\text{Ge}/^{56}\text{Ni}$ are significantly larger in the bipolar models than spherical models (except for model 25B, as this is a very weak explosion with $E_{51} = 0.6$).

The previous study on aspherical explosions by Maeda et al (2002) attained $M(^{44}\text{Ti}) \sim 1.6 \times 10^{-3} M_{\odot}$ and $M(^{64}\text{Ge}) \sim 1.6 \times 10^{-4} M_{\odot}$ for $M(^{56}\text{Ni}) \sim 0.4 M_{\odot}$ (their model C), thus $^{44}\text{Ti}/^{56}\text{Ni}$ and $^{64}\text{Ge}/^{56}\text{Ni}$ relative to the solar values are ~ 3.4 and ~ 0.5 , respectively.

In the present models, $M(^{44}\text{Ti})$, $M(^{56}\text{Ni})$, and the ratio $^{44}\text{Ti}/^{56}\text{Ni}$ are smaller than in Maeda et al. (2002). The smaller $^{44}\text{Ti}/^{56}\text{Ni}$ is mainly attributed to the time scale of the energy injection as discussed in the previous section: the present models are driven by jets which are injected over a few seconds (as they are powered by accretion), while Maeda et al. (2002) assumed prompt aspherical explosions. Because the continuous energy injection leads to lowering the post-shock temperature (section 3.2), the production of ^{44}Ti is suppressed as compared to the prompt explosions.

For ^{64}Ge (which decays into ^{64}Zn), the present models predict much larger $^{64}\text{Ge}/^{56}\text{Ni}$ ratio than Maeda et al (2002). This mainly stems from the difference in Y_e in the deepest region: In the present study, we assumed $Y_e = 0.5$ down to the mass cut. Because the production of ^{64}Ge is very sensitive to Y_e and most abundantly produced with $Y_e = 0.5$ as this isotope has the same number of protons and neutrons, this choice results in a large amount of ^{64}Ge (Umeda & Nomoto 2002).

In spherical models without any mixing, ejecta with large ratios of $(^{44}\text{Ti}, ^{64}\text{Ge})/^{56}\text{Ni}$ relative to the solar ratios should contain such a large amount of ^{56}Ni as $M(^{56}\text{Ni}) \gtrsim 0.4 M_{\odot}$. In contrast, bipolar models predict large ratios of $M(\alpha\text{-rich freezeout})/M(^{56}\text{Ni})$ relative to the solar values in ejecting relatively small amount of ^{56}Ni ($\sim 0.1 - 0.2 M_{\odot}$). This feature may have significant implication for the abundances in extremely metal-poor stars, as discussed in the coming section.

3.3.4. Incomplete silicon burning products

Incomplete silicon burning in the bipolar models shows different characteristics as compared to spherical models. Figure 16 exhibits the ratios, $[\text{Ti}/\text{Ca}]$, $[\text{Ca}/\text{Si}]$, $[\text{S}/\text{Si}]$, $[\text{Si}/\text{O}]$, and $[\text{C}/\text{O}]$ (where $[\text{X}/\text{Y}] \equiv \log(\text{X}/\text{Y}) - \log(\text{X}/\text{Y})_{\odot}$) as a function of the remnant's mass (M_{REM}).

Ti and Ca are dominated by ^{48}Ti and ^{40}Ca , respectively, which are produced by incomplete silicon burning. ^{48}Ti is a decay product of ^{48}Cr whose synthesis requires higher

temperature than ^{40}Ca . This is analogous to the relation between strong α -rich freezeout products and ^{56}Ni . Thus, the trend of Ti/Ca ratio is expected to be the same as the trends of $(^{44}\text{Ti}, ^{64}\text{Ge})/^{56}\text{Ni}$ (§3.3.3).

Figure 16 shows that the Ti/Ca ratio is basically larger for smaller M_{REM} , and thus for larger ^{56}Ni (Figure 8), with the exception of the very weak explosion model 25B. This relation and the variation of [Ti/Ca] as a function of M_{REM} are qualitatively similar to those seen in spherical models. However, we should note that M_{REM} varies in a much wider range ($1.5 - 11M_{\odot}$) in the bipolar models than in the spherical models ($< 3M_{\odot}$).

The trend in [Ca/Si] is similar to [Ti/Ca] for the same reason. For large M_{REM} , however, the difference between [Ti/Ca] and [Ca/Si] becomes evident. As ejected Si is produced both before and during the explosion, the behavior of the element ratios with respect to Si is complicated as will be discussed in the next subsection.

3.3.5. Oxygen burning and hydrostatic burning products

S, Si, O, Mg, and C are produced in hydrostatic burning before the explosion. During the explosion S and Si are also produced by explosive oxygen burning. In spherical models, all these elements are produced well above the mass cut, so that their abundance ratios are basically independent of M_{cut} as is evident in Figure 16. However, this is not the case for the bipolar models, as shown by the large variations of these ratios in Figure 16.

First, the abundance ratios depend on the progenitor's mass as follows:

- (1) For $M_{\text{ZAMS}} = 40M_{\odot}$, these ratios show large variations. The difference from the spherical models is larger for larger M_{REM} .
- (2) For $M_{\text{ZAMS}} = 25M_{\odot}$, the bipolar models 25A and 25B produce similar ratios to the spherical model 25S.

The accretion of heavy elements onto the central remnant is responsible for the variation of these abundance ratios. Since the final remnant mass, M_{REM} , is a measure of the amount of accreted material, accretion yields the correlation between these ratios and M_{REM} . Such a correlation is more pronounced in more massive stars because M_{REM} takes a larger range of values.

- (3) Si, S: In spherical models, Si and S in presupernova stars are mostly burned into Fe-peak elements during the explosion. However, these elements are newly synthesized by explosive O-burning and ejected with $[\text{Si/S}] \sim 0$. In the bipolar models, the silicon layer aside the jets are ejected without undergoing significant explosive burning. The ejected masses of Si and S produced during the explosion are comparable to those produced before the explosion.

In the presupernova star, S is more centrally concentrated than Si, thus accreting more easily onto the central remnant. This yields smaller [S/Si] for larger M_{REM} . This might explain the observed low S/Si ratio in M87 (Matsushita, Finoguenov, & Böhringer, 2003). As Si and S are produced in the deeper region than O, larger M_{REM} means a larger amount of Si

and S in the accreted matter, thus leading to smaller $[(\text{S}, \text{Si})/\text{O}]$.

In model 40D, however, [Si/O] is larger than that in models 40A and 40B with smaller M_{REM} . For very large M_{REM} like in 40D, Si in the presupernova star is totally accreted onto the center, thus Si ejected are dominated by the explosive burning products. The amount of Si, therefore, does not decrease with larger M_{REM} anymore. The amount of O, however, even decreases with larger M_{REM} as O is distributed in the progenitor star in the wide range. Thus, for model 40D, [Si/O] is large.

- (4) O, C: The carbon-rich layer is located above the oxygen-rich layer, so that O more easily accretes onto the central remnant. Therefore, larger [C/O] results from larger M_{REM} .

4. IMPLICATIONS ON ABUNDANCES IN EXTREMELY METAL-POOR STARS

Figure 17 shows $[(\text{Si}, \text{S}, \text{Sc}, \text{Ti}, \text{Cr}, \text{Mn}, \text{Co}, \text{Zn})/\text{Fe}]$ against [Mg/Fe] for the bipolar models and the spherical models (with different M_{cut}). Figure 17 clearly shows that the yields of the bipolar models are different from spherical models, irrespective of the choice of M_{cut} . The features of the bipolar explosions are summarized as follows.

- (1) Si, S: $[(\text{Si}, \text{S})/\text{Fe}]$ are smaller than in spherical models, because of the substantial loss of presupernova Si and S by accretion. This is evident in more massive progenitors with $M_{\text{ZAMS}} = 40M_{\odot}$, since a more massive star undergoes a larger amount of mass accretion. The difference between the bipolar models and the spherical models is larger for [S/Fe] than [Si/Fe], especially for larger M_{REM} (i.e., larger [Mg/Fe]), because of more centrally concentrated distribution of S than Si.
- (2) Sc, Ti: For explosions with larger energies and asphericity (models 40A, 40C, and 25A), $[(\text{Sc}, \text{Ti})/\text{Fe}]$ are larger compared to the less energetic and spherical models, because the production of Sc and Ti is enhanced at strong α -rich freezeout, i.e., high entropy condition, in complete Si burning. The enhancement is particularly strong for Sc, as its production is very sensitive to the entropy and needs very low density (i.e., high entropy). For 40A, 40C, and 25A $[\text{Sc/Fe}]$ is reached $\gtrsim 0.0$, while $[\text{Sc/Fe}] \lesssim -1.0$ for spherical models irrespective of M_{cut} . The caveat is that the production of Sc is very sensitive to the numerical resolution employed (see Appendix), though qualitatively enhancement of [Sc/Fe] is found irrespective of the numerical resolution. Future higher resolution studies are needed to quantitatively confirm the above result.
- (3) Cr, Mn: For a given [Mg/Fe], $[(\text{Cr}, \text{Mn})/\text{Fe}]$ in the bipolar models are much smaller than in the spherical models. Cr and Mn are mainly produced in the incomplete silicon burning region, i.e., at lower peak-temperatures than complete silicon burning which produces Fe. Since the bipolar explosions preferentially eject higher temperature matter, $[(\text{Cr}, \text{Mn})/\text{Fe}]$ are smaller than in spherical models.

- (4) Co, Zn: For a given $[\text{Mg}/\text{Fe}]$, $[(\text{Co}, \text{Zn})/\text{Fe}]$ in the bipolar models are much larger than in the spherical models. Because these ratios are larger at higher entropy (Umeda & Nomoto, 2002), and the ejection of higher entropy matter is enhanced in the bipolar models, $[(\text{Co}, \text{Zn})/\text{Fe}]$ are significantly enhanced in the bipolar models.

The bipolar supernova/hypernova explosions may have significantly contributed to the early Galactic chemical evolution. Abundances in extremely metal-poor stars provide us with important clues to know what were the first supernova explosions and what were the first stars in Galaxy.

At early phases, the Galaxy was not chemically well-mixed yet. Extremely metal-poor stars store the chemical information of an individual (core-collapse-induced) supernova, because those stars are likely to have been contaminated by only a single supernova (Audouze & Silk 1995; Shigeyama & Tsujimoto 1998). This expectation has led to many attempts to compare abundances in extremely metal-poor stars with theoretical supernova yields (e.g., Umeda & Nomoto 2002).

In this section, we compare the yields of the bipolar models and the abundances in extremely metal-poor stars. It should be taken in mind that the models presented here are solar metallicity models (see section 2). Therefore, we are mainly concerned in this section with explosive burning products and major isotopes of intermediate elements, which are little affected by the metallicity of the progenitor models.

4.1. Iron-Peak Elements

Observational studies on metal-poor halo stars have shown that there exist interesting trends in the abundances of iron peak elements for $[\text{Fe}/\text{H}] \lesssim -2.5$ (McWilliam et al. 1995; Ryan, Norris, & Beers 1996; Primas et al. 2000; Blake et al. 2001). Both $[\text{Cr}/\text{Fe}]$ and $[\text{Mn}/\text{Fe}]$ decrease toward smaller $[\text{Fe}/\text{H}]$, while $[\text{Co}/\text{Fe}]$ and $[\text{Zn}/\text{Fe}]$ increase to reach $\sim 0.3 - 0.5$ at $[\text{Fe}/\text{H}] \sim -3$ (Figure 18). Also $[(\text{O}, \text{Mg})/\text{Fe}]$ are as large as ~ 0.5 for $[\text{Fe}/\text{H}] \lesssim -2.5$, indicating that the amount of Fe was not excessively large in the ejecta of supernovae which were responsible for forming those stars (see also section 3.2 on the production of ^{56}Ni which decays into ^{56}Fe).

The large ratios of $[\text{Co}/\text{Fe}]$ and $[\text{Zn}/\text{Fe}]$ have not been predicted in previous Nucleosynthetic yields of spherical thermal bomb models. As pointed out by Umeda & Nomoto (2002), it is difficult to reproduce these ratios together with $[(\text{O}, \text{Mg})/\text{Fe}] \sim 0.4 - 0.5$. Co and Zn are produced in the deepest layer of the ejecta through strong α -rich freezeout. Mg and O, on the other hand, are mostly produced by hydrostatic burning, so that these yields are insensitive to the explosion. The ejection of a large amount of Zn and Co inevitably leads to the ejection of a large amount of Fe (produced as ^{56}Ni), because Fe is synthesized not only in the deep layer with Zn, but also in the outer regions with Si. This decreases $[\text{Mg}/\text{Fe}]$ and $[\text{O}/\text{Fe}]$ (Figure 11b), contrary to the observations. With $[\text{Mg}/\text{Fe}] \sim 0.4 - 0.5$, $[(\text{Co}, \text{Zn})/\text{Fe}] \lesssim 0.0$ and even much smaller than this for most of the case (Figure 11a).

To reproduce the observed trends of increasing $[(\text{Zn}, \text{Co})/\text{Fe}]$ and decreasing $[(\text{Mn}, \text{Cr})/\text{Fe}]$ toward smaller

$[\text{Fe}/\text{H}]$, nucleosynthesis in the SNe which are responsible for the chemical enrichment of small $[\text{Fe}/\text{H}]$ stars should have the following characteristics.

- (1) Matter which undergoes complete Si-burning should be ejected abundantly without ejecting much incomplete Si-burning products.
- (2) The mass ratio between the complete Si-burning products to incomplete Si-burning products should be larger at lower metallicities.

One possible model to realize the above nucleosynthesis is the deep mass cut (small M_{cut}). As shown in Figure 11, smaller M_{cut} makes $[(\text{Zn}, \text{Co})/\text{Fe}]$ larger and $[(\text{Mn}, \text{Cr})/\text{Fe}]$ smaller simultaneously. Figures 17e-17h also clearly show these trends with varying M_{cut} , where smaller $[\text{Mg}/\text{Fe}]$ results from smaller M_{cut} . In this case, however, $[(\text{O}, \text{Mg})/\text{Fe}]$ are too small because of the presence of a large amount of Fe above the mass cut (Figure 11b). Figures 17e-17h show that in the spherical models, $[\text{Cr}/\text{Fe}] \lesssim 0.0$, $[\text{Mn}/\text{Fe}] \lesssim -0.5$, and $[(\text{Co}, \text{Zn})/\text{Fe}] \gtrsim 0.0$ as observed in the very metal-poor stars require so deep a mass cut which results in $[\text{Mg}/\text{Fe}] \lesssim 0.2$, contrary to the observations.

We point out that the bipolar models naturally account for these features. Large $[(\text{Co}, \text{Zn})/\text{Fe}]$, small $[(\text{Cr}, \text{Mn})/\text{Fe}]$, and large $[(\text{O}, \text{Mg})/\text{Fe}]$ are simultaneously realized as seen in Figures 14 and 17. Compared with the spherical models, the bipolar models yield large $[(\text{Co}, \text{Zn})/\text{Fe}]$ and small $[(\text{Cr}, \text{Mn})/\text{Fe}]$ for given $[(\text{Mg}, \text{O})/\text{Fe}]$. This is due to the characteristic in hydrodynamics of the bipolar models, i.e., the ejection of higher temperature (and higher entropy) matter along the z -axis and the accretion of lower temperature matter along the r -axis.

If the formation of metal-poor stars was mainly driven by a supernova shock wave, $[\text{Fe}/\text{H}]$ in those stars is approximately determined by the ratio of the ejected mass of Fe to the amount of interstellar hydrogen swept up by the shock wave (Ryan et al. 1996). Then $[\text{Fe}/\text{H}]$ of the newly born metal-poor star is expressed as

$$[\text{Fe}/\text{H}] = \log_{10}(M(\text{Fe})_{\text{SN}}/M(\text{H})_{\text{SW}}) - \log_{10}(X(\text{Fe})/X(\text{H}))_{\odot}. \quad (7)$$

Here $M(\text{Fe})_{\text{SN}}$ is the mass of ejected iron and $M(\text{H})_{\text{SW}}$ is the mass of interstellar hydrogen swept up by the shock wave.

According to Shigeyama & Tsujimoto (1998), $M(\text{H})_{\text{SW}}$ can be estimated as

$$M(\text{H})_{\text{SW}} = 5.1 \times 10^4 M_{\odot} (E_{51})^{0.97} n_1^{-0.062} (C_{10})^{-9/7}, \quad (8)$$

where n_1 denotes the number density of hydrogen in circumstellar/interstellar medium (cm^{-3}) and C_{10} is the sound speed in units of 10 km s^{-1} . The values of $[\text{Fe}/\text{H}]$ estimated by these formulae are listed in Table 9 along with the values of $[\text{X}/\text{Fe}]$.

Assume that the spherical models 40SL and 25S with $M(^{56}\text{Ni}) = 0.1 M_{\odot}$ represent normal supernovae, then the bipolar models 40A-C and 25A can well account for the abundance trends observed in extremely metal-poor stars. These models have larger $[(\text{Zn}, \text{Co})/\text{Fe}]$, smaller $[(\text{Mn}, \text{Cr})/\text{Fe}]$, and smaller $[\text{Fe}/\text{H}]$ than those in 40SL and 25S. In addition, $[\text{Mg}/\text{Fe}]$ and $[\text{O}/\text{Fe}]$ are large enough to be consistent with observed ones. The smaller $[\text{Fe}/\text{H}]$ is

due to larger explosion energies and thus large $M(\text{H})_{\text{sw}}$ (Equation (8)) in these models. We emphasize that these good coincidence can not be achieved by simply varying a mass cut in spherical models. An example is the model 40SH with large $M(^{56}\text{Ni})$, which has the problems of too small $[(\text{Mg}, \text{O})/\text{Fe}]$ as already noted, as well as too large $[\text{Fe}/\text{H}]$. Figure 18 demonstrates that the models 40A and 25A are in good agreement with the abundances in extremely metal-poor stars, well-reproducing the overabundance of $[(\text{Zn}, \text{Co})/\text{Fe}]$ as well as the trends seen in metal-poor stars.

4.2. Intermediate Mass Elements

Enhancement of $[(\text{Sc}, \text{Ti})/\text{Fe}]$ is also characteristic of the bipolar models. These ratios are sensitive to the asphericity in the explosion. For larger asphericity, these ratios are larger, which is especially evident for $[\text{Sc}/\text{Fe}]$. We note that the production of Sc is very sensitive to how the detailed jet phenomenology can be resolved in the numerical calculation (see Appendix). The enhancement of $[\text{Sc}/\text{Fe}]$ is probably the case, though the detailed value of $[\text{Sc}/\text{Fe}]$ is to be examined by higher resolution simulations.

The enhancement of $[\text{Sc}/\text{Fe}]$ was not clearly shown in the previous studies on bipolar explosions (Nagataki 2000; Maeda et al. 2002). For example, Maeda et al. (2002) yields $[\text{Si}/\text{Fe}] = -0.74$. This is not surprising, because these previous works only addressed the limited case, i.e., prompt explosions.

$[(\text{Sc}, \text{Ti})/\text{Fe}]$ have been problematic in the previous supernova yields based on conventional spherical models. $[(\text{Sc}, \text{Ti})/\text{Fe}] \sim 0 - 0.5$ are observed in the very metal-poor stars, while those predicted by the models were less than the solar values (even much less for $[\text{Sc}/\text{Fe}]$). The present bipolar models predict $[(\text{Sc}, \text{Ti})/\text{Fe}] \gtrsim 0$ (for highly aspherical explosions), thus being in good agreement with observations (though these values, especially of Sc, have to be examined by higher resolution calculations. See Appendix).

4.3. Carbon-rich Metal-Poor Stars

Model 40D produces very small amount of $^{56}\text{Ni} \sim 10^{-7} M_{\odot}$, while the explosion is very energetic with $E_{51} \sim 10$. Such Fe-poor explosions might have caused the formation of a certain class of carbon-rich metal-poor stars, e.g., CS22949-037 (Norris et al. 2001; Aoki et al. 2002; Depagne et al. 2002) as postulated by Umeda & Nomoto (2003).

Model 40D ejects very little amount of explosive burning products, while a large amount of C, O, and Mg are ejected. This results in the enhancement of $[(\text{C}, \text{O}, \text{Mg})/\text{Fe}]$ as shown in Figure 14 and Table 9. The enhancement of $[(\text{Si}, \text{S})/\text{Fe}]$ is smaller because of accretion of a large fraction of Si and S. Heavier elements, such as iron-peak elements, relative to the solar values are not enhanced. These features are consistent with the abundance feature of CS22949-037. It would also be possible for larger amount of Mg to accrete to become $[\text{Mg}/\text{Fe}] \sim 0$ as postulated in Umeda & Nomoto (2003) to reproduce the observed feature of the most Fe-poor star HE0107-5249 (Cristlieb et al. 2002).

The bipolar models predict other characteristic abundance ratios, which can be tested with observations. For

example, the bipolar models predict smaller $[\text{S}/\text{Si}]$ and $[\text{O}/\text{C}]$ ratios for Fe-poor stars as discussed in section 3.3.

Also, in the context of the bipolar explosion, Fe-poor explosions are accompanied with the formation of very massive central remnants, i.e., $M_{\text{REM}} \gtrsim 10 M_{\odot}$. Model 40D results from large $M_{\text{REM}0}$, the mass of the remnant at the initiation of the jets. Though we treated $M_{\text{REM}0}$ as a parameter, we expect $M_{\text{REM}0}$ is related to the angular momentum in the presupernova star. If the Fe core is rapidly rotating before the explosion, $M_{\text{REM}0}$ would be small. On the other hand, if the core rotates relatively slowly, the core would not generate the jets immediately. In this case, continuous accretion would spin up the core, thus the core would be large at the formation of the jets, resulting in larger $M_{\text{REM}0}$.

5. CONCLUSIONS & DISCUSSION

In this paper, we have shown the hydrodynamical and nucleosynthetic features of bipolar supernova/hypernova explosions. In our 2D hydrodynamical models, the properties of jets (such as \dot{M}_{jet} and \dot{E}_{jet}) are determined by the mass accretion rate $\dot{M}_{\text{accretion}}$ as described in equation (1), while the interaction between the jets and the stellar material affects $\dot{M}_{\text{accretion}}$ and thus the properties of the jets. In our models, therefore, the explosion and the fallback are self-regulated.

Two possible sites have been suggested to be responsible for nucleosynthesis in jet-driven supernova/hypernova explosions: stellar materials heated by the jets and jets (winds) themselves from the central region. Which is more prominent will be determined by how much fraction of accreting materials is ejected from the accretion disk rather than is accreted onto the central remnant. In the present study, we have only addressed the case where a small amount of the accreting gas is ejected in the jets, i.e., fast and light jets. The other possibility, i.e., slow and massive jets (disk wind), is also interesting, though we postpone the detailed study to future works as it should require a different approach (both in physically and numerically) from the present study (see sections 1 & 2).

With the caveat mentioned above, our important and interesting findings are summarized as follows.

- (1) **Explosion Energies:** In our models, the resultant explosion energy ranges from $E_{51} \sim 0.5$ to $\gtrsim 30$, thus covering the observed hypernovae whose kinetic energies are estimated to be $E_{51} \sim 6 - 10$ (SN 2002ap: Mazzali et al. 2002), $E_{51} \sim 10 - 20$ (SN 1997ef: Iwamoto et al. 2000; Mazzali et al. 2000), and $E_{51} \gtrsim 30$ (SN 1998bw; Iwamoto et al. 1998). Reasonable parameters of the jets' properties (e.g., $\alpha = 0.01$) yield explosions with $E_{51} \sim 10$, which implies that these are promising models for hypernovae. Moreover, we have found that a more massive star produces a more energetic explosion, which reproduces the observed trend in the 'hypernova branch' (Figure 1; see also Nomoto et al. 2003).
- (2) **Remnant's Mass:** The mass of the central remnant shows a large variation, $M_{\text{REM}} \sim 2 - 10 M_{\odot}$, being larger for more massive progenitors. M_{REM} reaches $\gtrsim 5 M_{\odot}$ for the progenitor star with $M_{\text{ZAMS}} = 40 M_{\odot}$. This can be tested with observations of su-

pernova remnants and X-ray binaries, such as X-ray Nova Sco (Israelian et al. 1999). In fact Nova Sco shows the evidence of nucleosynthesis in a hypernova explosion accompanied by the formation of a black hole with $M_{\text{BH}} \sim 5M_{\odot}$ (Podsiadlowski et al. 2002).

- (3) **Density Structure:** The density structures of the ejecta of the bipolar models do not resemble those of conventional spherical models. Though the detailed structure becomes more evident with higher numerical resolutions, the overall slope is rather insensitive to the resolution. The slope depends on the assumed jet properties and probably on time variability of the central source, while the bipolar models in general have much flatter density distributions in the outer layers and a higher density central core than the spherical models. These features agree with the those inferred from modeling spectra and light curves of the observed hypernovae (Branch 2001 and Nakamura et al. 2001a for SN 1998bw; Iwamoto et al. 2000 and Mazzali et al. 2000 for SN 1997ef; Mazzali et al. 2002 and Yoshii et al. 2003 for SN 2002ap; Maeda et al. 2003 for SNe 1998bw, 1997ef, 2002ap).
- (4) **Production of ^{56}Ni :** The amount of synthesized ^{56}Ni , $M(^{56}\text{Ni})$, depends on the time scale of energy injection. For slow energy injection, $M(^{56}\text{Ni})$ is small because of pre-expansion of the ejecta. For $\dot{E}_{51} \lesssim 1 \text{ s}^{-1}$ or $M_{\text{REM0}} \gtrsim 3M_{\odot}$, especially, $M(^{56}\text{Ni}) \lesssim 0.1M_{\odot}$. The present models predict that there is rough anti-correlation between ^{56}Ni and M_{REM} . To explain the large masses of ^{56}Ni in the observed hypernovae ($M(^{56}\text{Ni}) \gtrsim 0.1M_{\odot}$), the explosion mechanism must satisfy one of the following conditions:
- (a) \dot{E}_{51} is as large as $\gtrsim 10 \text{ s}^{-1}$ and $M_{\text{REM0}} \lesssim 3M_{\odot}$, i.e., the compact remnant begins to generate jets before it evolves too much. In this case, the amount of ^{56}Ni produced at the shocked stellar material could be as large as $\sim 0.5M_{\odot}$ as observed in SN1998bw (Iwamoto et al. 1998).
 - (b) The jets (outflow from the central region) are more massive and have smaller velocities than those in the present models. Such jets could contain abundant ^{56}Ni in the jet material itself.

In both cases we expect that the distribution of ^{56}Ni is highly aspherical and elongated along the z -axis. Such configuration can account for the unusual feature in late time spectra of SN1998bw (Maeda et al. 2002).

- (5) **Distribution of isotopes:** The distribution of various isotopes in the bipolar models is completely different from conventional spherical models. Nucleosynthetic products are distributed as follows in the order of decreasing velocities (radii):
- (a) products of strong α -rich freezeout (e.g., ^{64}Zn , ^{59}Co , ^{44}Ca) at the highest velocity,
 - (b) products of complete silicon burning (e.g., ^{56}Fe),
 - (c) products of incomplete silicon burning (e.g., ^{55}Mn , ^{52}Cr , ^{40}Ca , ^{32}S , ^{28}S), and

- (d) products of hydrostatic burning (e.g., ^{32}S , ^{28}Si , ^{16}O , ^{12}C , ^4He) at the lowest velocity.

(6) **Abundance patterns:**

- (a) α -rich freezeout and radioactive isotopes: The ratio between α -rich freezeout products and $^{56}\text{Ni}(\text{Fe})$ is enhanced for more aspherical explosions. In particular, $^{44}\text{Ti}/^{56}\text{Ni}$ is enhanced significantly.
- (b) Iron-peak elements: The bipolar models provide unique yields for iron-peak elements, where $[\text{Zn}/\text{Fe}]$ and $[\text{Co}/\text{Fe}]$ are enhanced while $[\text{Cr}/\text{Fe}]$ and $[\text{Mn}/\text{Fe}]$ are suppressed for a given $[(\text{Mg}, \text{O})/\text{Fe}]$. The reason is that the bipolar explosions blow up the material from the innermost region which undergoes strong α -rich freezeout.
- (c) ^{45}Sc : Another important feature is the production of ^{45}Sc . It has been difficult to produce ^{45}Sc in spherical models, even for very large explosion energies. Spherical models always predict $[\text{Sc}/\text{Fe}] < -1$ because of too high densities (too low entropies) in the regions where α -rich freezeout takes place to produce a large amount of ^{45}Sc . The bipolar models, on the other hand, provide $[\text{Sc}/\text{Fe}] \sim 0$, because α -rich freezeout proceeds at lower densities along the z -axis than in spherical models. Inversely, ^{45}Sc could be an indicator of the degree of asphericity in supernovae/hypernovae. At the same time, we have found that the production of Sc is very sensitive to how the detailed jet phenomenology can be resolved. Therefore, future higher resolution studies are needed to confirm this result.
- (d) Intermediate mass elements: The bipolar models have different characteristics in the ratios among S, Si, Mg, O, C as compared to spherical models. In contrast to spherical models, which predict that these ratio are insensitive to the explosion process, the bipolar models result in large variations in these ratios. The accretion decreases the amount of those elements in a different way (e.g., S is more easily accreted onto the central remnant than Si), thus these ratios depends on the amount of the matter accreted onto the center. Large M_{REM} results in the reduction of heavier elements (e.g., larger M_{REM} leads to smaller $[\text{S}/\text{Si}]$, which might explain the low S/Si in M87 (Matsushita et al. 2003)).

(7) **Extremely metal-poor stars:**

- (a) Trends in iron-peak elements: The nucleosynthetic features of the bipolar models (described in (6b) above) are compatible with the abundance patterns and trends in extremely metal-poor stars. This is the result of the combined effects of the jets and the fallback. In spherical explosion models, 'mixing and fallback' provides a good agreement between the ejecta yields and the observed abundances (Umeda

& Nomoto 2003). The bipolar models provide naturally (without fine tuning) almost the same effect as ‘mixing and fallback’ by ejecting preferentially higher entropy matter. Moreover, it is possible that the jets induce a global mixing, through share instability and so on.

- (b) Fe-poor explosions and black hole formation: Some bipolar models also explain the existence of Fe-poor explosions with very little amount of Fe. Such explosion would be responsible for the formation of the carbon-rich metal-poor stars including the most Fe-poor star. The Fe-deficient explosion results from large $M_{\text{REM}0}$, which may be interpreted as the small angular momentum in the pre-explosion core.

We have shown that the bipolar models have potential to explain a wide range of observations. We conclude that (1) hypernovae explosions are driven by bipolar jets, and (2) their contribution on the early Galactic chemical evolution may be significant.

We would like to thank Hideyuki Umeda for useful discussion. The computation was partly carried out on Fujitsu VPP-700E at the Institute of Physical and Chemical Research (RIKEN). This work has been supported in part by the grant-in-Aid for COE Scientific Research (14047206, 14540223) of the Ministry of Education, Science, Culture, Sports, and Technology in Japan.

A. SENSITIVITY TO THE NUMERICAL RESOLUTION

In this section, we show what extent the results depend on the numerical grid resolution. We have run model 40A with the numerical grids 200×60 (higher resolution), 100×30 (standard run), and 70×21 (lower resolution) to see if there are significant differences.

Figure 19 shows time evolution of M_{REM} for different numerical resolutions. The evolution of M_{REM} is determined by the interaction between the jets and stellar materials, thus is a good indicator for a convergence test. Also, the final M_{REM} is of essential importance to the resultant isotopic composition in the ejected materials, because it determines which regions are finally ejected.

Except for the lowest resolution (70×21), the curves are almost identical. We, therefore, are confident that the numerical resolution of 100×30 used throughout the paper is sufficient to catch the overall structure of the interaction. In the lowest resolution, it is most likely that the bow shock expands sideways incorrectly faster than in the higher resolutions, making the accretion rate smaller.

Another test is to see the detailed structure of the ejecta. Figure 20 shows the density structures along the z - and r -axis for different resolutions. As implied by the first test (M_{REM}), the overall structure from the lowest to the highest velocities is very similar to one another. The curves of the higher resolution runs, especially, match with each other almost identically, except at the highest velocities ($\gtrsim 2.5 \times 10^9 \text{ cm s}^{-1}$) along the z -axis.

With higher numerical resolution appears richer jet phenomenology (Aloy et al. 2000; Zhang, Woosley, & Mac-

Fadyen 2003), making the deviation of the detailed structure at the highest velocities along the z -axis among the different numerical resolutions. We do not see the numerical convergence in this sense, thus need a higher resolution (more than 200×60) to resolve the exact jet phenomenology. We postpone it to future works. We note, however, that the averaged behavior (e.g., the averaged slope at $> 10^8 \text{ cm s}^{-1}$) is rather insensitive to the detailed density structure, as low resolutions just smear the details.

The final and the most important test is to see the effects of the numerical resolution on the isotopic composition of the ejected materials. Figure 21 compares the isotopic yield of model 40A with different resolutions. The isotopic compositions, especially for major species, are strikingly similar to one another. This is because the main feature of the jet induced explosion is the ejection of higher entropy materials associated with the jets and the accretion of lower entropy materials initially at outer envelopes, and the process is appropriately resolved with the resolution of 100×30 (Fig. 19).

A few isotopes, however, show quantitative difference for different resolutions. They are ^{44}Ca , ^{48}Ti (enhanced with higher resolution), and ^{45}Sc (suppressed). The difference of $(^{44}\text{Ca}, ^{48}\text{Ti})/^{56}\text{Fe}$ between different resolutions is still not large and the results with the resolution of 100×30 are almost unchanged, while $^{45}\text{Sc}/^{56}\text{Fe}$ shows the difference by a factor of 2 – 3.

The difference most likely comes from the formation of richer jet phenomenology with higher resolution (Fig. 20). Because these isotopes, especially ^{45}Sc , are minor isotopes and produced by α -rich freezeout, production of these isotopes is sensitive to the detailed structure (e.g., recollimation shocks; see Aloy et al. 2000 and Zhang et al. 2003) of the interaction between the jets and stellar materials.

In sum, we evaluate sensitivity of the results to numerical resolution as follows.

- (1) The overall structure of the hydrodynamic interaction can be resolved with the resolution of 100×30 used throughout the paper. It guarantees the results on the global quantities in the paper, e.g., M_{REM} , E_{total} , and $M(^{56}\text{Ni})$. For most isotopes, we see the convergence at the resolution 100×30 .
- (2) To resolve the detailed jet phenomenology, we need higher numerical resolutions. This affects the detailed density structure at the highest velocities along the z -axis, and production of a few isotopes. The isotope which is most sensitive to the resolution is ^{45}Sc . The detailed ejecta structure is of course important, though we note that the averaged behavior does not sensitively depend on the numerical resolution. For model 40A, the density structure above 10^9 cm s^{-1} shows significant flattening compared to spherical model 40SH, and the average slope is similar irrespective of the resolution. For ^{45}Sc , the result of the present study, i.e., the enhancement of $^{45}\text{Sc}/^{56}\text{Fe}$ is probably correct qualitatively, while we need future works with higher resolutions to conform the result quantitatively.

REFERENCES

- Aloy, M.A., Müller, E., Ibáñez, J.M., Martí, J.M., & MacFadyen, A. 2000, *ApJ*, 531, L119
- Aoki, W., Ryan, S.G., Beers, T.C., Ando, H. 2002, *ApJ*, 567, 1166
- Audouze, J., & Silk, J. 1995, *ApJ*, 451, L49
- Aufferheide, M.B., Baron, E., & Thielemann, F.-K. 1991, *ApJ*, 370, 630
- Blake L.A.J. et al. 2001, *Nucl. Phys. A.*, 688, 502
- Blandford, R.D., & Znajek, R.L. 1977, *MNRAS*, 179, 433
- Branch, D. 2001, in 'Supernovae and Gamma Ray Bursts,' eds. Livio, M. et al. (Cambridge: Cambridge University Press), 96
- Brown, G.E., Lee, C.-H., Wijers, R.A.M.J., Lee, H.K., Israelian, G., Bethe, H.A. 2000, *New Astronomy*, 5, 191
- Christlieb, N., et al. 2002, *Nature*, 419, 904
- Depagne, E. et al. 2002, *A&A*, 390, 187
- Fraiburghaus, C., Rembges, J.-F., Rauscher, T., Kolbe, E., Thielemann, F.-K., Kratz, K.-L., Pfeiffer, B., Cowan, J.J. 1999, *ApJ*, 516, 381
- Galama, T.J., et al. 1998, *Nature*, 395, 670
- Germany, L.M., Reiss, D.J., Sadler, E.M., Schmidt, B.P., Stubbs, C.W. 2000, *ApJ*, 533, 320
- Hachisu, I. 1986, *ApJS*, 62, 461
- Hachisu, I., Matsuda, T., Nomoto, K., Shigeyama, T. 1992, *ApJ*, 390, 230
- Hachisu, I., Matsuda, T., Nomoto, K., Shigeyama, T. 1994, *A&AS*, 104, 341
- Hamuy, M. 2003, *ApJ*, 582, 905
- Hatano, K., Branch, D., Nomoto, K., et al. 2001, *BAAS*, 198, 3902
- Hix, W.R., & Thielemann, F.-K. 1996, *ApJ*, 460, 869
- Hix, W.R., & Thielemann, F.-K. 1999, *ApJ*, 511, 862
- Israelian, G., Reboloto, R., Basri, G., et al. 1999, *Nature*, 401, 142
- Iwamoto, K., Nomoto, K., Höflich, P.A., Yamaoka, H., Kumagai, S., Shigeyama, T. 1994, *ApJ*, 437, L115
- Iwamoto, K., et al. 1998, *Nature*, 395, 672
- Iwamoto, K., et al. 2000, *ApJ*, 534, 660
- Janka, H.-Th., Buras, R., Kifonidis, K., Plewa, T., Rampp, M. 2003, in 'From Twilight to Highlight: The Physics of Supernovae', eds. W. Hillebrandt & B. Leibundgut (Berlin: Springer), 40
- Kawabata, K.S., et al. 2002, *ApJ*, 580, L39
- Khokhlov, A.M., Höflich, P.A., Oran, E.S., Wheeler, J.C., Wang, L., Chtchelkanova, A. Yu. 1999, *ApJ*, 524, L107
- Kinugasa, K., Kawakita, H., Ayani, K., Kawabata, T., Yamaoka, H., Deng, J., Mazzali, P.A., Maeda, K., Nomoto, K. 2002, *ApJ*, 577, L97
- Knop, R., Aldering, G., Deustua, S., et al. 1999, *IAU Circ.*, 7128
- LeBlanc, J.M., & Willson, J.R. 1970, *ApJ*, 161, 541
- Leonard, D.C., Filippenko, A.V., Chornock, R., Foley, R.J. 2002, *PASP*, 114, 1333
- MacFadyen, A.I., & Woosley, S.E. 1999, *ApJ*, 524, 262
- MacFadyen, A.I., Woosley, S.E., & Heger, A. 2001, *ApJ*, 550, 410
- MacFadyen, A.I. 2003, in 'From Twilight to Highlight: The Physics of Supernovae', eds. W. Hillebrandt & B. Leibundgut (Berlin: Springer), 97
- McWilliam, A., Preston, G.W., Sneden, C., & Searle, L. 1995, *AJ*, 109, 2757
- Maeda, K., Nakamura, T., Nomoto, K., Mazzali, P.A., Patat, F., Hachisu, I. 2002, *ApJ*, 565, 405
- Maeda, K., Mazzali, P.A., Deng, J., Nomoto, K., Yoshii, Y., Tomita, H., Kobayashi, Y. 2003, *ApJ*, 593, in press
- Matsushita, K., Finoguenov, A., & Böhringer, H. 2003, *A&A*, 401, 443
- Mazzali, P.A., Iwamoto, K., Nomoto, K. 2000, *ApJ*, 545, 407
- Mazzali, P.A., Nomoto, K., Patat, F., Maeda, K. 2001, *ApJ*, 559, 1047
- Mazzali, P.A., et al. 2002, *ApJ*, 572, L61
- Nagataki, S. 2000, *ApJS*, 127, 141
- Nagataki, S., Mizuta, A., Yamada, S., Takabe, H., & Sato, K. 2003, *ApJ*, in press
- Nakamura, T., Mazzali, P.A., Nomoto, K., Iwamoto, K. 2001a, *ApJ*, 550, 991
- Nakamura, T., Umeda, H., Iwamoto, K., Nomoto, K., Hashimoto, M., Hix, W.R., Thielemann, F.-K. 2001b, *ApJ*, 555, 880
- Narayan, R., Piran, T., & Kumar, P. 2001, *ApJ*, 557, 949
- Nomoto, K., & Hashimoto, M. 1988, *Phys. Rep.*, 256, 173
- Nomoto, K. et al. 2001, in 'Supernovae and Gamma Ray Bursts,' eds. M. Livio, et al. (Cambridge: Cambridge University Press), 144
- Nomoto, K., Maeda, K., Umeda, H., Ohkubo, T., Deng, J., Mazzali, P.A. 2003, in 'A massive Star Odyssey, from Main Sequence to Supernova,' eds. K.A. Van der Hucht, A. Herrero, & C. Esteban (San Francisco: ASP), 395 (astro-ph/0209064)
- Norris, J.E., Ryan, S.G., & Kumar, T.C. 2001, *ApJ*, 561, 1034
- Podsiadlowski, Ph., Nomoto, K., Maeda, K., Nakamura, T., Mazzali, P., Schmidt, B. 2002, *ApJ*, 567, 491
- Popham, R., Woosley, S.E., & Fryer, C.L. 1999, *ApJ*, 518, 356
- Primas, F., Reimers, D., Wisotzki, L., Reetz, J., Gehren, T., & Beers, T.C. 2000, in *The First Stars*, ed. A. Weiss, et al. (Springer), 51
- Pruet, J., Woosley, S.E., & Hoffman, R.D. 2003, *ApJ*, 586, 1254
- Rigon, L. et al. 2003, *MNRAS*, 340, 191
- Ryan, S.G., Norris, J.E. & Beers, T.C. 1996, *ApJ*, 471, 254
- Shigeyama, T., & Nomoto, K. 1990, *ApJ*, 360, 242
- Shigeyama, T., et al. 1994 *ApJ*, 420, 341
- Shigeyama, T., & Tsujimoto, T. 1998, *ApJ*, 507, L135
- Thielemann, F.-K., Nomoto, K., Hashimoto, M. 1996, *ApJ*, 460, 408
- Thomas, R.C., Kasen, D., Branch, D., & Baron, E. 2002, *ApJ*, 567, 1037
- Turatto, M., et al., 1998, *ApJ*, 498, L129
- Turatto, M., Suzuki, T., Mazzali, P.A., Benetti, S., Cappellaro, E., Danziger, I.J., Nomoto, K., Nakamura, T., Young, T.R., Patat, F. 2000, *ApJ*, 534, L57
- Umeda, H., & Nomoto, K. 2002, *ApJ*, 565, 385
- Umeda, H., & Nomoto, K. 2003, *Nature*, 422, 871
- Wang, L., Howell, D.A., Hoefflich, P., Wheeler, J.C. 2001, *ApJ*, 550, 1030
- Wang, L., et al., 2002, *ApJ*, 579, 671
- Wang, L., Baade, D., Höflich, P., Wheeler, J.C. 2003, *ApJ*, 592, 457
- Wheeler, J.C., Yi, I., Höflich, P., Wang, L. 2000, *ApJ*, 537, 810
- Woosley, S.E. 1993, *ApJ*, 405, 273
- Woosley, S.E., & Weaver, T.A. 1995, *ApJS*, 101, 181
- Woosley, S.E., Eastman, E.G., Schmidt, B.P. 1999, *ApJ*, 516, 788
- Yamada, S., & Sato, K. 1994, *ApJ*, 434, 268
- Yoshii, Y., et al. 2003, *ApJ*, 592, 467
- Zampieri, L., Pastorello, A., Turatto, M., et al. 2003, *MNRAS*, 338, 711
- Zhang, W., Woosley, S.E., MacFadyen, A. 2003, *ApJ*, 586, 356

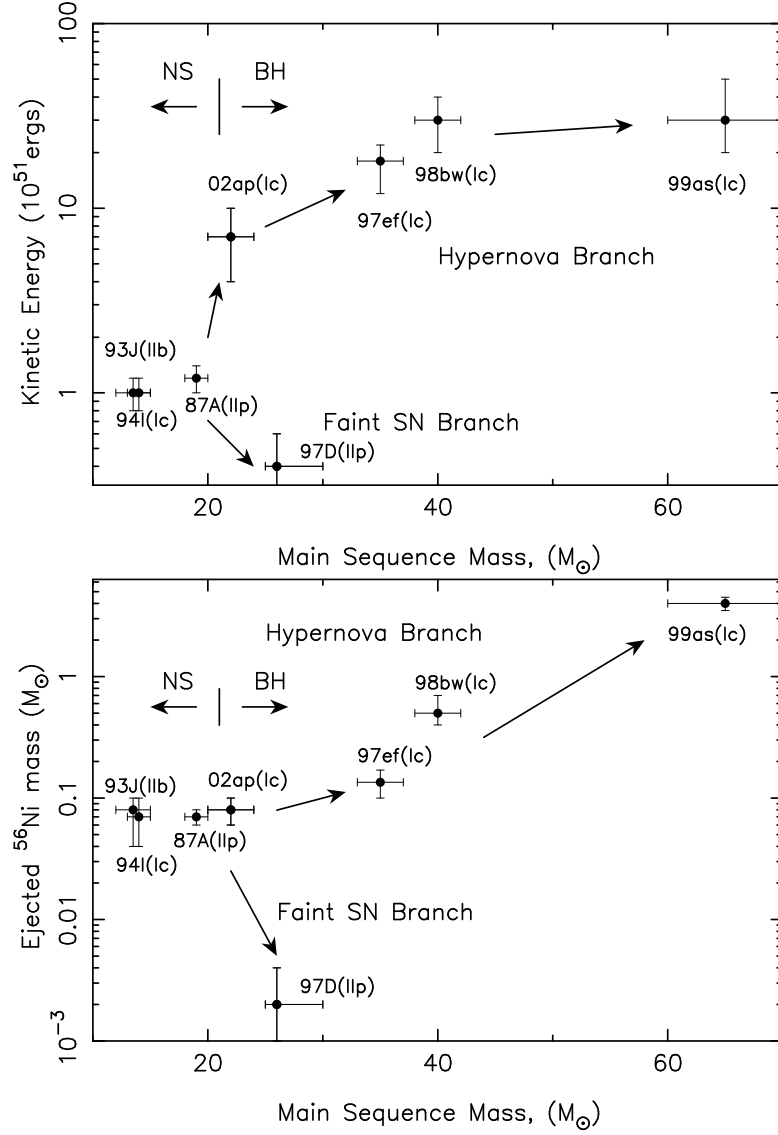


FIG. 1.— (a) Explosion Energies and (b) ejected ^{56}Ni masses against main-sequence mass of the progenitors for core-collapse supernovae/hypernovae, as estimated for SN II 1987A (Shigeyama & Nomoto 1990); SN IIb 1993J (Shigeyama et al. 1994); SN Ic 1994I (Iwamoto et al. 1994); SN II 1997D (Turatto et al. 1998); SN Ic 1997ef (Mazzali et al. 2000); SN Ic 1998bw (Iwamoto et al. 1998); SN Ic 1999as (Hatano et al. 2001); SN Ic 2002ap (Mazzali et al. 2002).

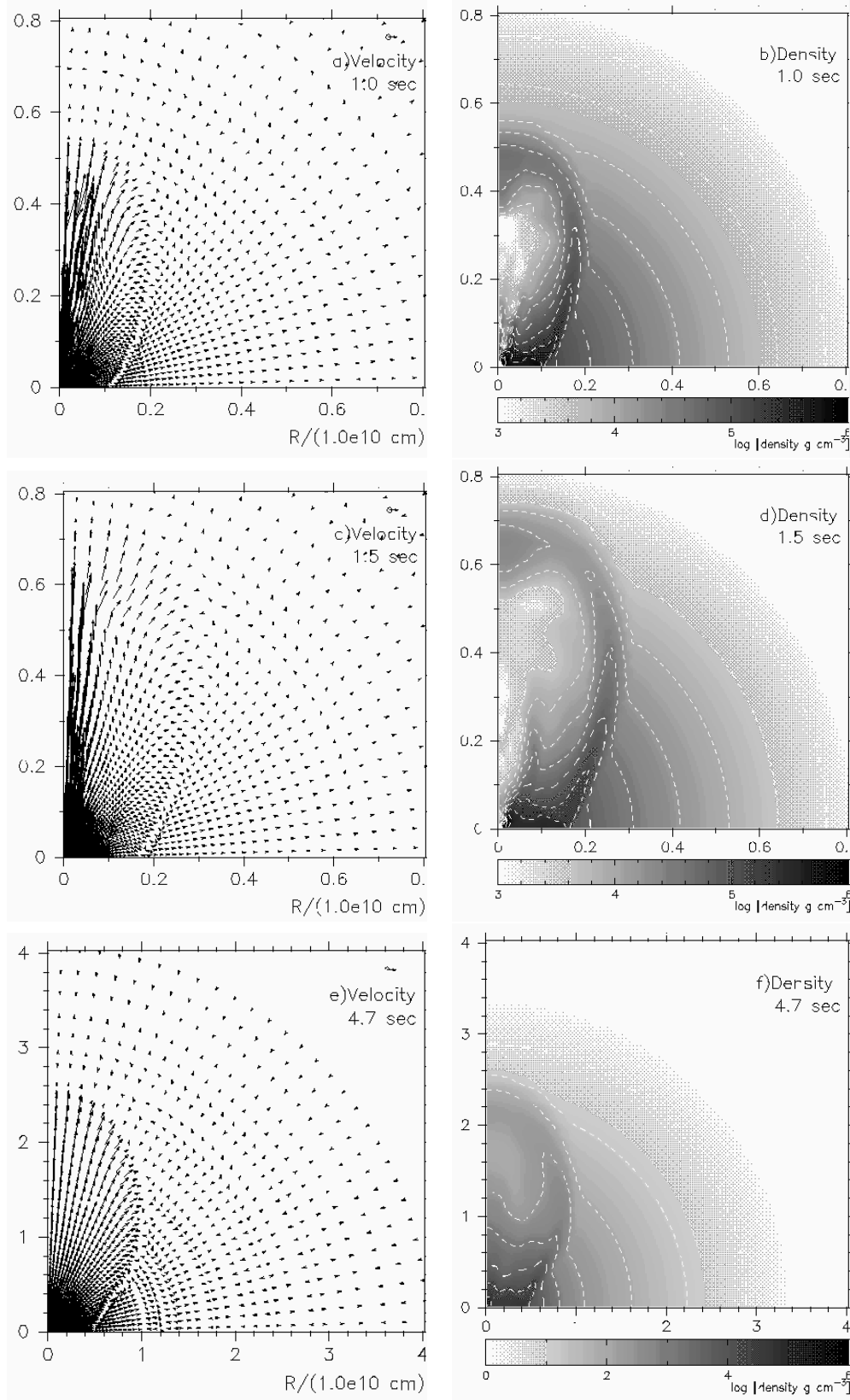


FIG. 2.— (a,c,e) Velocity and (b,d,f) density distributions of model 40A, at 1.0s (a,b), 1.5s (c,d), and 4.7s (e,f) after the initiation of the jets. (a,c,e) The arrows with a circle on its base shown on the upper right of each figure represent $2 \times 10^9 \text{ cm s}^{-1}$. (b,d,e) The interval of contour is $(\text{max-min})/10$ in log scale.

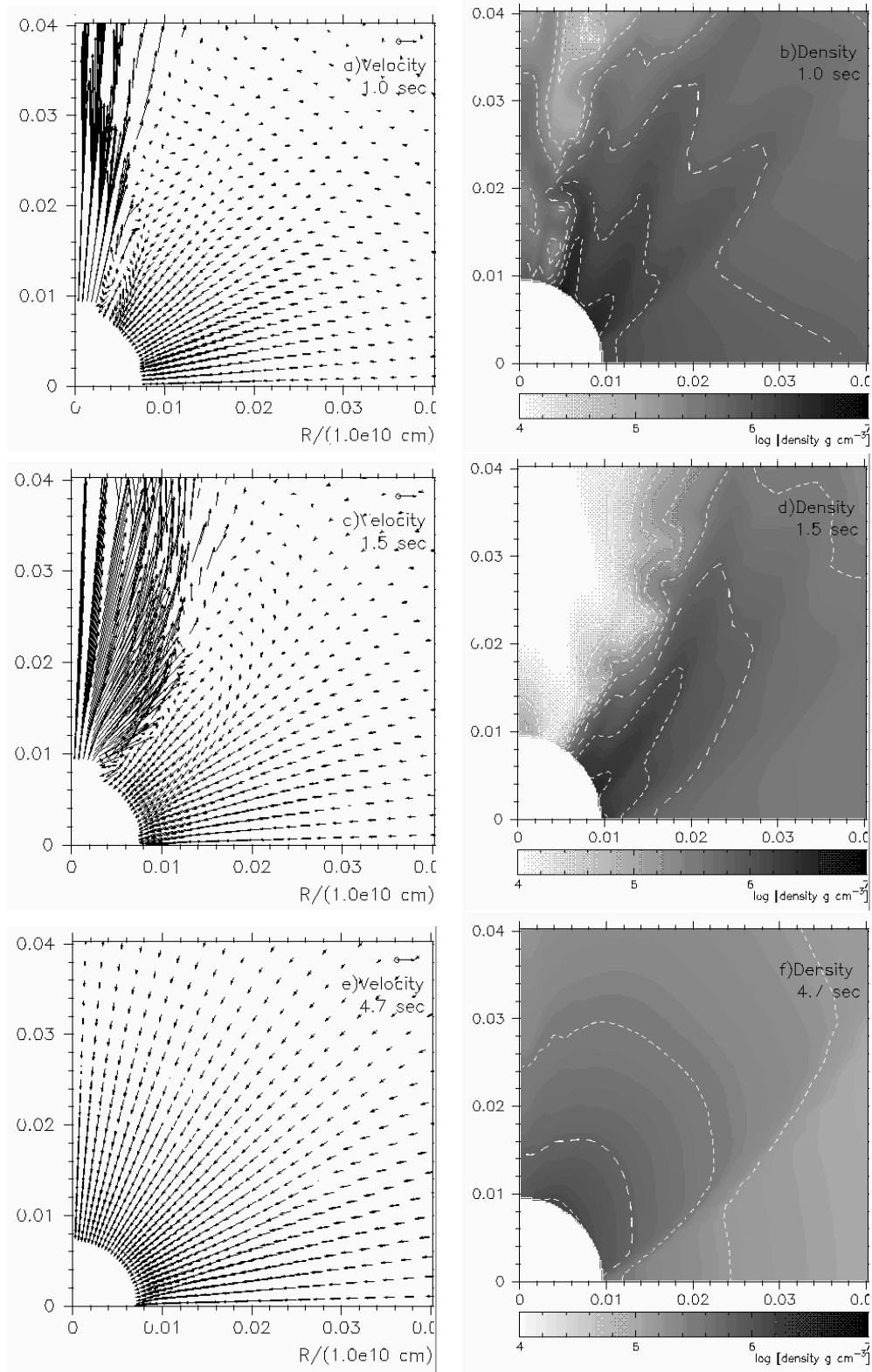


FIG. 3.— The same as Figure 2, but on an expanded scale.

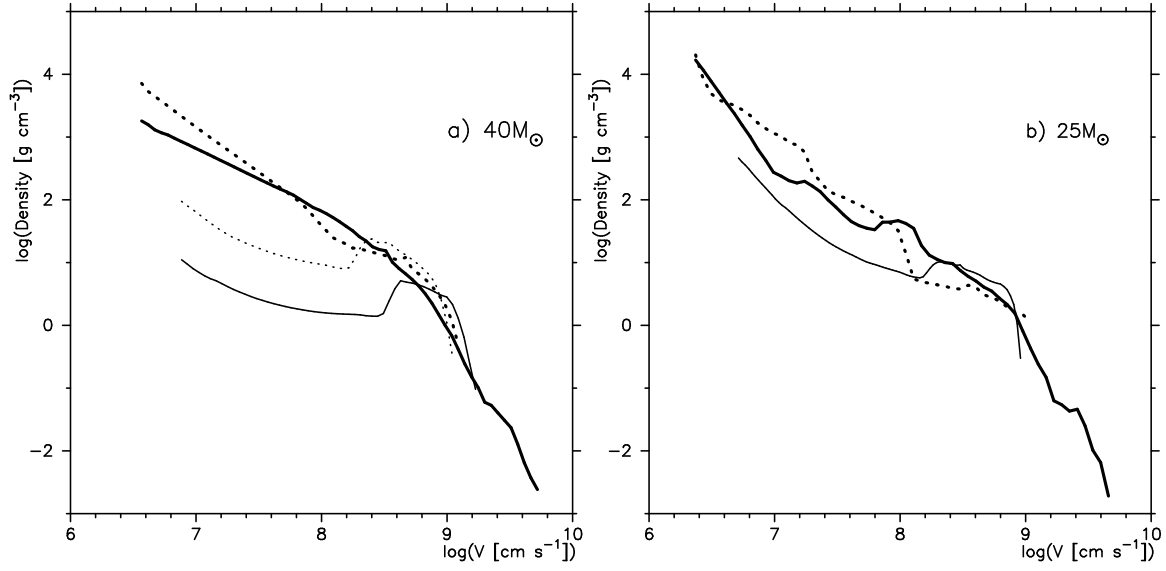


FIG. 4.— Density structure at 100 sec. (a) Along the z -axis of 40A (thick-solid) and the r -axis of 40A (thick-dotted), 40SH (thin-solid), and 40SL (thin-dotted). (b) Along the z -axis of 25A (thick-solid) and the r -axis of 25A (thick-dotted), and 25S (thin-solid).

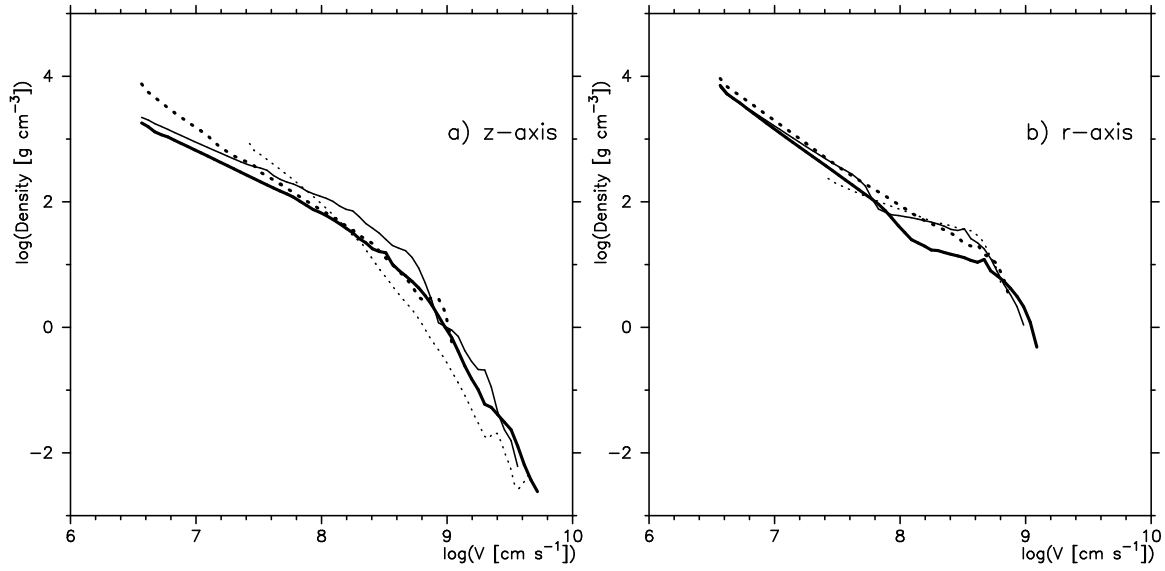


FIG. 5.— Density structure at 100 sec for different jet properties. (a) Along the z -axis of 40A (thick-solid), of 40B (thick-dotted), of 40C (thin-solid), and of 40D (thin-dotted). (b) Along the r -axis of 40A (thick-solid), of 40B (thick-dotted), of 40C (thin-solid), and of 40D (thin-dotted).

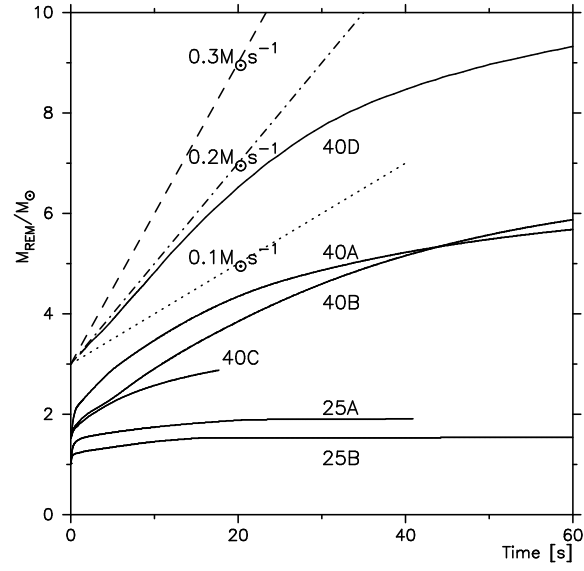


FIG. 6.— Growth of the mass of the central remnant (M_{REM}). The three straight lines correspond to constant accretion rates.

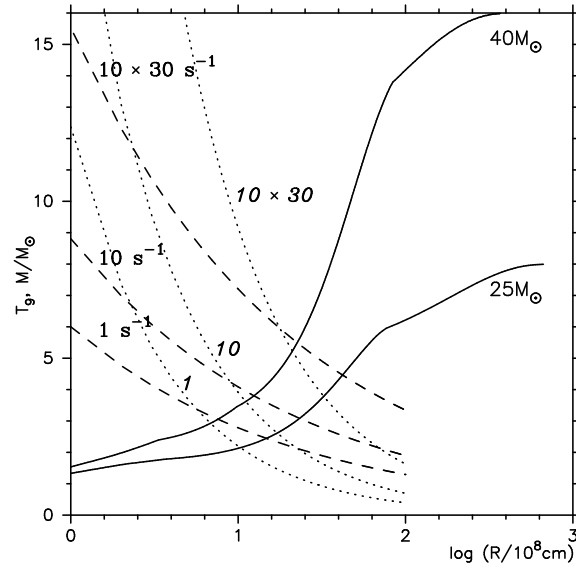


FIG. 7.— The post-shock temperature (T_9) as a function of radius predicted by equation (4), for $t < t_f$ (dashed) and $t \geq t_f$ (dotted). Also shown are the enclosed masses of the progenitor stars with main-sequence masses $M_{\text{ZAMS}} = 40M_\odot$ and $25M_\odot$ (solid lines: Nomoto & Hashimoto 1988).

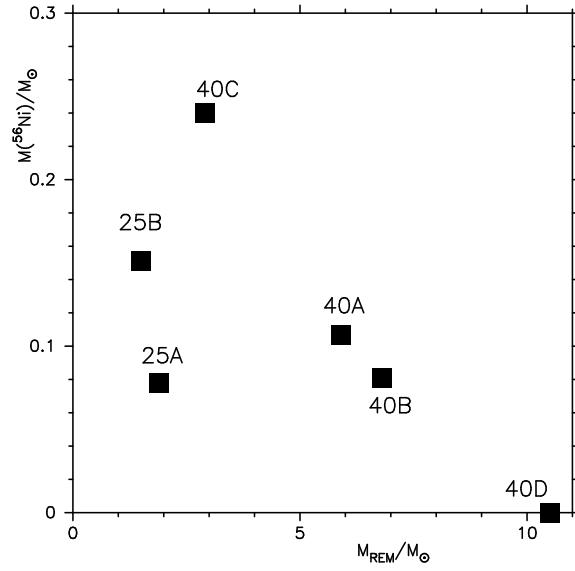


FIG. 8.— The mass of ejected ^{56}Ni as a function of the mass of the central remnant.

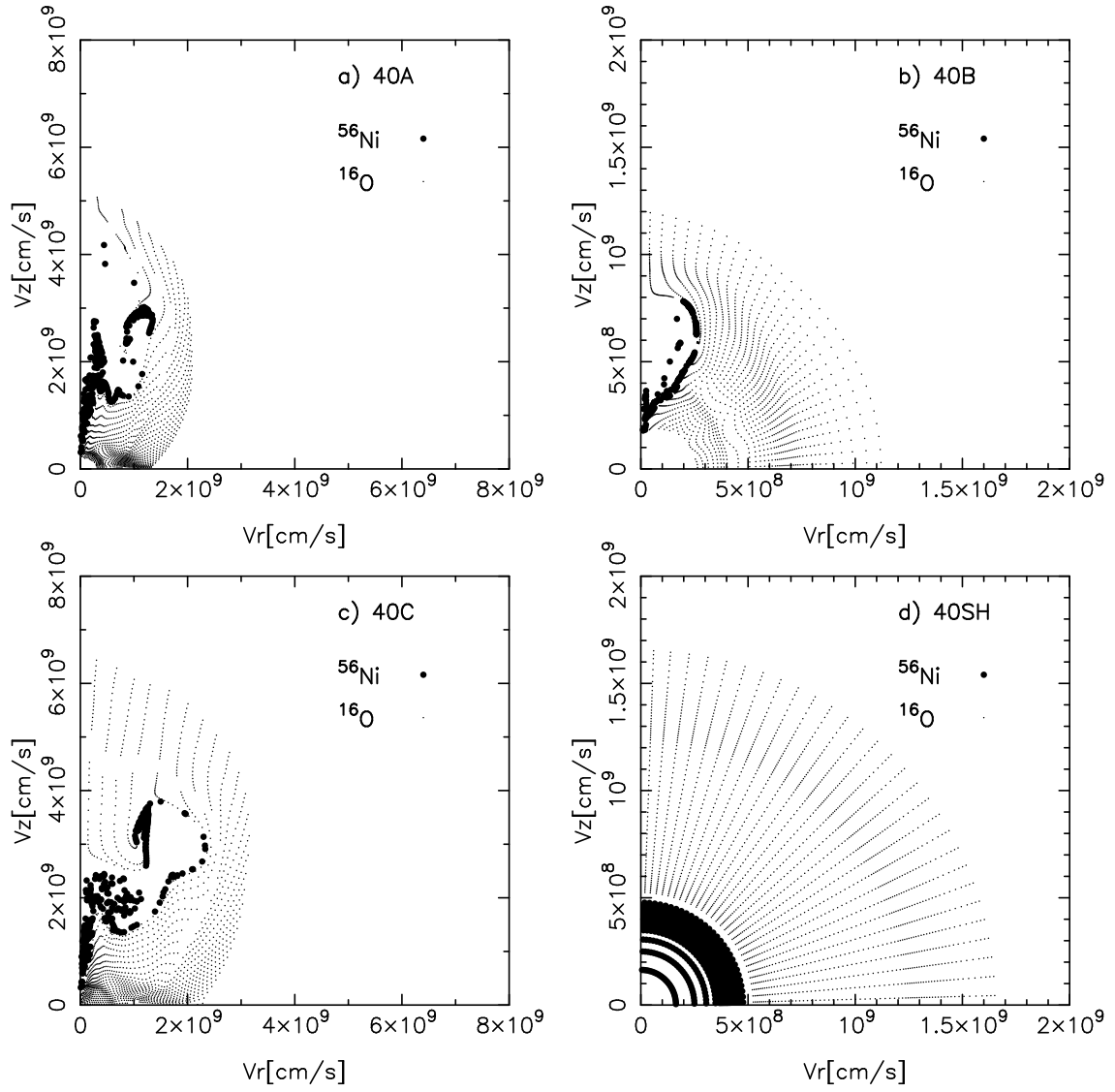


FIG. 9.— Distributions of ^{56}Ni and ^{16}O in the velocity space for (a) model 40A, (b) 40B, (c) 40C, and (d) 40SH. The filled circles and dots, respectively, show the mass elements in which the mass fraction of ^{56}Ni and ^{16}O exceeds 0.08.

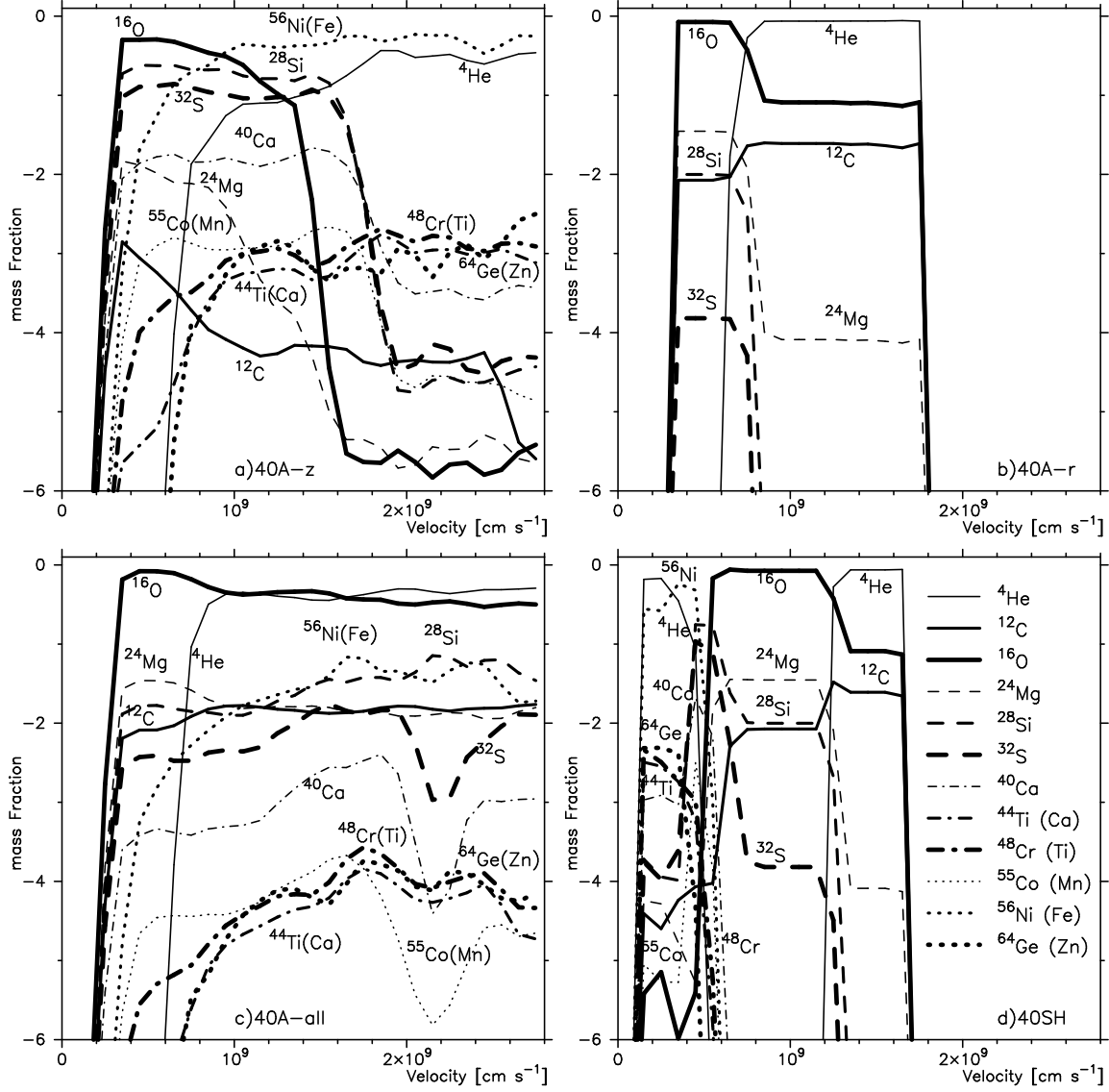


FIG. 10.— Mass fractions of selected isotopes in the velocity space for (a) model 40A along the z -axis (averaged over $0 - 15^\circ$), (b) 40A along the r -axis (averaged over $75 - 90^\circ$), (c) 40A averaged over all directions, and (d) a spherical model 40SH.

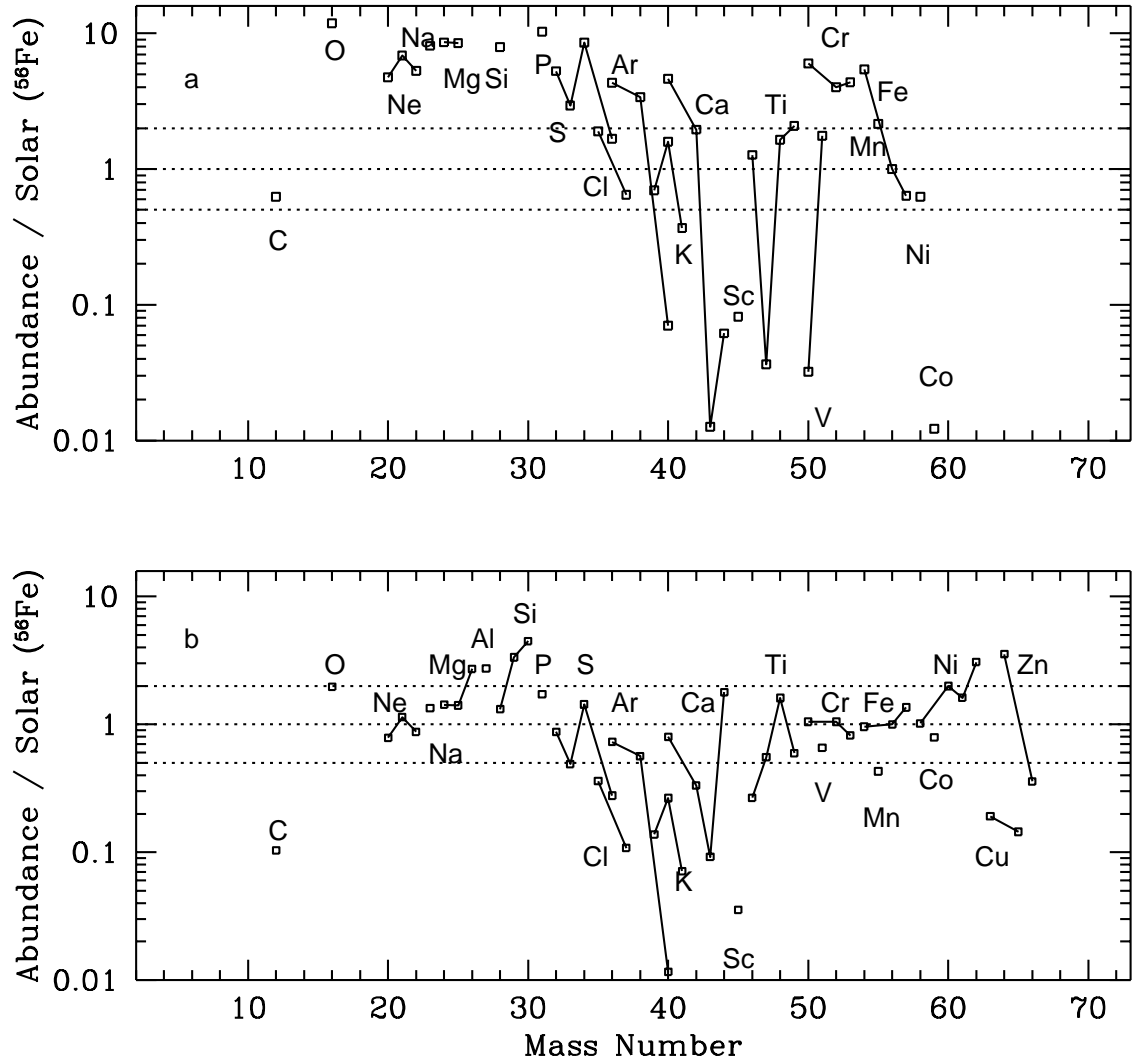


FIG. 11.— Isotopic yields of model the spherical model 40SH for different mass cuts M_{cut} . Larger and smaller M_{cut} lead to (a) $M(^{56}\text{Ni}) = 0.1 M_{\odot}$ and (b) $0.54 M_{\odot}$, respectively.

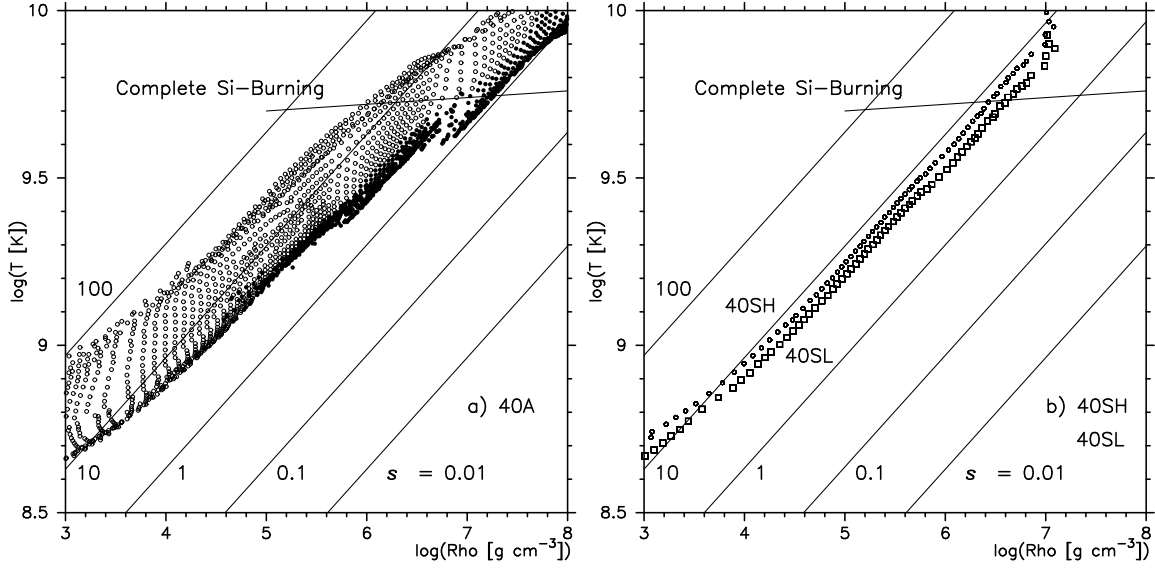


FIG. 12.— Peak temperatures of individual mass elements plotted against densities at the temperature maximum, for (a) model 40A and (b) the spherical models 40SH and 40SL. (a) The open circles and the filled circles denote the mass elements which are finally ejected and accreted, respectively. (b) The open circles and the squares denotes the mass elements for 40SH ($E_{51} = 10$) and 40SL ($E_{51} = 1$), respectively. Entropies, $s \equiv S_{\gamma}/(k_B/m_u) = 4aT^3/3\rho/(k_B/m_u) \sim 0.12T_9^3/\rho_6$, are shown (solid lines). Here k_B and m_u are Boltzmann constant and atomic unit mass, respectively.

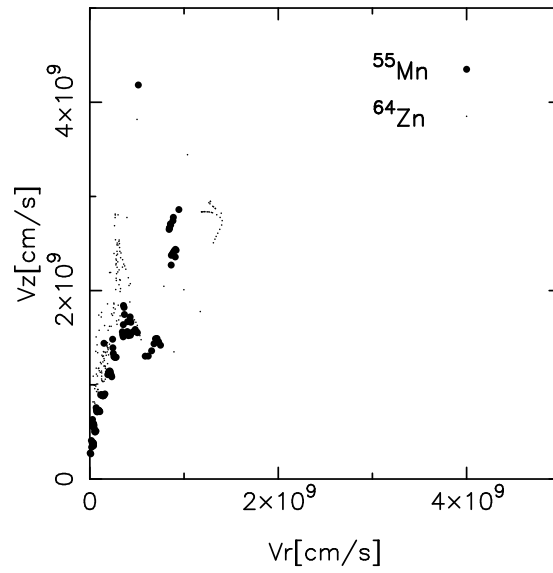


FIG. 13.— Distribution of ^{55}Mn and ^{64}Zn in the velocity space for model 40A. The filled circles and dots, respectively, show the mass elements in which the mass fraction of ^{55}Mn and ^{64}Zn exceeds 10^{-4} .

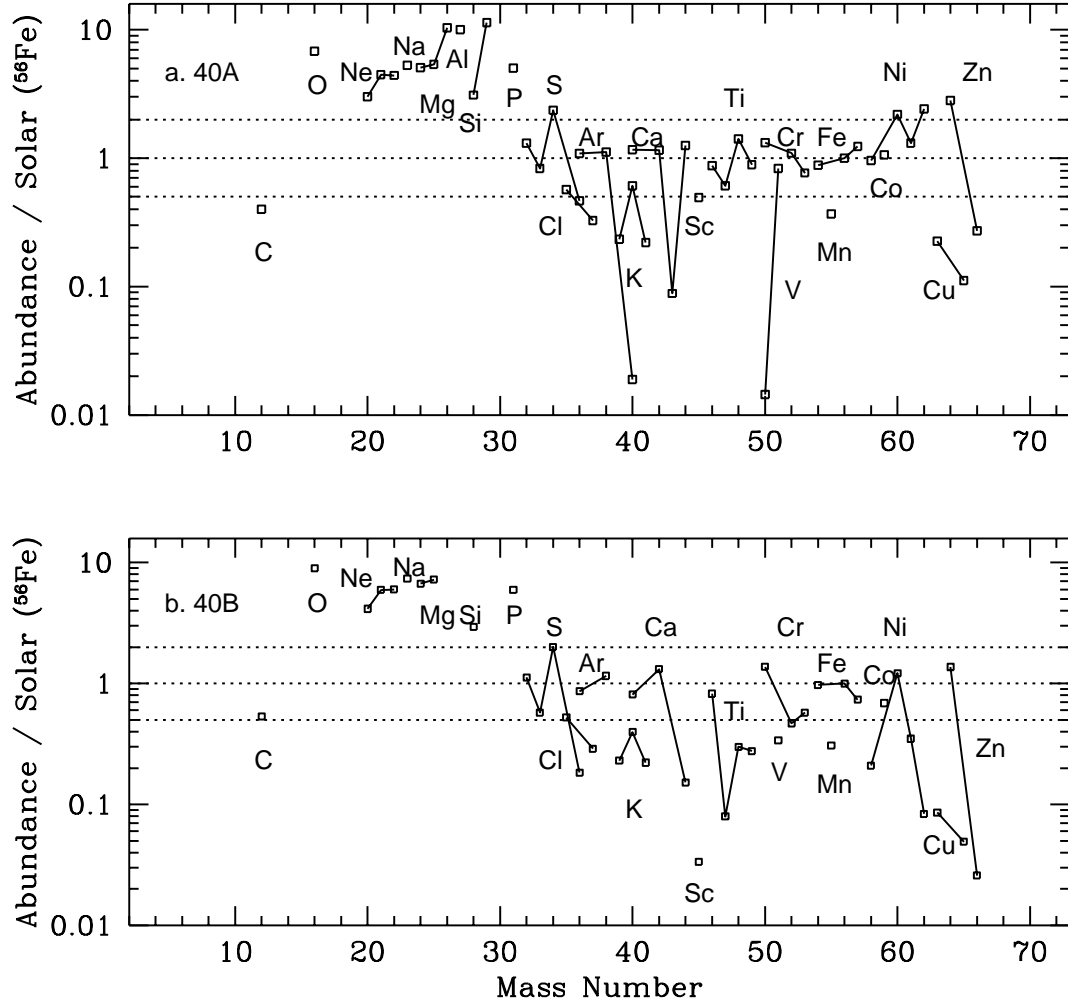
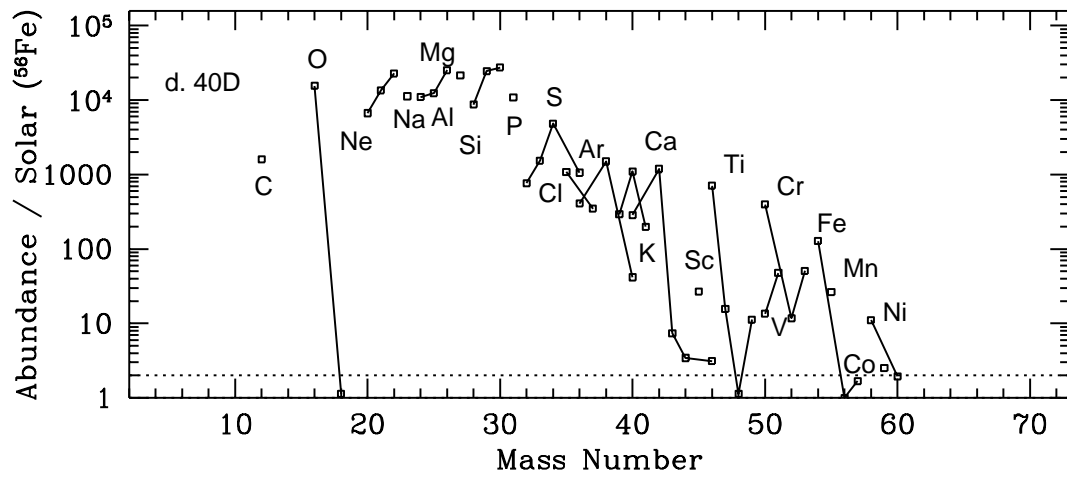
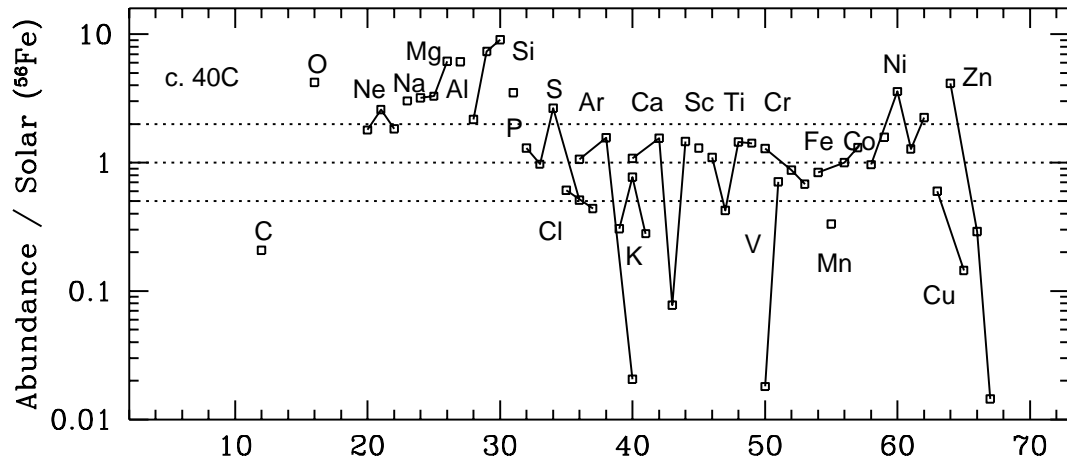
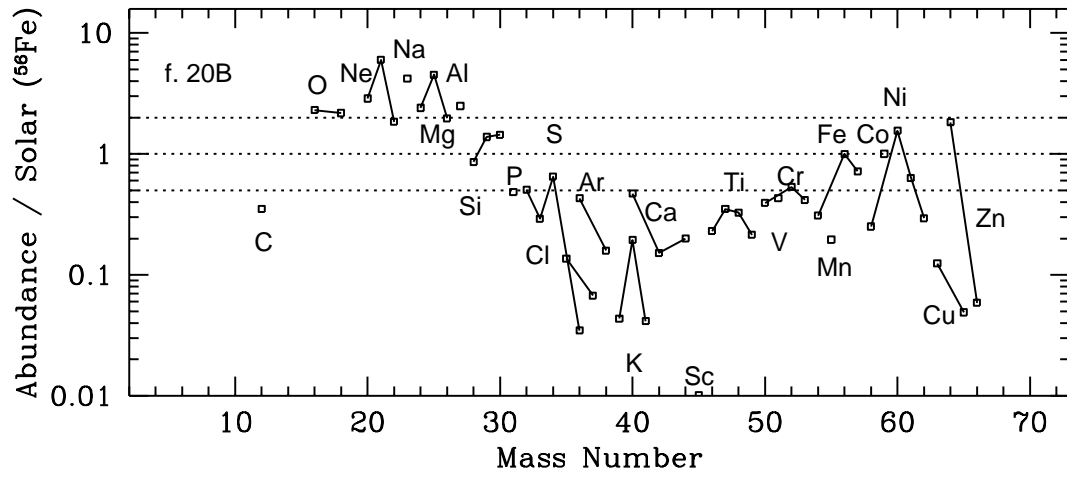
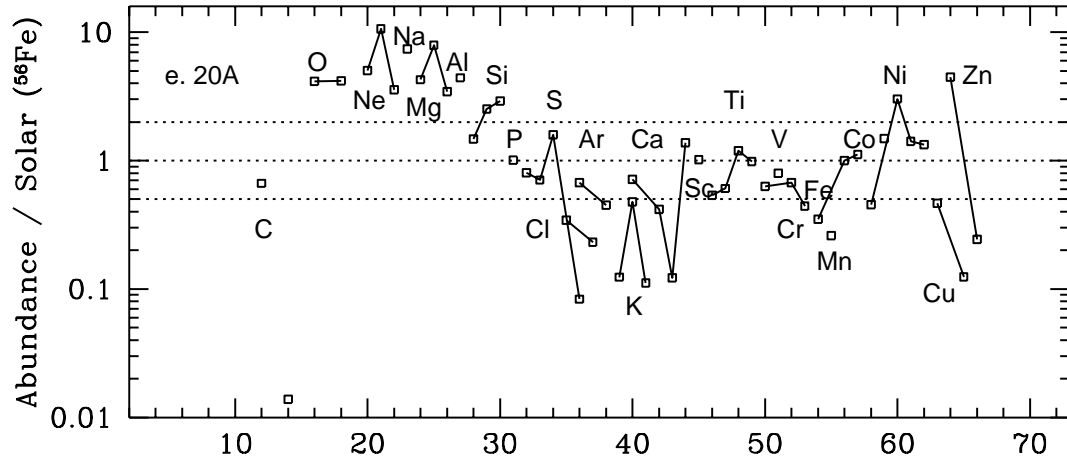


FIG. 14.— Isotopic yields of the bipolar models (a) 40A, (b) 40B, (c) 40C, (d) 40D, (e) 25A, and (f) 25B.





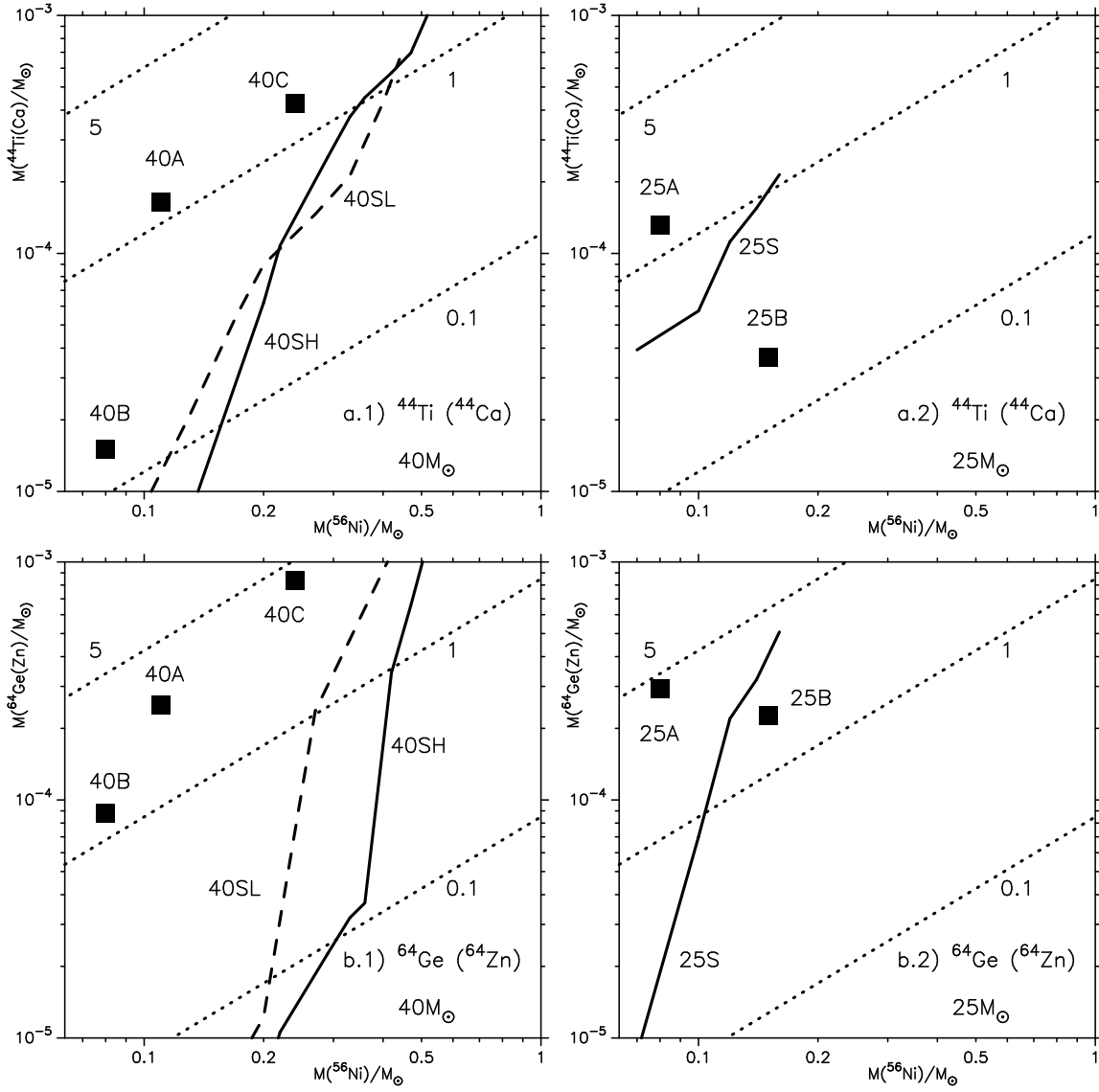


FIG. 15.— Ejected masses of (a) ^{44}Ti and (b) ^{64}Ge against ejected masses of ^{56}Ni for the bipolar models (filled-squares), and for the spherical models 40SH (solid), 40SL (dashed), and 25S (solid). The dashed lines show the ratio between $(^{44}\text{Ca}, ^{64}\text{Zn})/^{56}\text{Ni}$ relative to the solar values.

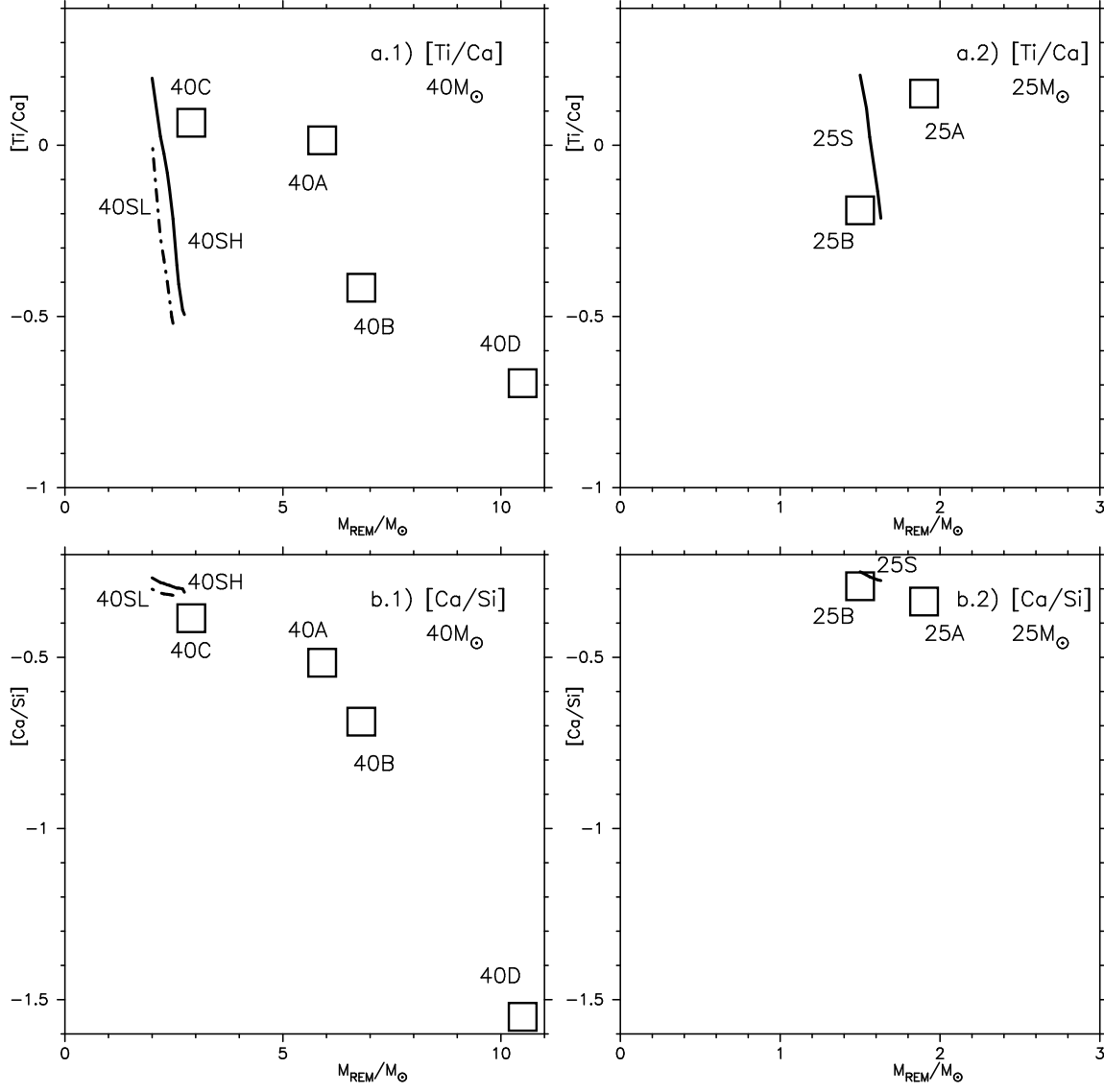
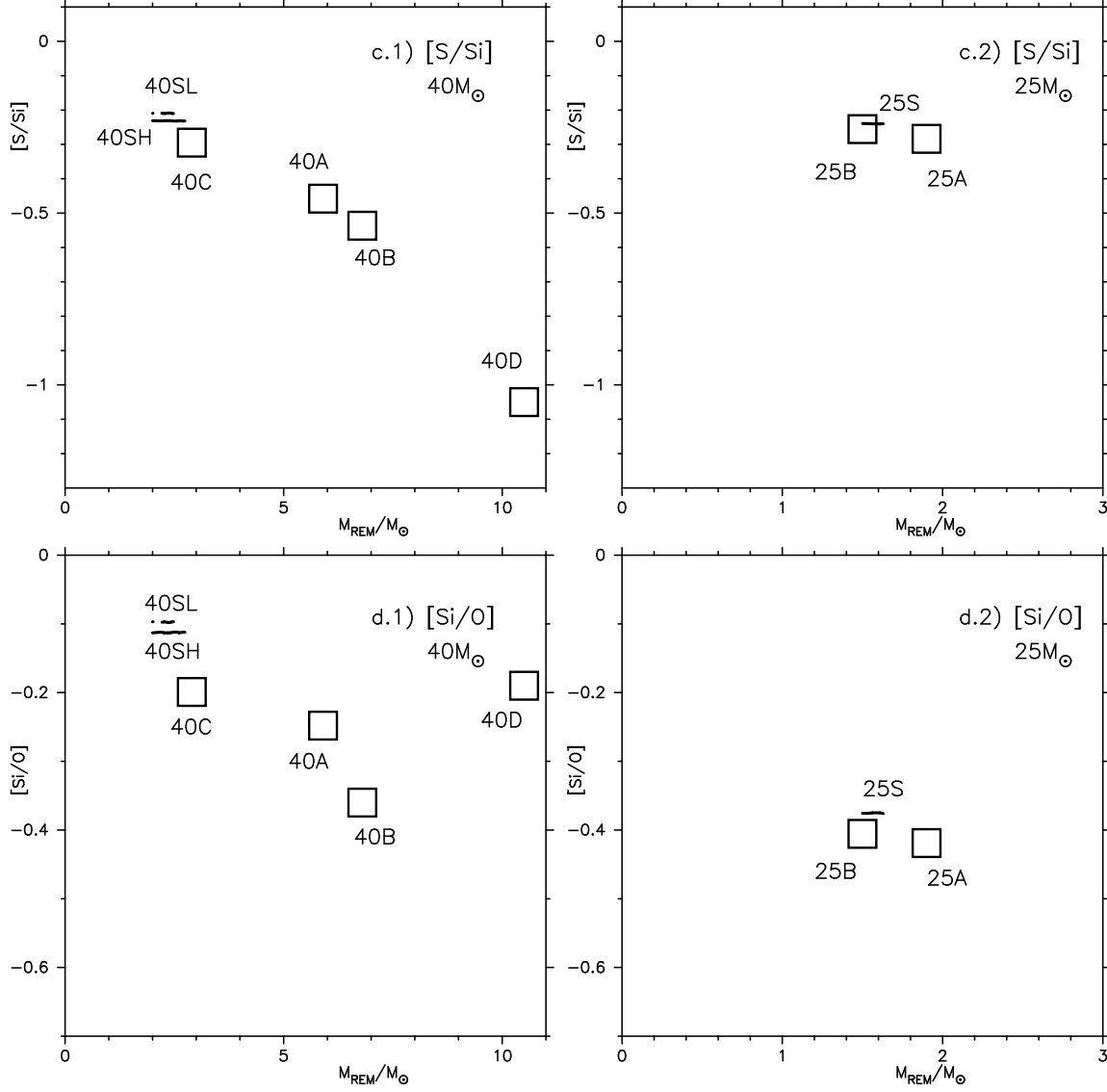
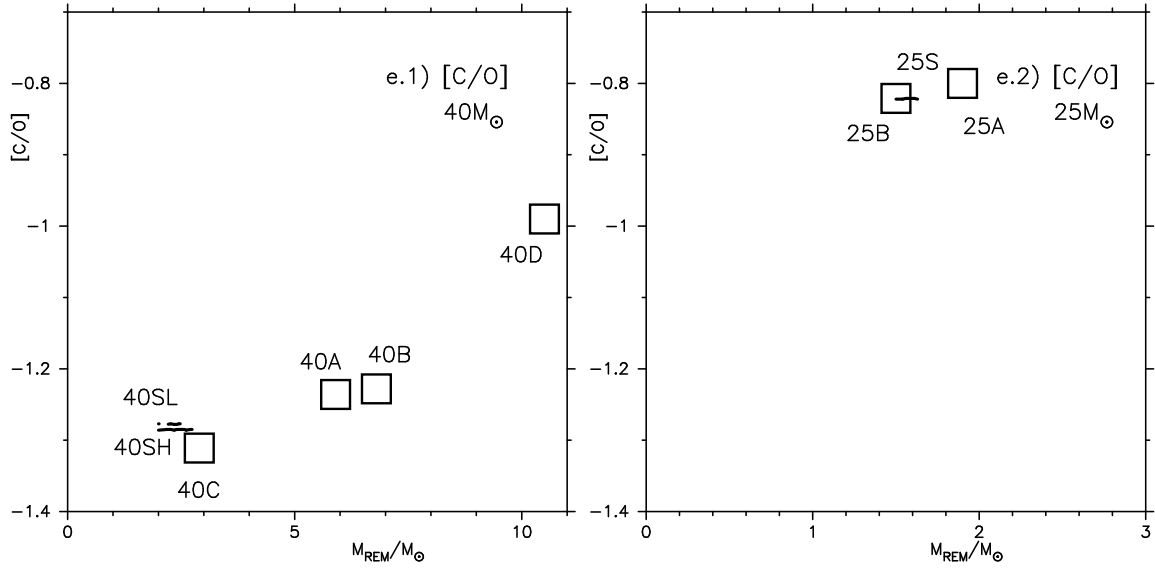


FIG. 16.— Abundance ratios, (a) $[\text{Ti}/\text{Ca}]$, (b) $[\text{Ca}/\text{Si}]$, (c) $[\text{S}/\text{Si}]$, (d) $[\text{Si}/\text{O}]$, and (e) $[\text{C}/\text{O}]$, as a function of the final remnant mass (M_{REM}) for the bipolar models (open squares). The lines show those for the spherical models 40SH (solid), 40SL (dashed), and 25S (solid) with different M_{cut} .





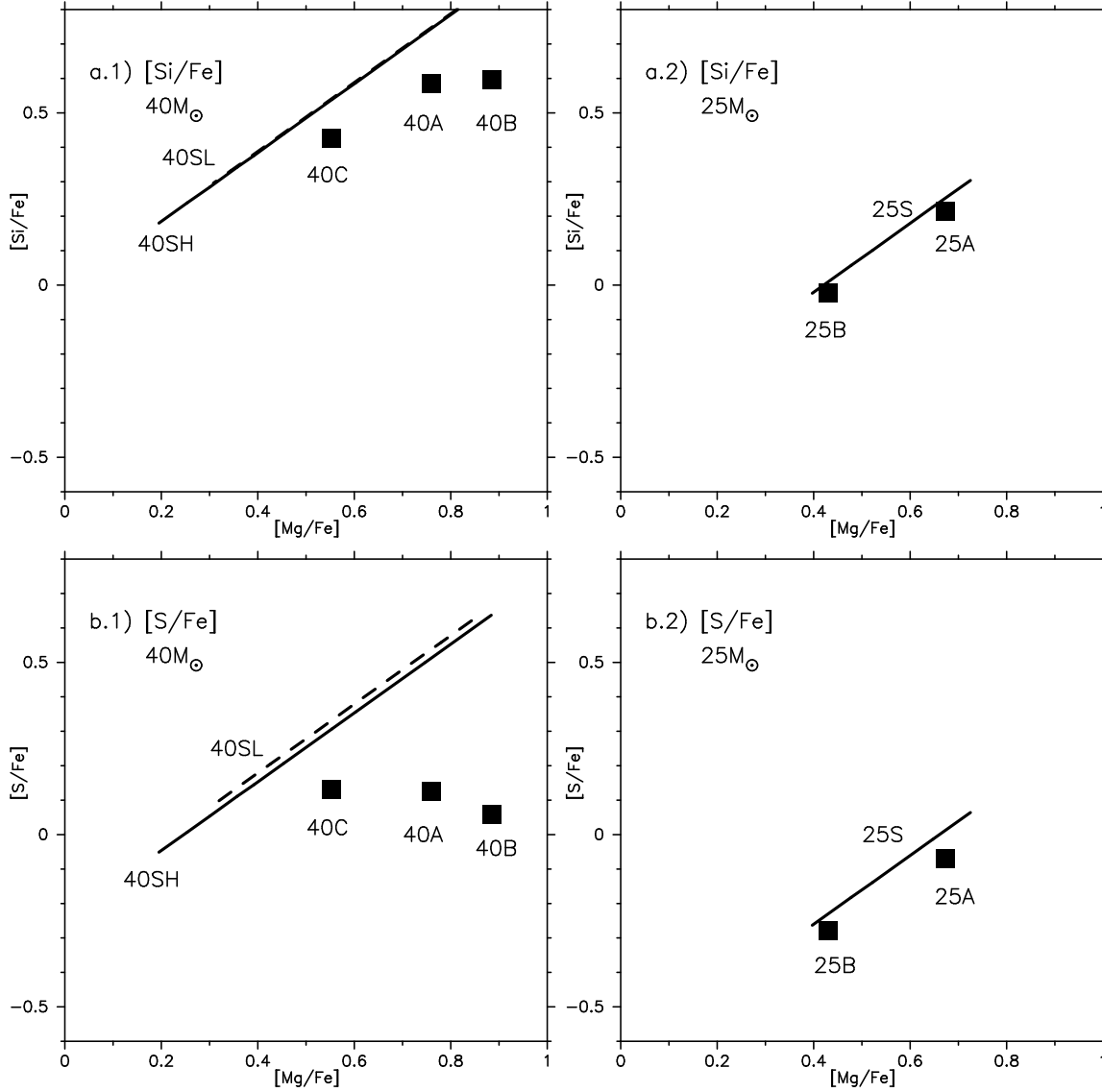
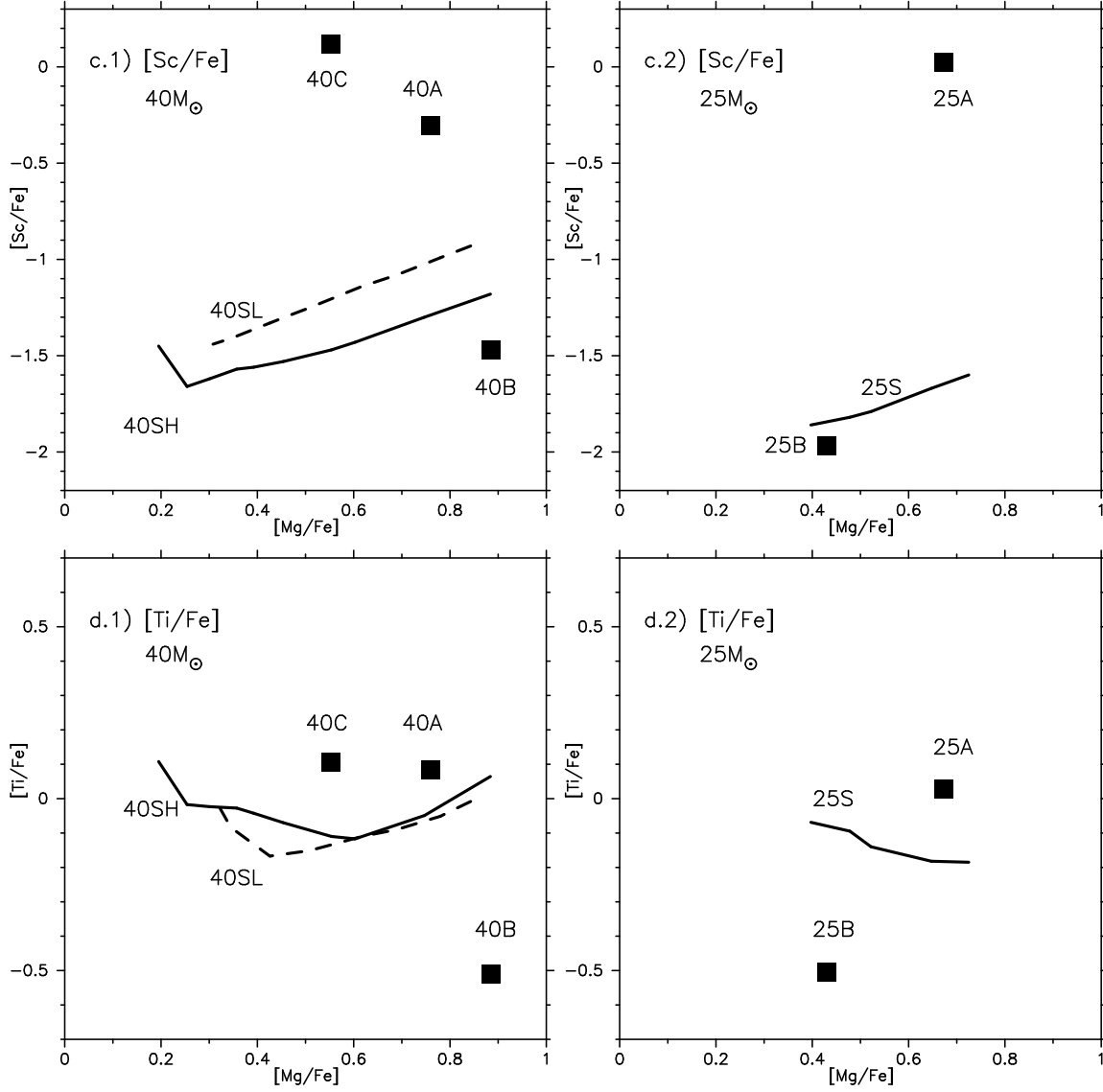
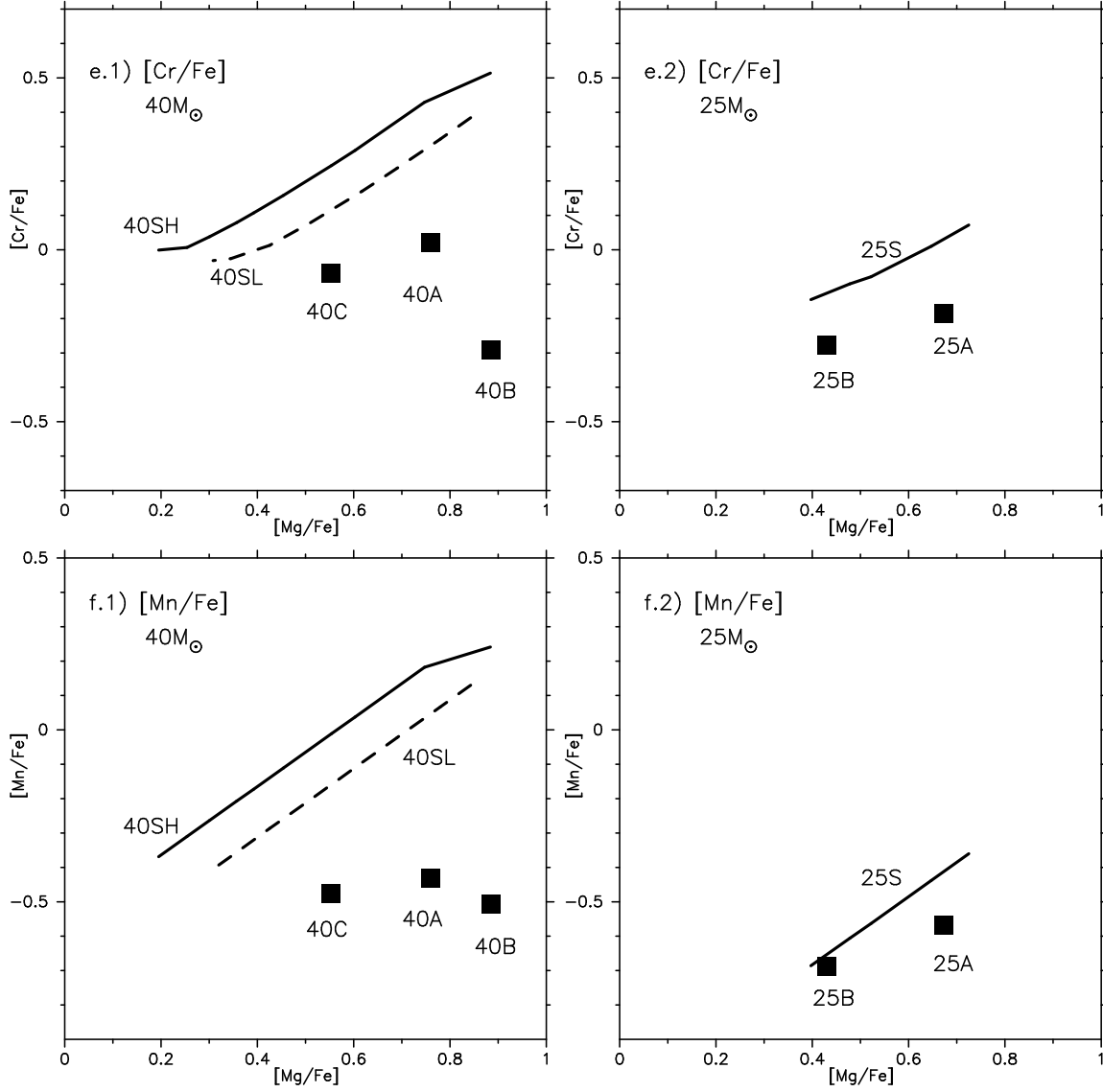
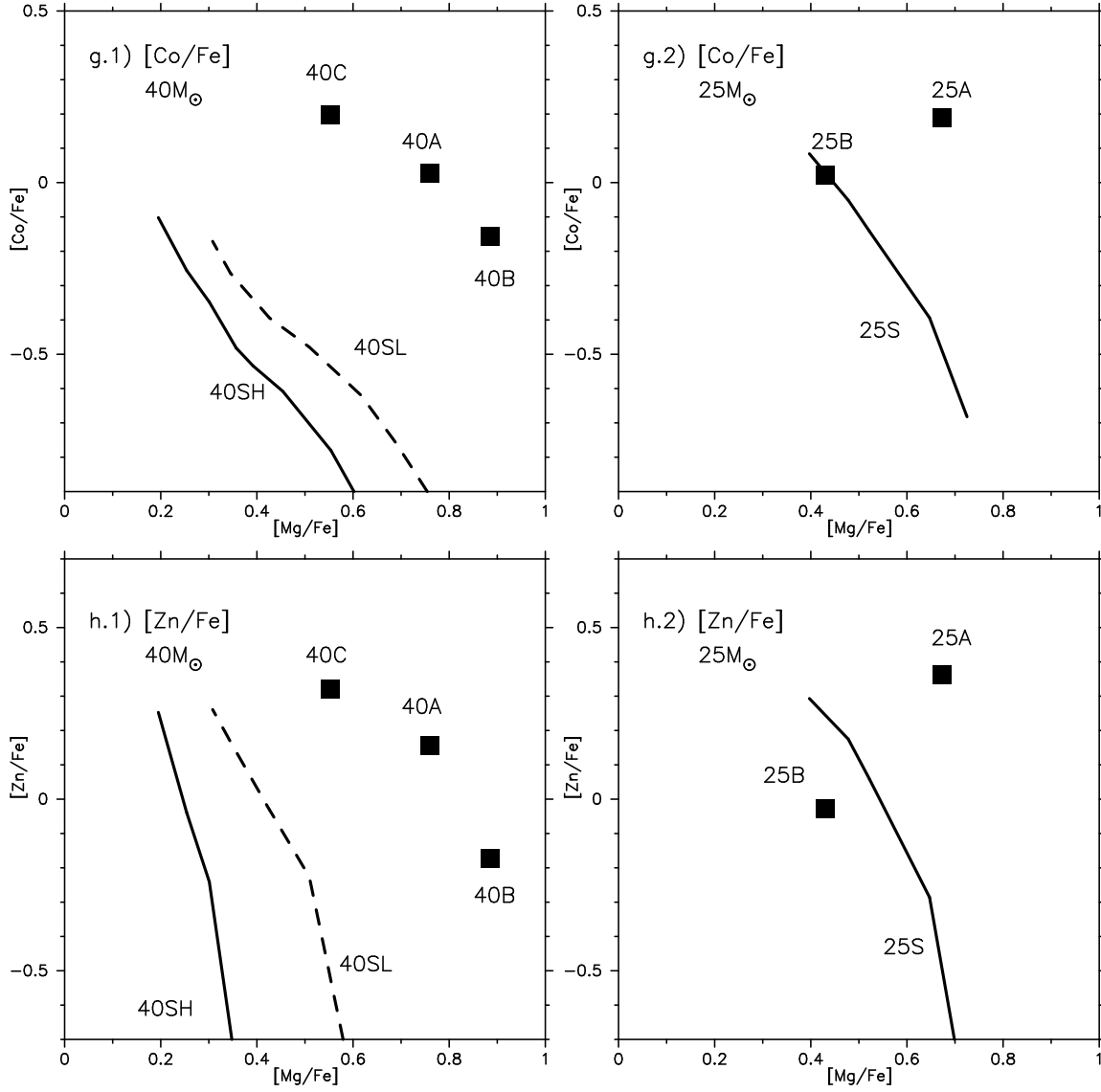


FIG. 17.— Abundances of stable isotopes relative to the solar values, for the bipolar models 40A, 40B, 40C, 25A, 25B (filled squares). The abundances for the spherical models with various M_{cut} are shown for 40SH (solid), 40SL (dashed), and 25S (solid). The isotopes plotted are (a) Si, (b) S, (c) Sc, (d) Ti, (e) Cr, (f) Mn, (g) Co, and (h) Zn.







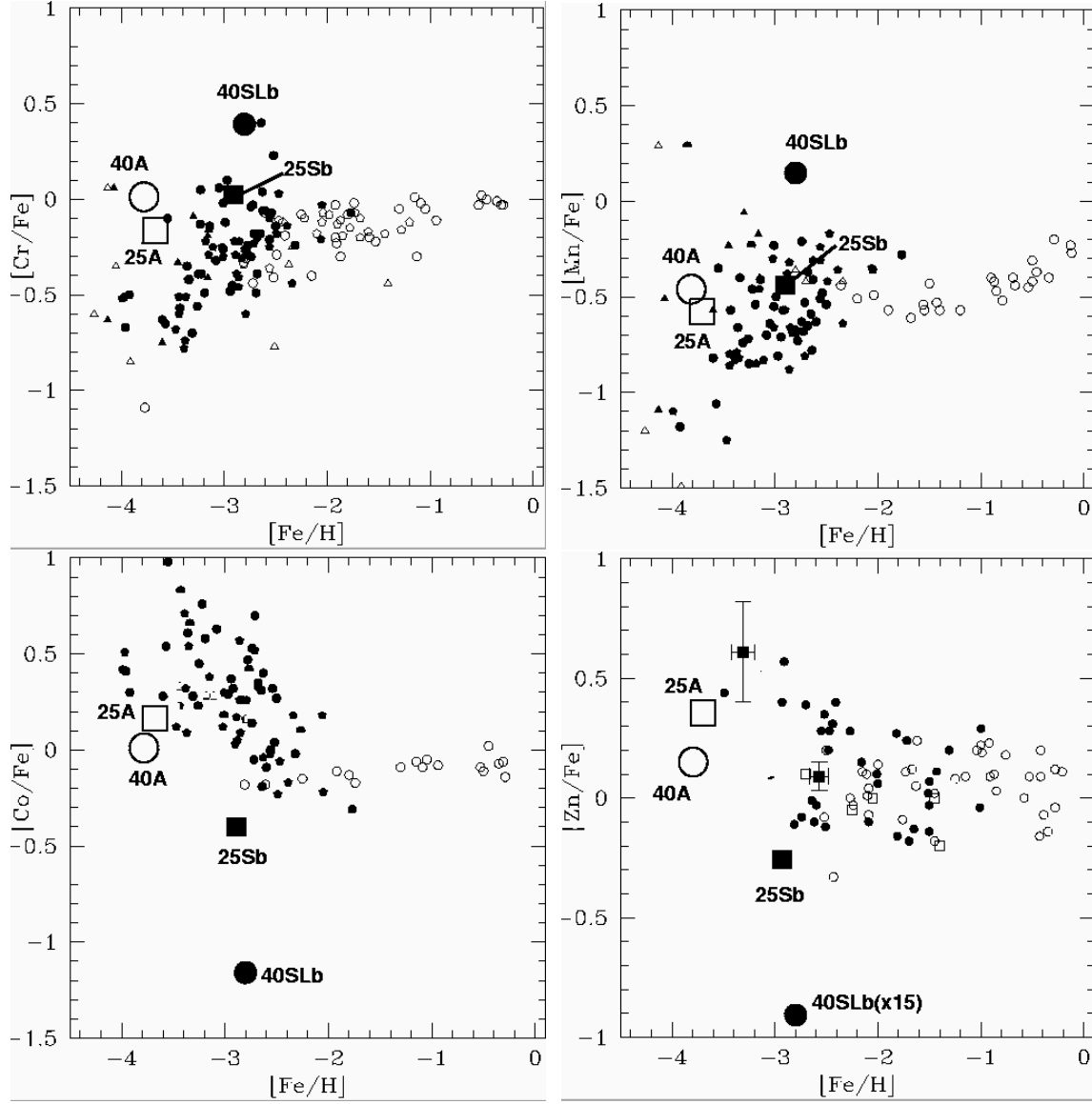


FIG. 18.— Observed abundance ratios of [Zn, Co, Mn, Cr/Fe] (McWilliam et al. 1995; Ryan et al. 1996; Primas et al. 2000; Blake et al. 2001), and the theoretical abundance patterns for normal supernovae (25Sb, 40SLb) and the bipolar models (25A, 40A).

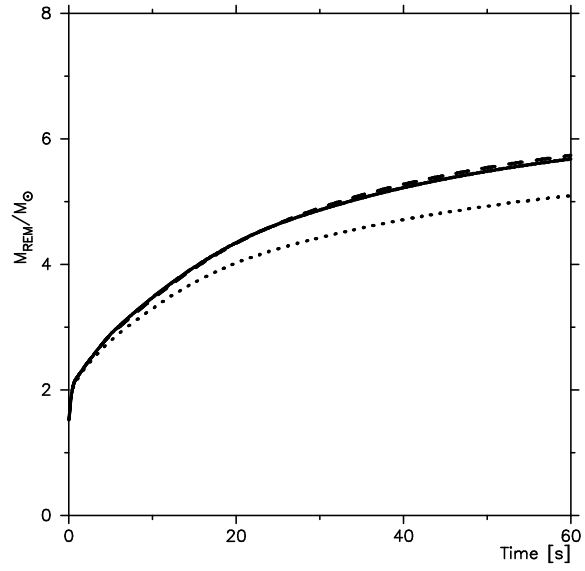


FIG. 19.— The effect of the numerical resolution on the growth of the mass of the central remnant (M_{REM}) for model 40A. The numbers of meshes are 100×30 (solid), 200×60 (dashed), and 70×21 (dotted).

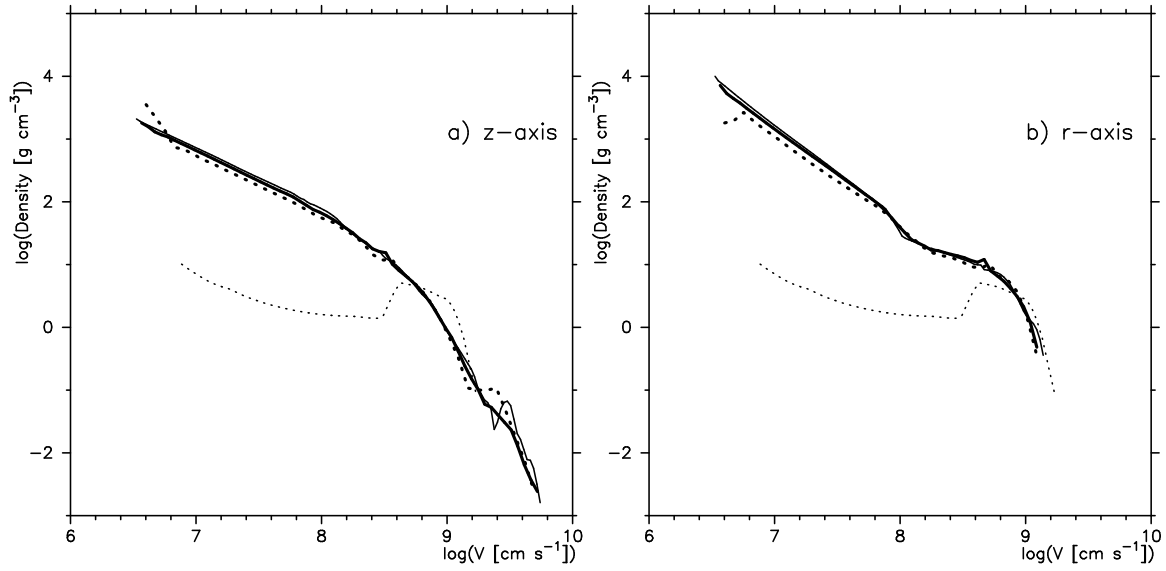


FIG. 20.— The effect of the numerical resolution on the density structure (at 100 sec). (a) Along the z -axis of 40A. The numbers of meshes are 100×30 (thick-solid), 200×60 (thin-solid), and 70×21 (thick-dotted). Also shown is model 40SH with 100×30 (thin-dotted). (b) Along the r -axis.

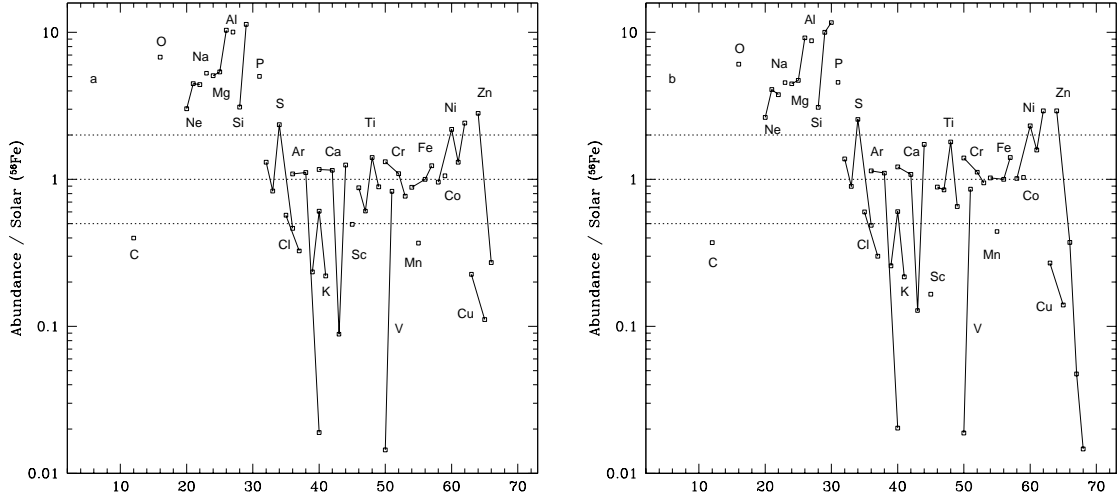


FIG. 21.— The effect of the numerical resolution on the isotopic yields (of model 40A; after decay of radioactive species). (a) The result of the run with 100×30 numerical grids. (b) The result of the run with 200×60 numerical grids.

Model	$M(M_{\odot})$	$M_{\text{REM0}}(M_{\odot})$	α	$\theta_{\text{jet}}(\text{degree})$	$E_{\text{total}}(10^{51}\text{ergs})$	$M_{\text{REM}}(M_{\odot})$	$M(^{56}\text{Ni})(M_{\odot})$
40A	40	1.5	0.01	15	10.9	5.9	1.07E-1
40B	40	1.5	0.01	45	1.2	6.8	8.11E-2
40C	40	1.5	0.05	15	32.4	2.9	2.40E-1
40D	40	3.0	0.01	15	8.5	10.5	6.28E-8
40SHa	40				10.0	2.0	5.40E-1
40SHb	40				10.0	2.7	1.00E-1
40SLa	40				1.0	2.0	4.38E-1
40SLb	40				1.0	2.5	1.00E-1
25A	25	1.0	0.01	15	6.7	1.9	7.81E-2
25B	25	1.0	0.01	45	0.6	1.5	1.51E-1
25Sa	25				1.0	1.5	1.64E-1
25Sb	25				1.0	1.6	1.00E-1

TABLE 1

Models

Species	40A	40B	40C	40D	Species	40A	40B	40C	40D
$M(^{56}\text{Ni})$	1.1E-01	8.1E-02	2.4E-01	6.3E-08		1.1E-01	8.1E-02	2.4E-01	6.3E-08
⁴ He	1.88E+00	1.85E+00	1.99E+00	1.81E+00	⁴³ Ca	7.30E-07	3.90E-08	1.43E-06	1.15E-08
¹² C	1.11E-01	1.13E-01	1.29E-01	8.44E-02	⁴⁴ Ca	1.64E-04	1.50E-05	4.26E-04	8.51E-08
¹³ C	2.76E-08	3.21E-09	8.95E-08	1.58E-08	⁴⁶ Ca	3.05E-10	8.62E-11	7.92E-10	1.52E-10
¹⁴ N	6.83E-05	6.83E-05	6.84E-05	8.80E-05	⁴⁵ Sc	1.77E-06	9.08E-08	1.04E-05	1.81E-08
¹⁵ N	8.45E-09	2.45E-09	2.63E-08	5.52E-09	⁴⁶ Ti	1.80E-05	1.28E-05	5.05E-05	2.76E-06
¹⁶ O	5.99E+00	5.97E+00	8.29E+00	2.61E+00	⁴⁷ Ti	1.16E-05	1.15E-06	1.81E-05	5.65E-08
¹⁷ O	5.33E-08	1.89E-08	1.44E-07	2.53E-08	⁴⁸ Ti	2.79E-04	4.47E-05	6.41E-04	4.24E-08
¹⁸ O	5.48E-06	5.46E-06	5.54E-06	4.27E-07	⁴⁹ Ti	1.34E-05	3.14E-06	4.76E-05	3.21E-08
¹⁹ F	1.61E-09	1.06E-10	6.52E-09	1.53E-09	⁵⁰ Ti	2.74E-10	3.36E-11	7.72E-10	5.75E-11
²⁰ Ne	4.50E-01	4.66E-01	5.97E-01	1.88E-01	⁵⁰ V	1.23E-09	6.17E-10	3.43E-09	2.18E-10
²¹ Ne	1.70E-03	1.70E-03	2.19E-03	9.75E-04	⁵¹ V	2.87E-05	8.90E-06	5.49E-05	3.13E-07
²² Ne	5.29E-02	5.42E-02	4.90E-02	5.16E-02	⁵⁰ Cr	9.00E-05	7.10E-05	1.96E-04	5.12E-06
²³ Na	1.62E-02	1.71E-02	2.08E-02	6.56E-03	⁵² Cr	1.50E-03	4.85E-04	2.66E-03	3.04E-06
²⁴ Mg	2.40E-01	2.40E-01	3.38E-01	9.85E-02	⁵³ Cr	1.21E-04	6.88E-05	2.39E-04	1.52E-06
²⁵ Mg	3.35E-02	3.40E-02	4.57E-02	1.47E-02	⁵⁴ Cr	5.21E-08	3.12E-08	1.23E-07	7.53E-09
²⁶ Mg	7.40E-02	7.59E-02	9.84E-02	3.41E-02	⁵⁵ Mn	4.50E-04	2.84E-04	9.05E-04	6.13E-06
²⁶ Al	3.53E-05	3.10E-05	5.87E-05	1.40E-05	⁵⁴ Fe	5.80E-03	4.83E-03	1.23E-02	1.59E-04
²⁷ Al	5.36E-02	5.46E-02	7.25E-02	2.18E-02	⁵⁶ Fe	1.08E-01	8.12E-02	2.40E-01	2.03E-05
²⁸ Si	1.87E-01	1.34E-01	2.92E-01	9.89E-02	⁵⁷ Fe	3.25E-03	1.46E-03	7.70E-03	8.34E-07
²⁹ Si	3.57E-02	3.45E-02	5.18E-02	1.46E-02	⁵⁸ Fe	1.55E-08	8.92E-09	3.72E-08	2.24E-09
³⁰ Si	2.73E-02	2.38E-02	4.37E-02	1.12E-02	⁵⁹ Co	3.27E-04	1.61E-04	1.08E-03	1.48E-07
³¹ P	3.77E-03	3.38E-03	5.88E-03	1.54E-03	⁵⁸ Ni	4.35E-03	7.21E-04	9.79E-03	9.57E-06
³² S	4.76E-02	3.09E-02	1.06E-01	5.27E-03	⁶⁰ Ni	3.94E-03	1.65E-03	1.44E-02	6.62E-07
³³ S	2.47E-04	1.29E-04	6.43E-04	8.64E-05	⁶¹ Ni	1.03E-04	2.09E-05	2.25E-04	1.70E-10
³⁴ S	3.29E-03	1.86E-03	9.18E-03	1.17E-03	⁶² Ni	6.17E-04	1.61E-05	1.28E-03	6.65E-11
³⁶ S	4.00E-06	1.20E-06	9.82E-06	1.73E-06	⁶⁴ Ni	1.93E-13	2.98E-14	3.21E-13	1.20E-16
³⁵ Cl	1.33E-04	9.22E-05	3.17E-04	4.80E-05	⁶³ Cu	1.20E-05	3.43E-06	7.09E-05	1.51E-12
³⁷ Cl	2.56E-05	1.72E-05	7.72E-05	5.17E-06	⁶⁵ Cu	2.71E-06	9.05E-07	7.89E-06	1.58E-15
³⁶ Ar	7.76E-03	4.64E-03	1.69E-02	5.51E-04	⁶⁴ Zn	2.57E-04	9.45E-05	8.48E-04	2.45E-12
³⁸ Ar	1.58E-03	1.24E-03	4.92E-03	4.03E-04	⁶⁶ Zn	1.47E-05	1.05E-06	3.51E-05	4.99E-15
⁴⁰ Ar	4.59E-08	1.34E-08	1.11E-07	1.91E-08	⁶⁷ Zn	4.44E-08	1.14E-09	2.60E-07	6.43E-18
³⁹ K	7.47E-05	5.56E-05	2.17E-04	1.76E-05	⁶⁸ Zn	1.71E-08	4.68E-10	1.65E-07	8.35E-17
⁴⁰ K	2.49E-08	1.23E-08	7.03E-08	8.54E-09	⁶⁹ Ga	1.20E-10	2.07E-11	6.90E-10	4.19E-17
⁴¹ K	5.33E-06	4.06E-06	1.51E-05	9.14E-07	⁷¹ Ga	3.96E-11	1.06E-11	1.98E-10	7.12E-18
⁴⁰ Ca	6.43E-03	3.38E-03	1.33E-02	2.99E-04	⁷⁰ Ge	2.21E-10	4.15E-11	9.91E-10	2.36E-16
⁴² Ca	4.45E-05	3.83E-05	1.34E-04	8.70E-06					

TABLE 2

Detailed yields (M_{\odot}) after decay of radioactive species: For models 40A, 40B, 40C, and 40D.

Species	40SHa	40SHb	40SLa	40SLb	Species	40SHa	40SHb	40SLa	40SLb
$M(^{56}\text{Ni})$	5.4E-01	1.0E-01	4.4E-01	1.0E-01		5.4E-01	1.0E-01	4.4E-01	1.0E-01
⁴ He	2.01E+00	1.79E+00	1.90E+00	1.83E+00	⁴³ Ca	3.85E-06	8.75E-08	1.14E-06	8.94E-08
¹² C	1.46E-01	1.46E-01	1.51E-01	1.49E-01	⁴⁴ Ca	1.18E-03	6.76E-06	6.52E-04	6.90E-06
¹³ C	1.83E-08	1.83E-08	1.53E-08	1.87E-08	⁴⁶ Ca	1.09E-09	1.09E-09	5.30E-10	1.11E-09
¹⁴ N	8.19E-05	8.19E-05	8.19E-05	8.36E-05	⁴⁵ Sc	6.42E-07	2.45E-07	5.33E-07	2.51E-07
¹⁵ N	1.46E-08	1.46E-08	1.11E-08	1.49E-08	⁴⁶ Ti	2.78E-05	2.20E-05	8.62E-05	2.24E-05
¹⁶ O	8.82E+00	8.82E+00	8.94E+00	9.01E+00	⁴⁷ Ti	5.36E-05	5.85E-07	5.14E-05	5.98E-07
¹⁷ O	1.05E-07	1.05E-07	8.36E-08	1.07E-07	⁴⁸ Ti	1.61E-03	2.73E-04	9.51E-04	2.79E-04
¹⁸ O	3.13E-06	3.13E-06	3.13E-06	3.19E-06	⁴⁹ Ti	4.54E-05	2.63E-05	2.19E-05	2.68E-05
¹⁹ F	5.68E-10	5.46E-10	4.78E-10	5.58E-10	⁵⁰ Ti	8.35E-10	8.35E-10	2.04E-10	8.53E-10
²⁰ Ne	5.93E-01	5.93E-01	6.43E-01	6.05E-01	⁵⁰ V	2.30E-09	2.30E-09	3.98E-09	2.35E-09
²¹ Ne	2.19E-03	2.19E-03	2.36E-03	2.24E-03	⁵¹ V	1.15E-04	5.11E-05	1.06E-04	5.22E-05
²² Ne	5.31E-02	5.31E-02	5.32E-02	5.42E-02	⁵⁰ Cr	3.63E-04	3.45E-04	4.07E-04	3.52E-04
²³ Na	2.09E-02	2.09E-02	2.30E-02	2.13E-02	⁵² Cr	7.27E-03	4.62E-03	5.31E-03	4.72E-03
²⁴ Mg	3.42E-01	3.42E-01	3.51E-01	3.49E-01	⁵³ Cr	6.57E-04	5.81E-04	4.89E-04	5.93E-04
²⁵ Mg	4.44E-02	4.44E-02	4.76E-02	4.53E-02	⁵⁴ Cr	8.86E-08	8.86E-08	2.11E-07	9.04E-08
²⁶ Mg	9.82E-02	9.82E-02	1.06E-01	1.00E-01	⁵⁵ Mn	2.66E-03	2.22E-03	1.97E-03	2.26E-03
²⁶ Al	5.88E-05	5.52E-05	5.36E-05	5.63E-05	⁵⁴ Fe	3.19E-02	2.99E-02	2.75E-02	3.05E-02
²⁷ Al	7.41E-02	7.41E-02	7.81E-02	7.56E-02	⁵⁶ Fe	5.44E-01	9.04E-02	4.38E-01	9.23E-02
²⁸ Si	4.00E-01	4.00E-01	4.30E-01	4.08E-01	⁵⁷ Fe	1.81E-02	1.40E-03	1.18E-02	1.43E-03
²⁹ Si	5.34E-02	5.34E-02	5.37E-02	5.45E-02	⁵⁸ Fe	2.72E-08	2.71E-08	5.95E-08	2.76E-08
³⁰ Si	4.92E-02	4.92E-02	4.27E-02	5.02E-02	⁵⁹ Co	1.24E-03	3.17E-06	8.51E-04	3.24E-06
³¹ P	6.52E-03	6.51E-03	6.07E-03	6.64E-03	⁵⁸ Ni	2.34E-02	2.40E-03	1.31E-02	2.45E-03
³² S	1.61E-01	1.61E-01	1.81E-01	1.65E-01	⁶⁰ Ni	1.82E-02	8.61E-06	1.38E-02	8.79E-06
³³ S	7.36E-04	7.32E-04	7.45E-04	7.47E-04	⁶¹ Ni	6.45E-04	1.73E-09	3.62E-04	1.77E-09
³⁴ S	1.14E-02	1.13E-02	1.02E-02	1.16E-02	⁶² Ni	3.97E-03	1.06E-09	1.79E-03	1.08E-09
³⁶ S	1.21E-05	1.21E-05	8.53E-06	1.24E-05	⁶⁴ Ni	8.54E-13	7.41E-16	2.70E-13	7.56E-16
³⁵ Cl	4.25E-04	3.70E-04	5.28E-04	3.78E-04	⁶³ Cu	5.12E-05	1.14E-11	3.36E-05	1.16E-11
³⁷ Cl	4.30E-05	4.26E-05	9.27E-05	4.35E-05	⁶⁵ Cu	1.78E-05	1.14E-14	1.55E-05	1.16E-14
³⁶ Ar	2.63E-02	2.58E-02	2.88E-02	2.64E-02	⁶⁴ Zn	1.63E-03	2.72E-11	1.36E-03	2.77E-11
³⁸ Ar	4.05E-03	4.03E-03	8.21E-03	4.12E-03	⁶⁶ Zn	9.80E-05	3.76E-14	5.61E-05	3.84E-14
⁴⁰ Ar	1.43E-07	1.43E-07	9.83E-08	1.46E-07	⁶⁷ Zn	2.21E-07	1.09E-15	7.63E-08	1.11E-15
³⁹ K	2.23E-04	1.88E-04	4.22E-04	1.91E-04	⁶⁸ Zn	7.06E-08	2.85E-14	3.05E-08	2.91E-14
⁴⁰ K	5.51E-08	5.49E-08	6.95E-08	5.60E-08	⁶⁹ Ga	5.39E-10	1.12E-15	4.78E-10	1.14E-15
⁴¹ K	8.72E-06	7.47E-06	2.27E-05	7.62E-06	⁷¹ Ga	1.74E-10	7.65E-17	1.75E-10	7.81E-17
⁴⁰ Ca	2.24E-02	2.14E-02	2.21E-02	2.18E-02	⁷⁰ Ge	7.95E-10	8.72E-14	7.34E-10	8.90E-14
⁴² Ca	6.49E-05	6.33E-05	2.16E-04	6.47E-05					

TABLE 3

Detailed yields (M_{\odot}) after decay of radioactive species: For models 40SH and 40SL (with different M_{cut}).

Species	25A	25B	25Sa	25Sb	Species	25A	25B	25Sa	25Sb
$M(^{56}\text{Ni})$	7.8E-02	1.5E-01	1.6E-01	1.0E-01		7.8E-02	1.5E-01	1.6E-01	1.0E-01
⁴ He	1.82E+00	1.80E+00	1.82E+00	1.79E+00	⁴³ Ca	7.33E-07	8.98E-08	7.83E-07	4.47E-07
¹² C	1.35E-01	1.38E-01	1.41E-01	1.41E-01	⁴⁴ Ca	1.31E-04	3.67E-05	2.14E-04	5.73E-05
¹³ C	1.56E-07	2.13E-09	2.22E-09	2.23E-09	⁴⁶ Ca	1.31E-10	9.74E-11	1.20E-10	1.20E-10
¹⁴ N	1.02E-03	1.02E-03	9.57E-04	9.57E-04	⁴⁵ Sc	2.65E-06	5.09E-08	7.26E-08	6.28E-08
¹⁵ N	1.40E-08	1.88E-09	2.04E-09	2.04E-09	⁴⁶ Ti	8.03E-06	6.66E-06	1.32E-05	6.30E-06
¹⁶ O	2.66E+00	2.86E+00	2.91E+00	2.91E+00	⁴⁷ Ti	8.44E-06	9.42E-06	2.50E-05	6.20E-06
¹⁷ O	3.00E-08	1.62E-08	1.77E-08	1.77E-08	⁴⁸ Ti	1.72E-04	9.11E-05	2.90E-04	1.28E-04
¹⁸ O	6.07E-03	6.11E-03	6.13E-03	6.13E-03	⁴⁹ Ti	1.07E-05	4.54E-06	5.62E-06	4.58E-06
¹⁹ F	2.78E-09	2.51E-10	2.81E-10	2.81E-10	⁵⁰ Ti	1.04E-10	4.35E-11	5.60E-11	5.60E-11
²⁰ Ne	5.44E-01	6.02E-01	6.03E-01	6.03E-01	⁵⁰ V	4.00E-10	1.98E-10	2.96E-10	2.96E-10
²¹ Ne	2.92E-03	3.20E-03	3.19E-03	3.19E-03	⁵¹ V	2.01E-05	2.09E-05	5.02E-05	1.53E-05
²² Ne	3.09E-02	3.11E-02	3.13E-02	3.13E-02	⁵⁰ Cr	3.12E-05	3.78E-05	4.84E-05	3.89E-05
²³ Na	1.66E-02	1.82E-02	1.82E-02	1.82E-02	⁵² Cr	6.67E-04	1.03E-03	1.56E-03	1.23E-03
²⁴ Mg	1.47E-01	1.60E-01	1.63E-01	1.63E-01	⁵³ Cr	5.08E-05	9.26E-05	1.04E-04	1.04E-04
²⁵ Mg	3.58E-02	3.95E-02	3.97E-02	3.97E-02	⁵⁴ Cr	1.47E-08	6.85E-09	1.13E-08	1.13E-08
²⁶ Mg	1.79E-02	1.98E-02	1.99E-02	1.99E-02	⁵⁵ Mn	2.32E-04	3.36E-04	3.69E-04	3.67E-04
²⁶ Al	1.10E-02	1.23E-02	1.22E-02	1.22E-02	⁵⁴ Fe	1.67E-03	2.86E-03	3.09E-03	3.09E-03
²⁷ Al	1.71E-02	1.87E-02	1.89E-02	1.89E-02	⁵⁶ Fe	7.81E-02	1.51E-01	1.64E-01	9.07E-02
²⁸ Si	6.45E-02	7.25E-02	7.95E-02	7.95E-02	⁵⁷ Fe	2.12E-03	2.65E-03	4.19E-03	2.55E-03
²⁹ Si	5.78E-03	6.13E-03	6.31E-03	6.30E-03	⁵⁸ Fe	4.92E-09	2.23E-09	3.71E-09	3.71E-09
³⁰ Si	4.59E-03	4.39E-03	4.83E-03	4.82E-03	⁵⁹ Co	3.33E-04	4.35E-04	5.50E-04	1.03E-04
³¹ P	5.50E-04	5.11E-04	5.70E-04	5.68E-04	⁵⁸ Ni	1.50E-03	1.61E-03	2.90E-03	2.07E-03
³² S	2.12E-02	2.59E-02	2.91E-02	2.91E-02	⁶⁰ Ni	3.95E-03	3.94E-03	5.69E-03	2.31E-03
³³ S	1.52E-04	1.22E-04	1.59E-04	1.59E-04	⁶¹ Ni	8.09E-05	7.04E-05	1.58E-04	9.03E-05
³⁴ S	1.53E-03	1.09E-03	1.47E-03	1.46E-03	⁶² Ni	2.48E-04	1.06E-04	4.43E-04	3.98E-04
³⁶ S	5.23E-07	4.22E-07	5.42E-07	5.42E-07	⁶⁴ Ni	1.68E-13	1.00E-14	1.45E-13	1.39E-13
³⁵ Cl	5.82E-05	4.48E-05	6.54E-05	5.56E-05	⁶³ Cu	1.79E-05	9.27E-06	1.53E-05	2.33E-06
³⁷ Cl	1.33E-05	7.44E-06	1.06E-05	1.05E-05	⁶⁵ Cu	2.20E-06	1.68E-06	3.82E-06	9.50E-07
³⁶ Ar	3.48E-03	4.31E-03	4.81E-03	4.76E-03	⁶⁴ Zn	2.97E-04	2.35E-04	5.30E-04	7.24E-05
³⁸ Ar	4.64E-04	3.16E-04	4.88E-04	4.84E-04	⁶⁶ Zn	9.55E-06	4.47E-06	1.80E-05	8.63E-06
⁴⁰ Ar	5.89E-09	4.61E-09	5.87E-09	5.87E-09	⁶⁷ Zn	2.65E-08	2.49E-09	1.98E-08	9.71E-09
³⁹ K	2.87E-05	1.96E-05	3.29E-05	2.82E-05	⁶⁸ Zn	1.19E-08	1.06E-09	7.24E-09	3.21E-09
⁴⁰ K	1.42E-08	1.12E-08	1.41E-08	1.41E-08	⁶⁹ Ga	1.06E-10	6.09E-11	1.73E-10	4.64E-11
⁴¹ K	1.96E-06	1.41E-06	2.07E-06	2.07E-06	⁷¹ Ga	4.51E-11	2.98E-11	6.58E-11	1.91E-11
⁴⁰ Ca	2.86E-03	3.65E-03	4.21E-03	4.14E-03	⁷⁰ Ge	1.43E-10	1.39E-10	2.06E-10	6.46E-11
⁴² Ca	1.17E-05	8.23E-06	1.23E-05	1.23E-05					

TABLE 4

Detailed yields (M_{\odot}) after decay of radioactive species: For models 25A, 25B, and 25S.

Species $M(^{56}\text{Ni})$	40A 1.1E-01	40B 8.1E-02	40C 2.4E-01	40D 6.3E-08
⁴ He	1.88E+00	1.85E+00	1.99E+00	1.81E+00
⁶ Li	3.23E-14	1.46E-15	2.01E-16	2.85E-21
⁷ Li	9.18E-19	2.97E-20	2.55E-19	6.62E-20
⁹ Be	9.97E-17	7.43E-26	3.06E-16	6.76E-17
¹⁰ B	3.25E-15	2.43E-16	2.14E-17	1.30E-22
¹¹ B	2.68E-14	8.48E-15	6.62E-14	1.28E-14
¹² C	1.11E-01	1.13E-01	1.29E-01	8.44E-02
¹³ C	2.76E-08	3.21E-09	8.95E-08	1.58E-08
¹⁴ C	3.99E-08	1.88E-09	1.24E-07	2.35E-08
¹³ N	6.57E-17	3.07E-16	7.89E-16	1.13E-16
¹⁴ N	6.83E-05	6.83E-05	6.84E-05	8.80E-05
¹⁵ N	8.19E-09	2.44E-09	2.55E-08	5.52E-09
¹⁶ N	8.11E-16	4.02E-24	2.25E-15	7.04E-16
¹⁴ O	2.18E-08	8.67E-10	9.32E-08	1.56E-09
¹⁵ O	2.58E-10	1.13E-11	7.94E-10	3.18E-12
¹⁶ O	5.99E+00	5.97E+00	8.29E+00	2.61E+00
¹⁷ O	5.33E-08	1.89E-08	1.44E-07	2.53E-08
¹⁸ O	5.47E-06	5.46E-06	5.48E-06	4.23E-07
¹⁷ F	3.59E-13	9.65E-15	1.28E-12	3.39E-15
¹⁸ F	1.06E-08	5.15E-11	5.96E-08	3.22E-09
¹⁹ F	1.43E-09	1.03E-10	5.92E-09	1.53E-09
²⁰ F	3.66E-10	4.87E-13	1.67E-09	2.27E-10
²¹ F	6.92E-11	2.26E-12	3.54E-10	2.29E-11
¹⁸ Ne	1.10E-12	1.20E-13	4.07E-12	1.46E-14
¹⁹ Ne	1.71E-10	2.84E-12	5.97E-10	5.82E-14
²⁰ Ne	4.50E-01	4.66E-01	5.97E-01	1.88E-01
²¹ Ne	1.70E-03	1.70E-03	2.19E-03	9.75E-04
²² Ne	5.29E-02	5.42E-02	4.90E-02	5.16E-02
²¹ Na	5.15E-09	5.63E-11	2.20E-08	3.43E-11
²² Na	1.29E-07	6.16E-08	3.85E-07	5.83E-08
²³ Na	1.62E-02	1.71E-02	2.08E-02	6.55E-03
²⁴ Na	2.99E-06	1.35E-06	8.33E-06	1.29E-06
²² Mg	6.55E-08	1.38E-09	2.15E-07	4.56E-17
²³ Mg	1.41E-06	4.64E-07	4.04E-06	5.03E-07
²⁴ Mg	2.40E-01	2.40E-01	3.38E-01	9.85E-02
²⁵ Mg	3.35E-02	3.40E-02	4.57E-02	1.47E-02
²⁶ Mg	7.40E-02	7.59E-02	9.84E-02	3.41E-02
²⁷ Mg	2.99E-05	3.81E-07	1.21E-04	2.71E-05
²⁴ Al	5.30E-09	6.60E-10	8.90E-09	2.34E-21
²⁵ Al	3.09E-07	2.58E-08	6.53E-07	9.13E-10
²⁶ Al	3.39E-05	3.10E-05	5.45E-05	1.40E-05
²⁷ Al	5.36E-02	5.46E-02	7.24E-02	2.18E-02
²⁸ Al	7.52E-05	2.91E-05	2.00E-04	3.23E-05
²⁹ Al	8.39E-07	3.08E-07	2.35E-06	3.56E-07
²⁶ Si	1.34E-06	1.69E-08	4.21E-06	5.48E-15
²⁷ Si	1.18E-06	1.83E-07	2.95E-06	1.68E-07
²⁸ Si	1.86E-01	1.34E-01	2.91E-01	9.89E-02
²⁹ Si	3.57E-02	3.45E-02	5.18E-02	1.46E-02
³⁰ Si	2.72E-02	2.38E-02	4.36E-02	1.12E-02
²⁸ P	5.52E-08	3.66E-10	2.07E-07	1.46E-20
²⁹ P	2.97E-06	1.15E-07	1.54E-06	4.12E-12
³⁰ P	9.26E-06	3.36E-06	9.51E-06	1.63E-06
³¹ P	3.76E-03	3.38E-03	5.87E-03	1.54E-03
³² P	6.44E-06	2.14E-06	1.63E-05	2.81E-06
³³ P	2.74E-06	8.04E-07	6.88E-06	1.19E-06
³⁴ P	1.95E-09	4.58E-10	5.71E-09	6.27E-10
³⁰ S	3.90E-06	5.51E-08	6.02E-06	2.51E-17
³¹ S	4.09E-06	2.86E-07	5.71E-06	2.89E-09
³² S	4.76E-02	3.09E-02	1.06E-01	5.27E-03
³³ S	2.44E-04	1.28E-04	6.35E-04	8.52E-05
³⁴ S	3.29E-03	1.86E-03	9.17E-03	1.17E-03
³⁵ S	3.59E-06	1.20E-06	9.01E-06	1.63E-06
³⁶ S	4.01E-06	1.20E-06	9.82E-06	1.73E-06
³¹ Cl	2.09E-15	1.23E-16	1.36E-14	0.00E+00
³² Cl	2.94E-08	1.69E-09	1.43E-07	4.23E-22
³³ Cl	4.56E-07	3.33E-08	1.75E-06	3.21E-13
³⁴ Cl	2.90E-06	3.60E-07	3.66E-06	9.26E-10
³⁵ Cl	1.26E-04	9.08E-05	2.98E-04	4.64E-05
³⁶ Cl	1.82E-06	5.96E-07	4.53E-06	7.88E-07
³⁷ Cl	3.13E-06	9.75E-07	7.86E-06	1.32E-06
³⁸ Cl	1.88E-10	5.09E-11	4.67E-10	7.10E-11

TABLE 5

Detailed yields (M_{\odot}) before decay of radioactive species: For models 40A, 40B, 40C, and 40D

Species	40A	40B	40C	40D
$M(^{56}\text{Ni})$	1.1E-01	8.1E-02	2.4E-01	6.3E-08
³³ Ar	1.17E-10	5.41E-11	3.81E-10	1.44E-21
³⁴ Ar	2.35E-06	2.77E-08	9.49E-06	5.87E-20
³⁵ Ar	3.42E-06	1.79E-07	1.02E-05	2.23E-13
³⁶ Ar	7.75E-03	4.64E-03	1.69E-02	5.50E-04
³⁷ Ar	2.13E-05	1.62E-05	6.14E-05	3.85E-06
³⁸ Ar	1.57E-03	1.24E-03	4.92E-03	4.03E-04
³⁹ Ar	1.53E-08	5.06E-09	3.90E-08	6.72E-09
⁴⁰ Ar	4.59E-08	1.34E-08	1.11E-07	1.91E-08
⁴¹ Ar	1.43E-11	4.44E-12	3.45E-11	6.78E-12
³⁵ K	1.37E-16	8.07E-18	9.80E-16	4.00E-24
³⁶ K	8.71E-09	1.77E-10	3.89E-08	1.06E-21
³⁷ K	1.18E-06	4.30E-09	7.95E-06	1.35E-17
³⁸ K	1.14E-06	9.37E-08	3.30E-06	8.87E-11
³⁹ K	7.38E-05	5.55E-05	2.14E-04	1.76E-05
⁴⁰ K	2.49E-08	1.23E-08	7.03E-08	8.54E-09
⁴¹ K	2.17E-08	7.18E-09	5.43E-08	9.24E-09
⁴² K	5.64E-10	1.77E-10	1.37E-09	2.54E-10
⁴³ K	9.84E-11	2.92E-11	2.43E-10	4.23E-11
³⁷ Ca	6.97E-10	4.71E-11	2.32E-09	2.40E-21
³⁸ Ca	3.51E-07	1.64E-09	2.03E-06	9.65E-22
³⁹ Ca	9.31E-07	1.11E-08	2.97E-06	3.20E-16
⁴⁰ Ca	6.43E-03	3.38E-03	1.33E-02	2.99E-04
⁴¹ Ca	5.30E-06	4.05E-06	1.50E-05	9.05E-07
⁴² Ca	4.45E-05	3.83E-05	1.34E-04	8.70E-06
⁴³ Ca	4.37E-08	3.06E-08	1.32E-07	1.11E-08
⁴⁴ Ca	2.67E-08	8.98E-09	7.83E-08	9.42E-09
⁴⁵ Ca	5.61E-11	1.41E-11	1.39E-10	2.36E-11
⁴⁶ Ca	5.59E-11	1.50E-11	1.41E-10	2.30E-11
⁴⁰ Sc	4.42E-14	3.03E-15	1.47E-13	1.12E-23
⁴¹ Sc	3.93E-09	2.48E-10	2.61E-08	1.11E-21
⁴² Sc	4.92E-09	6.36E-11	1.67E-08	2.53E-17
⁴³ Sc	6.58E-07	8.32E-09	1.08E-06	3.36E-10
⁴⁴ Sc	2.11E-09	1.55E-09	6.23E-09	4.15E-10
⁴⁵ Sc	1.33E-08	8.95E-09	3.95E-08	3.74E-09
⁴⁶ Sc	2.50E-10	7.12E-11	6.51E-10	1.29E-10
⁴⁷ Sc	6.89E-11	1.90E-11	1.79E-10	2.67E-11
⁴⁸ Sc	2.40E-12	6.88E-13	5.75E-12	9.15E-13
⁴⁹ Sc	9.70E-14	2.53E-14	2.28E-13	3.35E-14
⁴² Ti	6.33E-11	2.53E-11	2.93E-10	1.30E-21
⁴³ Ti	2.82E-08	9.28E-11	2.15E-07	2.07E-21
⁴⁴ Ti	1.64E-04	1.50E-05	4.26E-04	7.52E-08
⁴⁵ Ti	8.78E-07	8.12E-08	3.96E-06	1.43E-08
⁴⁶ Ti	1.77E-05	1.28E-05	4.88E-05	2.76E-06
⁴⁷ Ti	3.22E-07	2.29E-07	9.18E-07	5.56E-08
⁴⁸ Ti	1.27E-07	6.80E-08	3.65E-07	2.40E-08
⁴⁹ Ti	3.75E-10	8.89E-11	1.06E-09	8.04E-11
⁵⁰ Ti	2.74E-10	3.36E-11	7.72E-10	5.75E-11
⁵¹ Ti	2.81E-14	1.17E-15	2.24E-14	6.24E-17
⁴⁴ V	1.34E-10	8.02E-12	2.36E-09	1.03E-21
⁴⁵ V	8.81E-07	6.43E-10	6.38E-06	3.02E-21
⁴⁶ V	2.99E-07	2.10E-10	1.38E-06	3.17E-18
⁴⁷ V	1.04E-05	9.18E-07	1.38E-05	8.74E-10
⁴⁸ V	4.42E-08	3.09E-08	1.19E-07	6.61E-09
⁴⁹ V	9.55E-08	6.52E-08	2.55E-07	1.45E-08
⁵⁰ V	1.23E-09	6.17E-10	3.43E-09	2.18E-10
⁵¹ V	9.19E-09	4.55E-09	2.59E-08	1.54E-09
⁵² V	1.95E-13	3.54E-14	5.16E-13	3.06E-14
⁵³ V	2.59E-14	5.19E-16	2.43E-14	7.78E-17
⁴⁶ Cr	6.03E-08	1.04E-11	3.28E-07	2.30E-21
⁴⁷ Cr	9.13E-07	3.47E-09	3.36E-06	3.96E-21
⁴⁸ Cr	2.79E-04	4.46E-05	6.41E-04	1.17E-08
⁴⁹ Cr	1.19E-05	3.07E-06	3.53E-05	1.76E-08
⁵⁰ Cr	8.91E-05	7.10E-05	1.92E-04	5.13E-06
⁵¹ Cr	2.03E-06	1.45E-06	5.26E-06	3.08E-07
⁵² Cr	2.00E-05	1.33E-05	4.70E-05	3.01E-06
⁵³ Cr	4.51E-09	2.35E-09	1.10E-08	6.45E-10
⁵⁴ Cr	1.31E-10	5.38E-11	3.29E-10	1.84E-11
⁵⁵ Cr	1.22E-14	2.51E-15	3.80E-14	1.80E-18
⁴⁸ Mn	5.67E-10	2.33E-13	1.73E-09	4.52E-22
⁴⁹ Mn	1.43E-06	9.18E-10	1.21E-05	1.85E-21
⁵⁰ Mn	8.66E-07	8.50E-10	4.56E-06	2.40E-18

Species	40A	40B	40C	40D
$M(^{56}\text{Ni})$	1.1E-01	8.1E-02	2.4E-01	6.3E-08
⁵¹ Mn	2.65E-05	7.45E-06	4.84E-05	3.92E-09
⁵² Mn	4.55E-07	3.24E-07	8.52E-07	2.17E-08
⁵³ Mn	1.03E-05	7.51E-06	2.35E-05	1.48E-06
⁵⁴ Mn	5.20E-08	3.12E-08	1.23E-07	7.52E-09
⁵⁵ Mn	1.81E-08	9.76E-09	4.32E-08	2.49E-09
⁵⁶ Mn	1.03E-13	2.71E-14	2.10E-13	8.74E-15
⁵⁷ Mn	2.52E-14	2.23E-16	3.35E-14	2.07E-17
⁵⁰ Fe	7.69E-09	1.66E-12	6.42E-08	6.82E-22
⁵¹ Fe	1.97E-07	2.72E-11	1.22E-06	3.88E-21
⁵² Fe	1.48E-03	4.72E-04	2.62E-03	5.20E-09
⁵³ Fe	1.11E-04	6.13E-05	2.16E-04	3.61E-08
⁵⁴ Fe	5.80E-03	4.82E-03	1.23E-02	1.59E-04
⁵⁵ Fe	4.36E-05	3.10E-05	9.92E-05	6.06E-06
⁵⁶ Fe	1.31E-04	8.71E-05	3.15E-04	2.02E-05
⁵⁷ Fe	1.50E-08	7.85E-09	3.65E-08	2.17E-09
⁵⁸ Fe	8.39E-10	3.98E-10	2.07E-09	1.11E-10
⁵⁹ Fe	4.05E-14	2.51E-15	6.54E-14	3.06E-17
⁶⁰ Fe	4.57E-14	2.19E-15	5.74E-14	1.03E-17
⁵² Co	2.88E-11	1.23E-14	1.10E-10	3.69E-22
⁵³ Co	2.56E-08	2.78E-10	2.01E-07	3.77E-21
⁵⁴ Co	1.44E-07	8.30E-10	1.51E-07	7.91E-19
⁵⁵ Co	4.07E-04	2.53E-04	8.06E-04	6.61E-08
⁵⁶ Co	3.50E-06	2.14E-06	6.42E-06	4.51E-08
⁵⁷ Co	5.41E-06	3.47E-06	1.24E-05	7.63E-07
⁵⁸ Co	1.47E-08	8.53E-09	3.51E-08	2.13E-09
⁵⁹ Co	6.74E-09	3.56E-09	1.61E-08	8.96E-10
⁶⁰ Co	2.49E-13	7.04E-14	4.20E-13	1.36E-14
⁶¹ Co	4.23E-14	2.60E-14	8.32E-14	1.28E-16
⁶² Co	4.72E-14	1.98E-14	5.34E-14	4.44E-19
⁵⁴ Ni	8.71E-11	7.49E-13	4.70E-10	9.41E-22
⁵⁵ Ni	2.49E-08	9.53E-12	6.44E-08	9.03E-22
⁵⁶ Ni	1.07E-01	8.11E-02	2.40E-01	6.28E-08
⁵⁷ Ni	3.25E-03	1.45E-03	7.68E-03	6.90E-08
⁵⁸ Ni	4.03E-03	6.76E-04	8.16E-03	9.57E-06
⁵⁹ Ni	8.91E-06	9.86E-06	1.91E-05	1.47E-07
⁶⁰ Ni	5.12E-06	4.84E-06	1.16E-05	6.62E-07
⁶¹ Ni	1.41E-09	1.46E-09	3.00E-09	1.55E-10
⁶² Ni	7.67E-10	2.65E-10	1.55E-09	6.54E-11
⁶³ Ni	1.23E-13	3.63E-14	1.20E-13	1.11E-16
⁶⁴ Ni	1.33E-13	2.69E-15	2.43E-13	3.87E-17
⁵⁷ Cu	3.42E-09	1.35E-09	2.17E-08	1.14E-21
⁵⁸ Cu	3.21E-04	4.54E-05	1.63E-03	8.73E-21
⁵⁹ Cu	3.18E-04	1.51E-04	1.07E-03	7.61E-15
⁶⁰ Cu	5.58E-05	5.80E-05	1.16E-04	1.50E-13
⁶¹ Cu	2.63E-06	1.15E-06	3.59E-06	1.47E-11
⁶² Cu	8.32E-08	2.29E-09	1.26E-07	3.65E-13
⁶³ Cu	1.02E-09	8.78E-10	1.69E-09	1.48E-12
⁶⁴ Cu	1.21E-13	5.43E-14	1.55E-13	1.63E-16
⁶⁵ Cu	1.78E-13	1.63E-14	3.65E-13	7.10E-17
⁶⁶ Cu	1.31E-13	4.11E-15	1.63E-13	1.43E-18
⁵⁹ Zn	1.56E-06	1.64E-10	2.02E-05	3.11E-21
⁶⁰ Zn	3.88E-03	1.59E-03	1.43E-02	3.12E-18
⁶¹ Zn	1.01E-04	1.97E-05	2.21E-04	6.29E-17
⁶² Zn	6.17E-04	1.61E-05	1.28E-03	6.70E-13
⁶³ Zn	1.12E-06	4.42E-07	3.44E-06	3.83E-14
⁶⁴ Zn	5.52E-08	2.76E-07	8.44E-08	2.45E-12
⁶⁵ Zn	2.46E-10	8.76E-10	3.07E-10	1.51E-15
⁶⁶ Zn	1.73E-12	3.55E-13	2.39E-12	4.99E-15
⁶⁷ Zn	2.26E-13	8.63E-15	1.65E-13	2.10E-18
⁶⁸ Zn	1.94E-13	1.59E-14	2.10E-13	7.33E-17
⁶¹ Ga	4.32E-10	2.26E-10	3.58E-09	5.33E-22
⁶² Ga	6.46E-09	1.53E-10	1.19E-07	1.75E-21
⁶³ Ga	1.08E-05	2.98E-06	6.75E-05	9.03E-21
⁶⁴ Ga	7.28E-06	6.62E-06	1.53E-05	1.13E-20
⁶⁵ Ga	1.75E-07	1.28E-07	3.23E-07	2.98E-19
⁶⁶ Ga	6.12E-09	6.24E-10	1.02E-08	1.72E-19
⁶⁷ Ga	1.07E-10	4.37E-12	3.67E-10	3.95E-18
⁶⁸ Ga	4.09E-13	6.65E-15	4.36E-13	1.17E-18
⁶⁹ Ga	5.21E-13	2.22E-13	8.39E-13	4.02E-17
⁶³ Ge	6.28E-09	6.93E-13	1.08E-07	2.62E-21
⁶⁴ Ge	2.50E-04	8.76E-05	8.32E-04	5.59E-20
⁶⁵ Ge	2.54E-06	7.76E-07	7.57E-06	6.17E-20
⁶⁶ Ge	1.47E-05	1.05E-06	3.51E-05	2.77E-19
⁶⁷ Ge	4.43E-08	1.13E-09	2.59E-07	3.77E-19
⁶⁸ Ge	1.71E-08	4.68E-10	1.65E-07	9.06E-18
⁶⁹ Ge	1.20E-10	2.05E-11	6.89E-10	1.67E-18
⁷⁰ Ge	2.21E-10	4.15E-11	9.91E-10	2.36E-16
⁷¹ Ge	3.96E-11	1.06E-11	1.98E-10	7.12E-18

Species $M(^{56}\text{Ni})$	40SHa 5.4E-01	40SHb 9.0E-02	40SLa 4.4E-01	40SLb 1.1E-01
⁴ He	2.01E+00	1.79E+00	1.90E+00	1.80E+00
⁶ Li	2.10E-20	2.10E-20	1.80E-20	1.80E-20
⁷ Li	4.19E-19	4.19E-19	2.22E-19	2.22E-19
⁹ Be	0.00E+00	0.00E+00	0.00E+00	0.00E+00
¹⁰ B	9.84E-22	9.84E-22	7.15E-22	7.15E-22
¹¹ B	4.79E-14	4.79E-14	3.73E-14	3.73E-14
¹² C	1.46E-01	1.46E-01	1.51E-01	1.51E-01
¹³ C	1.83E-08	1.83E-08	1.53E-08	1.53E-08
¹⁴ C	1.10E-08	1.10E-08	8.43E-09	8.43E-09
¹³ N	1.32E-16	1.32E-16	1.70E-16	1.70E-16
¹⁴ N	8.19E-05	8.19E-05	8.19E-05	8.19E-05
¹⁵ N	1.46E-08	1.46E-08	1.11E-08	1.11E-08
¹⁶ N	9.11E-24	8.35E-24	1.08E-23	1.01E-23
¹⁴ O	1.69E-09	3.65E-14	2.64E-10	9.69E-13
¹⁵ O	2.80E-11	1.80E-11	2.61E-11	2.61E-11
¹⁶ O	8.82E+00	8.82E+00	8.94E+00	8.94E+00
¹⁷ O	1.05E-07	1.05E-07	8.36E-08	8.36E-08
¹⁸ O	3.13E-06	3.13E-06	3.13E-06	3.13E-06
¹⁷ F	2.36E-14	6.93E-21	4.03E-15	6.21E-18
¹⁸ F	3.62E-10	2.80E-10	2.55E-10	2.27E-10
¹⁹ F	5.47E-10	5.46E-10	4.78E-10	4.78E-10
²⁰ F	3.34E-12	3.34E-12	2.41E-12	2.41E-12
²¹ F	9.94E-11	1.97E-13	5.82E-11	3.37E-13
¹⁸ Ne	2.85E-13	3.98E-23	1.81E-14	3.60E-17
¹⁹ Ne	2.19E-11	2.19E-16	6.63E-14	1.97E-16
²⁰ Ne	5.93E-01	5.93E-01	6.43E-01	6.43E-01
²¹ Ne	2.19E-03	2.19E-03	2.36E-03	2.36E-03
²² Ne	5.31E-02	5.31E-02	5.32E-02	5.32E-02
²¹ Na	1.96E-10	4.31E-14	1.32E-13	5.25E-14
²² Na	3.61E-07	3.60E-07	3.07E-07	3.07E-07
²³ Na	2.09E-02	2.09E-02	2.30E-02	2.30E-02
²⁴ Na	7.97E-06	7.97E-06	6.19E-06	6.19E-06
²² Mg	2.73E-09	1.19E-17	8.93E-15	7.32E-18
²³ Mg	4.39E-06	4.39E-06	3.19E-06	3.19E-06
²⁴ Mg	3.42E-01	3.42E-01	3.51E-01	3.51E-01
²⁵ Mg	4.44E-02	4.44E-02	4.76E-02	4.76E-02
²⁶ Mg	9.82E-02	9.82E-02	1.06E-01	1.06E-01
²⁷ Mg	2.42E-06	2.42E-06	1.82E-06	1.82E-06
²⁴ Al	1.77E-13	1.87E-20	3.42E-20	1.49E-20
²⁵ Al	1.07E-06	6.59E-13	3.97E-10	8.81E-13
²⁶ Al	5.70E-05	5.52E-05	5.36E-05	5.35E-05
²⁷ Al	7.41E-02	7.41E-02	7.80E-02	7.80E-02
²⁸ Al	2.03E-04	2.03E-04	1.51E-04	1.51E-04
²⁹ Al	2.14E-06	2.14E-06	1.55E-06	1.55E-06
²⁶ Si	1.87E-06	5.41E-14	1.15E-08	2.61E-14
²⁷ Si	4.05E-06	1.69E-06	1.05E-06	1.02E-06
²⁸ Si	3.99E-01	3.99E-01	4.30E-01	4.30E-01
²⁹ Si	5.34E-02	5.34E-02	5.37E-02	5.37E-02
³⁰ Si	4.92E-02	4.92E-02	4.26E-02	4.26E-02
²⁸ P	1.53E-10	3.04E-21	5.76E-15	8.56E-22
²⁹ P	4.56E-06	1.92E-11	5.17E-07	9.26E-12
³⁰ P	2.48E-05	9.45E-06	1.64E-05	7.91E-06
³¹ P	6.52E-03	6.51E-03	6.07E-03	6.06E-03
³² P	1.84E-05	1.84E-05	1.29E-05	1.29E-05
³³ P	8.45E-06	8.45E-06	5.49E-06	5.49E-06
³⁴ P	3.85E-09	3.85E-09	2.59E-09	2.59E-09
³⁰ S	2.33E-06	1.01E-14	1.21E-07	1.83E-15
³¹ S	6.80E-06	1.28E-07	7.98E-07	6.75E-08
³² S	1.61E-01	1.61E-01	1.80E-01	1.80E-01
³³ S	7.26E-04	7.24E-04	7.40E-04	7.40E-04
³⁴ S	1.14E-02	1.13E-02	1.02E-02	1.01E-02
³⁵ S	1.01E-05	1.01E-05	7.32E-06	7.32E-06
³⁶ S	1.21E-05	1.21E-05	8.53E-06	8.53E-06
³¹ Cl	1.43E-19	0.00E+00	2.19E-22	0.00E+00
³² Cl	1.16E-11	9.66E-25	2.94E-14	2.19E-20
³³ Cl	1.46E-06	1.31E-13	7.36E-09	3.22E-13
³⁴ Cl	2.50E-05	3.19E-08	1.11E-05	1.66E-08
³⁵ Cl	4.03E-04	3.60E-04	5.18E-04	4.77E-04
³⁶ Cl	5.62E-06	5.62E-06	4.01E-06	4.01E-06
³⁷ Cl	1.04E-05	1.04E-05	6.88E-06	6.88E-06
³⁸ Cl	4.07E-10	4.07E-10	3.09E-10	3.09E-10

TABLE 6

Detailed yields (M_{\odot}) before decay of radioactive species: For models 40SH and 40SL.

Species $M(^{56}\text{Ni})$	40SHa	40SHb	40SLa	40SLb
³³ Ar	8.46E-17	5.74E-25	1.37E-22	2.45E-24
³⁴ Ar	2.49E-06	4.58E-16	1.43E-07	7.39E-16
³⁵ Ar	1.21E-05	3.99E-09	2.35E-06	1.30E-09
³⁶ Ar	2.63E-02	2.58E-02	2.88E-02	2.86E-02
³⁷ Ar	3.26E-05	3.22E-05	8.58E-05	8.58E-05
³⁸ Ar	4.04E-03	4.03E-03	8.21E-03	8.20E-03
³⁹ Ar	4.14E-08	4.14E-08	3.12E-08	3.12E-08
⁴⁰ Ar	1.43E-07	1.43E-07	9.83E-08	9.83E-08
⁴¹ Ar	3.81E-11	3.81E-11	2.83E-11	2.83E-11
³⁵ K	4.79E-21	0.00E+00	9.40E-24	0.00E+00
³⁶ K	1.36E-11	2.81E-24	1.03E-14	1.08E-19
³⁷ K	4.23E-08	8.28E-17	1.47E-10	3.08E-14
³⁸ K	6.68E-06	3.19E-08	5.66E-06	2.50E-08
³⁹ K	2.22E-04	1.87E-04	4.21E-04	3.99E-04
⁴⁰ K	5.51E-08	5.49E-08	6.95E-08	6.94E-08
⁴¹ K	6.60E-08	6.60E-08	4.92E-08	4.92E-08
⁴² K	1.67E-09	1.67E-09	1.22E-09	1.22E-09
⁴³ K	2.83E-10	2.83E-10	2.05E-10	2.05E-10
³⁷ Ca	2.58E-15	1.23E-24	1.54E-21	3.60E-24
³⁸ Ca	1.63E-08	1.05E-19	1.76E-10	3.68E-18
³⁹ Ca	7.45E-07	1.10E-10	6.11E-08	8.40E-11
⁴⁰ Ca	2.24E-02	2.14E-02	2.21E-02	2.18E-02
⁴¹ Ca	8.65E-06	7.40E-06	2.27E-05	2.24E-05
⁴² Ca	6.49E-05	6.33E-05	2.16E-04	2.16E-04
⁴³ Ca	8.56E-08	8.49E-08	1.57E-07	1.57E-07
⁴⁴ Ca	8.86E-08	8.86E-08	4.52E-08	4.52E-08
⁴⁵ Ca	1.79E-10	1.79E-10	9.39E-11	9.39E-11
⁴⁶ Ca	2.10E-10	2.09E-10	1.07E-10	1.07E-10
⁴⁰ Sc	3.42E-19	0.00E+00	1.60E-21	3.19E-25
⁴¹ Sc	2.14E-12	1.64E-21	7.79E-14	3.08E-17
⁴² Sc	3.85E-09	2.27E-14	6.75E-11	1.41E-12
⁴³ Sc	3.76E-06	2.40E-09	9.87E-07	1.67E-08
⁴⁴ Sc	3.74E-09	2.63E-09	8.42E-09	8.14E-09
⁴⁵ Sc	2.38E-08	2.31E-08	4.66E-08	4.64E-08
⁴⁶ Sc	8.80E-10	8.80E-10	4.24E-10	4.24E-10
⁴⁷ Sc	2.57E-10	2.57E-10	1.31E-10	1.31E-10
⁴⁸ Sc	8.10E-12	8.03E-12	4.93E-12	4.91E-12
⁴⁹ Sc	3.44E-13	3.08E-13	2.02E-13	1.90E-13
⁴² Ti	3.85E-15	7.70E-25	6.45E-19	5.80E-24
⁴³ Ti	4.49E-09	8.41E-18	2.88E-11	3.61E-13
⁴⁴ Ti	1.18E-03	6.67E-06	6.52E-04	8.72E-06
⁴⁵ Ti	6.06E-07	2.22E-07	4.86E-07	4.54E-07
⁴⁶ Ti	2.77E-05	2.20E-05	8.62E-05	8.05E-05
⁴⁷ Ti	5.44E-07	4.50E-07	1.60E-06	1.44E-06
⁴⁸ Ti	2.48E-07	2.48E-07	4.35E-07	4.35E-07
⁴⁹ Ti	1.12E-09	1.12E-09	5.35E-10	5.35E-10
⁵⁰ Ti	8.35E-10	8.35E-10	2.04E-10	2.04E-10
⁵¹ Ti	1.50E-13	6.83E-16	4.14E-14	1.76E-15
⁴⁴ V	1.53E-15	8.33E-25	2.20E-19	4.22E-22
⁴⁵ V	1.20E-08	3.13E-21	2.65E-11	7.69E-15
⁴⁶ V	2.12E-08	2.15E-13	2.70E-10	3.45E-14
⁴⁷ V	5.26E-05	1.35E-07	4.98E-05	1.81E-07
⁴⁸ V	8.85E-08	6.07E-08	2.11E-07	1.96E-07
⁴⁹ V	1.97E-07	1.76E-07	4.17E-07	4.14E-07
⁵⁰ V	2.30E-09	2.30E-09	3.98E-09	3.98E-09
⁵¹ V	1.69E-08	1.69E-08	3.09E-08	3.09E-08
⁵² V	5.33E-13	4.07E-13	2.75E-13	2.38E-13
⁵³ V	1.60E-13	1.03E-15	3.29E-14	7.27E-16
⁴⁶ Cr	5.24E-11	9.59E-25	3.54E-14	3.28E-20
⁴⁷ Cr	4.53E-07	2.43E-14	1.98E-08	2.40E-11
⁴⁸ Cr	1.61E-03	2.73E-04	9.50E-04	2.09E-04
⁴⁹ Cr	4.51E-05	2.61E-05	2.15E-05	2.02E-05
⁵⁰ Cr	3.63E-04	3.45E-04	4.07E-04	3.99E-04
⁵¹ Cr	3.78E-06	3.70E-06	9.52E-06	9.39E-06
⁵² Cr	4.00E-05	4.00E-05	9.05E-05	9.05E-05
⁵³ Cr	5.55E-09	5.55E-09	1.67E-08	1.67E-08
⁵⁴ Cr	1.53E-10	1.52E-10	3.96E-10	3.96E-10
⁵⁵ Cr	8.15E-14	1.60E-17	2.50E-14	1.17E-15
⁴⁸ Mn	1.43E-15	5.54E-25	5.02E-18	1.01E-21
⁴⁹ Mn	9.52E-08	4.47E-18	2.43E-11	3.56E-15
⁵⁰ Mn	6.98E-08	3.01E-11	4.47E-10	1.98E-12

Species $M(^{56}\text{Ni})$	40SHa	40SHb	40SLa	40SLb
^{51}Mn	1.12E-04	4.74E-05	9.66E-05	3.73E-05
^{52}Mn	2.04E-06	1.71E-06	2.34E-06	2.12E-06
^{53}Mn	3.07E-05	3.01E-05	4.82E-05	4.82E-05
^{54}Mn	8.85E-08	8.84E-08	2.10E-07	2.10E-07
^{55}Mn	2.19E-08	2.19E-08	6.95E-08	6.95E-08
^{56}Mn	2.54E-13	6.02E-14	2.38E-13	1.70E-13
^{57}Mn	1.66E-13	1.79E-16	3.15E-14	4.14E-15
^{50}Fe	2.02E-14	1.29E-25	2.50E-20	4.69E-24
^{51}Fe	8.79E-10	4.06E-16	8.58E-13	1.11E-15
^{52}Fe	7.22E-03	4.58E-03	5.22E-03	3.72E-03
^{53}Fe	6.26E-04	5.51E-04	4.41E-04	4.40E-04
^{54}Fe	3.19E-02	2.99E-02	2.75E-02	2.75E-02
^{55}Fe	1.25E-04	1.24E-04	1.99E-04	1.99E-04
^{56}Fe	2.88E-04	2.88E-04	5.93E-04	5.93E-04
^{57}Fe	1.83E-08	1.83E-08	5.63E-08	5.63E-08
^{58}Fe	7.38E-10	7.38E-10	2.95E-09	2.95E-09
^{59}Fe	1.57E-13	1.91E-16	2.15E-14	1.22E-15
^{60}Fe	1.72E-13	1.19E-16	4.06E-14	6.14E-16
^{52}Co	5.34E-19	2.91E-26	4.17E-23	1.00E-24
^{53}Co	5.34E-11	2.23E-20	7.71E-14	2.09E-17
^{54}Co	2.86E-09	9.59E-11	3.55E-11	5.59E-12
^{55}Co	2.53E-03	2.09E-03	1.77E-03	1.76E-03
^{56}Co	2.30E-05	1.12E-05	1.45E-05	1.11E-05
^{57}Co	1.69E-05	1.44E-05	2.35E-05	2.27E-05
^{58}Co	2.65E-08	2.63E-08	5.65E-08	5.65E-08
^{59}Co	7.84E-09	7.82E-09	2.52E-08	2.52E-08
^{60}Co	5.14E-13	8.36E-14	4.37E-13	3.05E-13
^{61}Co	2.95E-13	8.52E-16	5.55E-14	5.31E-15
^{62}Co	1.81E-13	1.23E-18	3.35E-14	6.58E-16
^{54}Ni	2.02E-17	2.22E-24	6.98E-23	6.29E-24
^{55}Ni	1.63E-12	2.57E-17	6.60E-16	1.44E-17
^{56}Ni	5.44E-01	9.01E-02	4.38E-01	1.09E-01
^{57}Ni	1.81E-02	1.39E-03	1.18E-02	2.16E-03
^{58}Ni	2.30E-02	2.40E-03	1.30E-02	3.85E-03
^{59}Ni	5.98E-05	3.16E-06	6.87E-05	6.37E-06
^{60}Ni	1.72E-05	8.61E-06	3.52E-05	1.95E-05
^{61}Ni	5.10E-09	1.18E-09	9.04E-09	4.23E-09
^{62}Ni	3.54E-09	3.83E-10	3.83E-09	1.88E-09
^{63}Ni	3.73E-13	6.10E-16	1.06E-13	9.14E-15
^{64}Ni	6.64E-13	2.81E-16	2.09E-13	1.96E-15
^{57}Cu	7.68E-13	3.46E-23	1.75E-14	1.97E-16
^{58}Cu	4.26E-04	1.66E-13	9.85E-05	3.51E-09
^{59}Cu	1.18E-03	1.25E-09	7.83E-04	1.80E-05
^{60}Cu	4.50E-04	2.51E-10	5.35E-04	1.52E-05
^{61}Cu	2.50E-05	5.42E-10	2.15E-05	1.01E-06
^{62}Cu	7.24E-07	3.64E-12	3.62E-07	2.28E-08
^{63}Cu	8.94E-09	1.06E-11	9.37E-09	1.68E-10
^{64}Cu	3.80E-13	9.19E-16	1.24E-13	5.34E-15
^{65}Cu	6.51E-13	5.46E-16	2.17E-13	8.65E-15
^{66}Cu	5.10E-13	4.60E-18	2.46E-13	6.23E-15
^{59}Zn	1.06E-09	1.47E-24	3.24E-13	1.93E-19
^{60}Zn	1.77E-02	6.46E-11	1.33E-02	3.74E-04
^{61}Zn	6.20E-04	1.41E-11	3.41E-04	1.61E-05
^{62}Zn	3.97E-03	6.73E-10	1.79E-03	1.38E-04
^{63}Zn	7.64E-06	8.11E-13	6.27E-06	5.68E-08
^{64}Zn	8.94E-07	2.71E-11	2.08E-06	1.97E-09
^{65}Zn	3.55E-09	1.08E-14	8.26E-09	2.19E-11
^{66}Zn	1.01E-11	3.75E-14	4.95E-12	2.06E-13
^{67}Zn	2.70E-13	2.92E-17	1.24E-13	3.40E-15
^{68}Zn	6.77E-13	7.24E-16	1.59E-13	3.35E-15
^{61}Ga	4.08E-14	0.00E+00	2.72E-15	1.31E-17
^{62}Ga	2.99E-13	7.36E-24	1.21E-14	9.00E-17
^{63}Ga	4.36E-05	1.49E-18	2.73E-05	1.69E-08
^{64}Ga	8.07E-05	2.32E-18	1.11E-04	5.97E-08
^{65}Ga	1.81E-06	2.36E-17	2.54E-06	6.52E-09
^{66}Ga	5.59E-08	1.24E-17	4.07E-08	7.18E-10
^{67}Ga	7.77E-10	8.33E-16	3.94E-10	3.36E-12
^{68}Ga	9.03E-13	9.08E-17	2.38E-13	1.53E-14
^{69}Ga	1.52E-12	4.68E-16	3.44E-13	1.15E-14
^{63}Ge	3.12E-12	8.50E-26	5.89E-16	1.55E-22
^{64}Ge	1.55E-03	9.12E-19	1.25E-03	6.44E-07
^{65}Ge	1.60E-05	1.65E-18	1.30E-05	3.27E-08
^{66}Ge	9.80E-05	1.04E-16	5.60E-05	1.09E-06
^{67}Ge	2.20E-07	2.22E-16	7.60E-08	6.90E-10
^{68}Ge	7.06E-08	2.77E-14	3.05E-08	4.51E-10
^{69}Ge	5.38E-10	6.51E-16	4.77E-10	2.79E-12
^{70}Ge	7.95E-10	8.72E-14	7.34E-10	2.49E-12
^{71}Ge	1.74E-10	7.65E-17	1.75E-10	2.84E-13

Species $M(^{56}\text{Ni})$	25A 7.8E-02	25B 1.5E-01	25Sa 1.6E-01	25Sb 9.1E-02
⁴ He	1.82E+00	1.80E+00	1.82E+00	1.79E+00
⁶ Li	3.23E-14	2.88E-20	2.12E-20	2.12E-20
⁷ Li	3.13E-19	7.26E-20	9.73E-20	9.73E-20
⁹ Be	9.86E-16	0.00E+00	0.00E+00	0.00E+00
¹⁰ B	2.97E-15	6.92E-22	4.37E-22	4.37E-22
¹¹ B	1.23E-14	4.92E-15	5.11E-15	5.11E-15
¹² C	1.35E-01	1.38E-01	1.41E-01	1.41E-01
¹³ C	1.56E-07	2.13E-09	2.22E-09	2.22E-09
¹⁴ C	1.93E-07	8.44E-10	8.78E-10	8.78E-10
¹³ N	3.78E-15	2.65E-16	1.41E-16	1.41E-16
¹⁴ N	1.02E-03	1.02E-03	9.57E-04	9.57E-04
¹⁵ N	1.39E-08	1.86E-09	2.03E-09	2.03E-09
¹⁶ N	1.69E-11	1.04E-22	8.16E-23	8.14E-23
¹⁴ O	8.58E-08	6.99E-10	1.70E-10	5.47E-11
¹⁵ O	1.15E-10	1.35E-11	1.43E-11	1.43E-11
¹⁶ O	2.66E+00	2.86E+00	2.91E+00	2.91E+00
¹⁷ O	3.00E-08	1.62E-08	1.77E-08	1.77E-08
¹⁸ O	6.07E-03	6.11E-03	6.13E-03	6.13E-03
¹⁷ F	4.52E-13	7.55E-15	3.17E-15	9.26E-16
¹⁸ F	2.49E-10	1.35E-10	1.59E-10	1.50E-10
¹⁹ F	2.76E-09	2.50E-10	2.81E-10	2.81E-10
²⁰ F	3.72E-09	4.48E-13	5.28E-13	5.28E-13
²¹ F	4.74E-09	9.35E-12	4.33E-11	1.31E-11
¹⁸ Ne	9.84E-13	3.50E-14	1.67E-14	3.88E-15
¹⁹ Ne	2.53E-11	1.48E-12	2.15E-13	5.82E-15
²⁰ Ne	5.44E-01	6.02E-01	6.03E-01	6.03E-01
²¹ Ne	2.92E-03	3.20E-03	3.19E-03	3.19E-03
²² Ne	3.09E-02	3.11E-02	3.13E-02	3.13E-02
²¹ Na	6.18E-09	3.20E-11	7.00E-13	8.10E-14
²² Na	3.11E-07	2.55E-07	2.92E-07	2.92E-07
²³ Na	1.66E-02	1.82E-02	1.82E-02	1.82E-02
²⁴ Na	8.06E-07	4.80E-07	5.42E-07	5.42E-07
²² Mg	5.24E-08	2.59E-11	1.05E-11	2.69E-14
²³ Mg	1.29E-06	1.15E-06	1.46E-06	1.46E-06
²⁴ Mg	1.47E-01	1.60E-01	1.63E-01	1.63E-01
²⁵ Mg	3.58E-02	3.95E-02	3.97E-02	3.97E-02
²⁶ Mg	1.79E-02	1.98E-02	1.99E-02	1.99E-02
²⁷ Mg	3.55E-06	7.67E-08	8.83E-08	8.83E-08
²⁴ Al	1.80E-09	1.21E-13	1.12E-17	1.94E-20
²⁵ Al	1.22E-07	1.97E-08	2.26E-08	1.76E-10
²⁶ Al	1.10E-02	1.23E-02	1.22E-02	1.22E-02
²⁷ Al	1.71E-02	1.87E-02	1.89E-02	1.89E-02
²⁸ Al	2.30E-05	1.71E-05	2.08E-05	2.08E-05
²⁹ Al	1.32E-07	8.85E-08	1.08E-07	1.08E-07
²⁶ Si	1.29E-06	3.28E-08	9.74E-08	3.21E-09
²⁷ Si	2.16E-05	1.63E-05	1.90E-05	1.89E-05
²⁸ Si	6.44E-02	7.25E-02	7.95E-02	7.95E-02
²⁹ Si	5.78E-03	6.13E-03	6.30E-03	6.30E-03
³⁰ Si	4.58E-03	4.38E-03	4.82E-03	4.82E-03
²⁸ P	5.10E-08	2.60E-11	1.86E-13	1.26E-15
²⁹ P	1.06E-06	1.79E-07	9.41E-07	5.25E-08
³⁰ P	5.33E-06	4.92E-06	9.17E-06	4.47E-06
³¹ P	5.48E-04	5.11E-04	5.69E-04	5.68E-04
³² P	9.43E-07	7.36E-07	9.20E-07	9.20E-07
³³ P	5.91E-07	4.80E-07	6.10E-07	6.10E-07
³⁴ P	1.84E-10	1.17E-10	1.46E-10	1.46E-10
³⁰ S	3.67E-06	3.70E-07	8.11E-07	9.27E-08
³¹ S	2.23E-06	3.74E-07	9.15E-07	1.22E-07
³² S	2.12E-02	2.59E-02	2.91E-02	2.91E-02
³³ S	1.51E-04	1.21E-04	1.59E-04	1.58E-04
³⁴ S	1.53E-03	1.08E-03	1.46E-03	1.45E-03
³⁵ S	5.80E-07	4.54E-07	5.61E-07	5.61E-07
³⁶ S	5.23E-07	4.22E-07	5.42E-07	5.42E-07
³¹ Cl	4.18E-15	7.35E-19	7.06E-21	3.89E-22
³² Cl	3.26E-08	2.18E-11	1.70E-13	6.83E-15
³³ Cl	8.20E-07	3.09E-08	8.88E-08	2.07E-09
³⁴ Cl	2.85E-06	3.04E-06	1.11E-05	1.46E-06
³⁵ Cl	5.38E-05	4.32E-05	6.18E-05	5.46E-05
³⁶ Cl	9.30E-07	7.62E-07	9.80E-07	9.80E-07
³⁷ Cl	1.12E-06	9.24E-07	1.20E-06	1.20E-06
³⁸ Cl	2.97E-11	2.21E-11	2.67E-11	2.67E-11

TABLE 7

Detailed yields (M_{\odot}) before decay of radioactive species: For models 25A, 25B and 25S.

Species	25A	25B	25Sa	25Sb
$M(^{56}\text{Ni})$	7.8E-02	1.5E-01	1.6E-01	9.1E-02
³³ Ar	6.61E-11	2.24E-15	2.95E-17	9.83E-18
³⁴ Ar	4.90E-06	7.80E-07	1.59E-06	2.74E-07
³⁵ Ar	3.85E-06	1.18E-06	3.00E-06	4.45E-07
³⁶ Ar	3.48E-03	4.31E-03	4.80E-03	4.76E-03
³⁷ Ar	9.18E-06	6.52E-06	9.35E-06	9.34E-06
³⁸ Ar	4.61E-04	3.15E-04	4.83E-04	4.83E-04
³⁹ Ar	4.44E-09	3.18E-09	3.98E-09	3.98E-09
⁴⁰ Ar	5.89E-09	4.61E-09	5.87E-09	5.87E-09
⁴¹ Ar	1.48E-12	1.05E-12	1.28E-12	1.28E-12
³⁵ K	3.82E-16	4.11E-20	5.22E-22	4.89E-23
³⁶ K	1.10E-08	7.30E-12	2.06E-13	1.36E-14
³⁷ K	2.96E-06	1.91E-09	5.77E-10	2.97E-11
³⁸ K	2.00E-06	1.53E-06	4.50E-06	7.21E-07
³⁹ K	2.73E-05	1.93E-05	3.24E-05	2.80E-05
⁴⁰ K	1.42E-08	1.12E-08	1.41E-08	1.41E-08
⁴¹ K	4.76E-09	3.74E-09	4.86E-09	4.86E-09
⁴² K	4.93E-11	3.83E-11	4.75E-11	4.75E-11
⁴³ K	2.44E-12	1.81E-12	2.26E-12	2.26E-12
³⁷ Ca	4.34E-10	1.13E-14	6.04E-16	1.61E-16
³⁸ Ca	9.79E-07	3.73E-08	4.04E-08	1.00E-08
³⁹ Ca	1.41E-06	2.78E-07	4.75E-07	1.30E-07
⁴⁰ Ca	2.86E-03	3.65E-03	4.21E-03	4.14E-03
⁴¹ Ca	1.95E-06	1.41E-06	2.06E-06	2.06E-06
⁴² Ca	1.17E-05	8.23E-06	1.23E-05	1.23E-05
⁴³ Ca	1.41E-08	9.17E-09	1.31E-08	1.31E-08
⁴⁴ Ca	1.01E-08	6.18E-09	8.17E-09	8.17E-09
⁴⁵ Ca	1.37E-11	9.53E-12	1.15E-11	1.15E-11
⁴⁶ Ca	1.11E-11	8.37E-12	1.08E-11	1.08E-11
⁴⁰ Sc	4.81E-14	8.25E-18	5.68E-20	1.04E-20
⁴¹ Sc	9.37E-09	2.77E-12	1.02E-13	1.35E-14
⁴² Sc	8.19E-09	1.58E-10	1.93E-09	1.83E-09
⁴³ Sc	5.20E-07	7.88E-08	7.61E-07	4.28E-07
⁴⁴ Sc	6.76E-10	4.33E-10	6.29E-10	6.27E-10
⁴⁵ Sc	4.36E-09	2.68E-09	3.72E-09	3.72E-09
⁴⁶ Sc	1.20E-10	8.91E-11	1.09E-10	1.09E-10
⁴⁷ Sc	1.78E-11	1.22E-11	1.62E-11	1.62E-11
⁴⁸ Sc	2.59E-13	1.85E-13	2.49E-13	2.49E-13
⁴⁹ Sc	1.20E-14	3.07E-15	7.62E-15	7.55E-15
⁴² Ti	1.37E-10	2.13E-13	8.40E-14	2.63E-14
⁴³ Ti	1.99E-07	1.89E-09	8.55E-09	6.03E-09
⁴⁴ Ti	1.31E-04	3.66E-05	2.14E-04	5.73E-05
⁴⁵ Ti	9.27E-07	4.74E-08	6.86E-08	5.90E-08
⁴⁶ Ti	6.71E-06	6.51E-06	1.30E-05	6.25E-06
⁴⁷ Ti	8.05E-08	5.70E-08	1.00E-07	7.70E-08
⁴⁸ Ti	3.83E-08	1.89E-08	2.95E-08	2.95E-08
⁴⁹ Ti	1.56E-10	7.49E-11	9.95E-11	9.95E-11
⁵⁰ Ti	1.04E-10	4.35E-11	5.60E-11	5.60E-11
⁵¹ Ti	9.44E-15	7.56E-16	2.24E-14	2.23E-14
⁴⁴ V	1.37E-09	1.30E-14	4.31E-16	2.33E-16
⁴⁵ V	1.72E-06	7.83E-10	1.99E-10	1.18E-11
⁴⁶ V	1.00E-06	1.43E-07	1.46E-07	4.17E-08
⁴⁷ V	5.93E-06	8.78E-06	2.42E-05	5.87E-06
⁴⁸ V	1.36E-08	9.87E-09	1.51E-08	1.39E-08
⁴⁹ V	2.72E-08	2.02E-08	2.78E-08	2.67E-08
⁵⁰ V	4.00E-10	1.98E-10	2.96E-10	2.96E-10
⁵¹ V	2.58E-09	1.25E-09	2.01E-09	2.01E-09
⁵² V	8.62E-14	2.90E-14	6.25E-14	6.20E-14
⁵³ V	2.47E-14	1.07E-15	8.54E-15	8.40E-15
⁴⁶ Cr	3.21E-07	2.71E-09	1.37E-09	4.70E-10
⁴⁷ Cr	2.43E-06	5.81E-07	7.85E-07	2.53E-07
⁴⁸ Cr	1.72E-04	9.11E-05	2.90E-04	1.28E-04
⁴⁹ Cr	7.54E-06	4.52E-06	5.58E-06	4.55E-06
⁵⁰ Cr	2.91E-05	3.77E-05	4.83E-05	3.89E-05
⁵¹ Cr	5.67E-07	3.65E-07	6.00E-07	5.68E-07
⁵² Cr	4.66E-06	2.43E-06	4.23E-06	4.23E-06
⁵³ Cr	1.08E-09	4.56E-10	7.57E-10	7.57E-10
⁵⁴ Cr	3.17E-11	1.17E-11	2.00E-11	2.00E-11
⁵⁵ Cr	2.65E-14	7.28E-16	6.21E-15	5.69E-15
⁴⁸ Mn	6.69E-10	1.13E-13	9.01E-16	2.00E-16
⁴⁹ Mn	3.18E-06	4.08E-09	6.51E-09	4.09E-10
⁵⁰ Mn	2.04E-06	1.08E-07	1.35E-07	3.19E-08

Species	25A	25B	25Sa	25Sb
$M(^{56}\text{Ni})$	7.8E-02	1.5E-01	1.6E-01	9.1E-02
⁵¹ Mn	1.84E-05	2.06E-05	4.96E-05	1.47E-05
⁵² Mn	2.10E-07	2.29E-07	2.72E-07	2.50E-07
⁵³ Mn	3.25E-06	2.08E-06	3.38E-06	3.38E-06
⁵⁴ Mn	1.46E-08	6.83E-09	1.13E-08	1.13E-08
⁵⁵ Mn	4.18E-09	1.85E-09	3.06E-09	3.06E-09
⁵⁶ Mn	4.69E-14	6.82E-15	4.16E-14	4.06E-14
⁵⁷ Mn	2.62E-14	2.44E-15	1.94E-14	1.83E-14
⁵⁰ Fe	5.01E-08	5.01E-13	5.95E-14	2.45E-14
⁵¹ Fe	1.14E-06	1.51E-08	1.00E-08	3.51E-09
⁵² Fe	6.63E-04	1.02E-03	1.56E-03	1.23E-03
⁵³ Fe	4.75E-05	9.05E-05	1.01E-04	1.01E-04
⁵⁴ Fe	1.67E-03	2.86E-03	3.09E-03	3.09E-03
⁵⁵ Fe	1.31E-05	7.84E-06	1.38E-05	1.38E-05
⁵⁶ Fe	3.25E-05	1.74E-05	3.09E-05	3.09E-05
⁵⁷ Fe	3.74E-09	1.63E-09	2.64E-09	2.64E-09
⁵⁸ Fe	1.62E-10	6.69E-11	1.10E-10	1.10E-10
⁵⁹ Fe	4.74E-14	1.46E-15	2.08E-14	2.03E-14
⁶⁰ Fe	4.30E-14	1.04E-15	3.69E-14	3.59E-14
⁵² Co	4.17E-11	3.93E-16	1.16E-18	2.92E-19
⁵³ Co	5.02E-08	1.68E-11	2.34E-12	2.93E-13
⁵⁴ Co	1.44E-07	6.91E-09	4.65E-09	2.54E-09
⁵⁵ Co	2.19E-04	3.28E-04	3.55E-04	3.53E-04
⁵⁶ Co	1.87E-06	1.76E-06	2.26E-06	2.16E-06
⁵⁷ Co	1.93E-06	1.02E-06	1.88E-06	1.85E-06
⁵⁸ Co	4.76E-09	2.16E-09	3.60E-09	3.60E-09
⁵⁹ Co	1.62E-09	7.18E-10	1.16E-09	1.16E-09
⁶⁰ Co	1.70E-13	1.26E-14	9.36E-14	8.97E-14
⁶¹ Co	3.59E-14	3.54E-15	2.04E-14	1.91E-14
⁶² Co	2.71E-14	1.40E-15	2.94E-14	2.80E-14
⁵⁴ Ni	5.94E-10	1.23E-14	1.13E-15	4.92E-16
⁵⁵ Ni	8.38E-08	1.64E-09	5.75E-11	4.22E-11
⁵⁶ Ni	7.81E-02	1.51E-01	1.64E-01	9.07E-02
⁵⁷ Ni	2.12E-03	2.65E-03	4.18E-03	2.55E-03
⁵⁸ Ni	1.02E-03	1.34E-03	2.64E-03	2.03E-03
⁵⁹ Ni	4.86E-06	1.14E-05	1.98E-05	3.41E-06
⁶⁰ Ni	1.56E-06	1.39E-06	2.42E-06	1.43E-06
⁶¹ Ni	4.16E-10	3.09E-10	6.11E-10	3.85E-10
⁶² Ni	1.22E-10	5.17E-11	1.54E-10	1.45E-10
⁶³ Ni	6.60E-14	5.42E-15	8.24E-14	7.96E-14
⁶⁴ Ni	1.26E-13	6.46E-15	1.10E-13	1.08E-13
⁵⁷ Cu	5.55E-09	1.16E-11	7.90E-14	2.28E-14
⁵⁸ Cu	4.76E-04	2.68E-04	2.62E-04	3.95E-05
⁵⁹ Cu	3.28E-04	4.24E-04	5.30E-04	9.93E-05
⁶⁰ Cu	3.35E-05	5.87E-05	1.02E-04	3.68E-05
⁶¹ Cu	1.10E-06	1.61E-06	4.08E-06	2.13E-06
⁶² Cu	2.05E-08	6.80E-09	3.96E-08	3.60E-08
⁶³ Cu	2.55E-10	3.49E-10	8.96E-10	2.19E-10
⁶⁴ Cu	8.41E-14	7.08E-15	6.81E-14	6.21E-14
⁶⁵ Cu	1.34E-13	9.24E-15	8.84E-14	7.90E-14
⁶⁶ Cu	1.07E-13	6.47E-15	4.94E-14	4.37E-14
⁵⁹ Zn	1.35E-05	1.02E-07	1.44E-08	4.68E-09
⁶⁰ Zn	3.92E-03	3.88E-03	5.58E-03	2.27E-03
⁶¹ Zn	7.98E-05	6.88E-05	1.54E-04	8.82E-05
⁶² Zn	2.48E-04	1.06E-04	4.43E-04	3.98E-04
⁶³ Zn	5.78E-07	5.74E-07	1.34E-06	2.87E-07
⁶⁴ Zn	4.09E-08	8.44E-08	1.97E-07	1.78E-08
⁶⁵ Zn	1.21E-10	1.91E-10	4.54E-10	8.08E-11
⁶⁶ Zn	9.59E-13	9.30E-14	5.44E-13	3.51E-13
⁶⁷ Zn	9.10E-14	7.26E-15	3.65E-14	2.82E-14
⁶⁸ Zn	1.48E-13	8.59E-15	6.75E-14	5.87E-14
⁶¹ Ga	8.45E-10	7.36E-13	4.89E-15	1.25E-15
⁶² Ga	1.57E-07	1.31E-10	1.43E-12	6.52E-13
⁶³ Ga	1.73E-05	8.70E-06	1.39E-05	2.04E-06
⁶⁴ Ga	4.98E-06	7.73E-06	2.14E-05	2.37E-06
⁶⁵ Ga	7.82E-08	1.10E-07	2.99E-07	6.40E-08
⁶⁶ Ga	2.07E-09	1.18E-09	5.89E-09	2.79E-09
⁶⁷ Ga	2.97E-11	5.36E-12	4.53E-11	2.04E-11
⁶⁸ Ga	2.62E-13	1.65E-14	1.55E-13	1.37E-13
⁶⁹ Ga	6.28E-13	1.84E-14	2.08E-13	1.80E-13
⁶³ Ge	1.31E-07	4.83E-10	8.30E-11	2.69E-11
⁶⁴ Ge	2.92E-04	2.27E-04	5.08E-04	7.00E-05
⁶⁵ Ge	2.12E-06	1.57E-06	3.53E-06	8.86E-07
⁶⁶ Ge	9.55E-06	4.47E-06	1.80E-05	8.63E-06
⁶⁷ Ge	2.65E-08	2.49E-09	1.98E-08	9.69E-09
⁶⁸ Ge	1.19E-08	1.06E-09	7.24E-09	3.21E-09
⁶⁹ Ge	1.06E-10	6.09E-11	1.73E-10	4.62E-11
⁷⁰ Ge	1.43E-10	1.39E-10	2.06E-10	6.46E-11
⁷¹ Ge	4.51E-11	2.98E-11	6.58E-11	1.91E-11

Species	Models			
	40A	40B	40C	40D
²⁶ Al	3.39E-05	3.10E-05	5.45E-05	1.40E-05
⁴¹ Ca	5.30E-06	4.05E-06	1.50E-05	9.05E-07
⁴⁴ Ti	1.64E-04	1.50E-05	4.26E-04	7.52E-08
⁵⁶ Ni	1.07E-01	8.11E-02	2.40E-01	6.28E-08
⁵⁷ Ni	3.25E-03	1.45E-03	7.68E-03	6.90E-08
	40SHa	40SHb	40SLa	40SLb
²⁶ Al	5.70E-05	5.52E-05	5.36E-05	5.35E-05
⁴¹ Ca	8.65E-06	7.40E-06	2.27E-05	2.24E-05
⁴⁴ Ti	1.18E-03	6.67E-06	6.52E-04	8.72E-06
⁵⁶ Ni	5.44E-01	9.01E-02	4.38E-01	1.09E-01
⁵⁷ Ni	1.81E-02	1.39E-03	1.18E-02	2.16E-03
	25A	25B	25Sa	25Sb
²⁶ Al	1.10E-02	1.23E-02	1.22E-02	1.22E-02
⁴¹ Ca	1.95E-06	1.41E-06	2.06E-06	2.06E-06
⁴⁴ Ti	1.31E-04	3.66E-05	2.14E-04	5.73E-05
⁵⁶ Ni	7.81E-02	1.51E-01	1.64E-01	9.07E-02
⁵⁷ Ni	2.12E-03	2.65E-03	4.18E-03	2.55E-03

TABLE 8

Major Radioact isotopes (M_{\odot})

Model	$M(^{56}\text{Ni})$	[Fe/H]	[O/Fe]	[Mg/Fe]	[Si/Fe]	[S/Fe]	[Sc/Fe]
		[Ti/Fe]	[Cr/Fe]	[Mn/Fe]	[Co/Fe]	[Zn/Fe]	
40A	1.1E-01	-3.8	8.32E-01	7.59E-01	5.84E-01	1.26E-01	-3.04E-01
40B	8.1E-01	8.24E-02	2.08E-02	-4.32E-01	2.59E-02	1.56E-01	
		-3.1	9.55E-01	8.86E-01	5.95E-01	5.83E-02	-1.47E+00
40C	2.4E-01	-5.09E-01	-2.91E-01	-5.08E-01	-1.58E-01	-1.73E-01	
		-4.0	6.25E-01	5.52E-01	4.26E-01	1.31E-01	1.16E-01
40D	6.3E-08	1.06E-01	-6.90E-02	-4.77E-01	1.98E-01	3.20E-01	
		-6.6	3.28E+00	3.20E+00	3.09E+00	2.04E+00	5.15E-01
40SHa	5.4E-01	8.45E-01	5.85E-01	5.12E-01	-5.10E-01	-5.08E+00	
		-3.1	2.93E-01	1.95E-01	1.80E-01	-5.11E-02	-1.45E+00
40SHb	9.0E-02	1.08E-01	-9.19E-04	-3.69E-01	-1.02E-01	2.53E-01	
		-3.8	9.81E-01	8.84E-01	8.69E-01	6.37E-01	-1.18E+00
40SLa	4.4E-01	6.44E-02	5.14E-01	2.41E-01	-2.01E+00	-6.86E+00	
		-2.2	3.93E-01	3.08E-01	2.96E-01	8.66E-02	-1.44E+00
40SLb	1.1E-01	7.72E-03	-3.15E-02	-4.05E-01	-1.71E-01	2.61E-01	
		-2.8	9.28E-01	8.43E-01	8.31E-01	6.21E-01	-9.30E-01
25A	7.8E-02	-8.10E-03	3.84E-01	1.30E-01	-1.18E+00	-2.10E+00	
		-3.7	6.33E-01	6.74E-01	2.14E-01	-6.98E-02	2.43E-02
25B	1.5E-01	2.78E-02	-1.84E-01	-5.67E-01	1.88E-01	3.62E-01	
		-2.5	3.83E-01	4.31E-01	-2.26E-02	-2.78E-01	-1.97E+00
25Sa	1.6E-01	-5.05E-01	-2.76E-01	-6.87E-01	2.22E-02	-2.72E-02	
		-2.7	3.52E-01	3.97E-01	-2.37E-02	-2.63E-01	-1.86E+00
25Sb	9.1E-02	-6.89E-02	-1.45E-01	-6.86E-01	8.40E-02	2.93E-01	
		-2.9	6.02E-01	6.47E-01	2.27E-01	-1.34E-02	-1.67E+00
		-1.82E-01	1.02E-02	-4.38E-01	-3.94E-01	-2.86E-01	

TABLE 9

[X/Fe]. [Fe/H] is estimated with equation (6) and (7) in the text.